

On Effects of Electrostatic Waves on the Auroral Ionospheric
Plasma

Susumu Saito

Solar-Terrestrial Environment Laboratory
Nagoya University, Japan

Acknowledgments

Chapters 3–4 of this thesis are mostly a reproduction of published materials (Saito *et al.*, Observation of isotropic electron temperature in the turbulent E region, *Annales Geophysicae*, vol. 19, 1, 2001; Saito *et al.*, Effects of a kappa distribution function of electrons on incoherent scatter spectra, *Annales Geophysicae*, vol. 18, 1124, 2000; Buchert and Saito, On the Pedersen current which is carried by electrons, *SUBSTORM-4*, 485, 1998).

I wish to express my sincere gratitude to my supervisor Prof. R. Fujii, who helped to conduct my study. I would also like to express my sincere gratitude to Prof. S. C. Buchert, who also helped provide guidance for my study. His knowledge and advice have greatly helped me. I am deeply grateful to Prof. Matuura who was my supervisor in the first year of my master's study program.

I am deeply grateful to Dr. F. R. E. Forme for his discussion and suggestions, which greatly helped me in the study of Chap. 4 in this thesis. Prof. T. Ogawa and Dr. S. Nozawa are greatly appreciated for their important help, discussion, and encouragement.

Prof. T. Hagfors is sincerely acknowledged for his discerning insight into my thesis. Appendix A is based on Hagfors (1984) and his personal communication to me.

I would like to acknowledge the contribution of the staff and students of STEL for their support, concern, and friendship. This thesis was finally written at the Auroral Observatory, University of Tromsø, Norway with the financial support of the Research Council of Norway. I wish to acknowledge the staff and students of the Auroral Observatory for their support and friendship to me as I studied in a foreign country. We are indebted to the director and staff of EISCAT for operating the facility and supplying the data. EISCAT

is an International Association supported by Finland (SA), France (CNRS), the Federal Republic of Germany (MPG), Japan (NIPR), Norway (NFR), Sweden (NFR) and the United Kingdom (PPARC).

Data originated from the Imaging Riometer for Ionospheric Studies (IRIS), operated by the Department of Communication Systems at Lancaster University (UK), funded by the Particle Physics and Astronomy Research Council (PPARC) in collaboration with the Sodankylä Geophysical Observatory.

The STARE radars are operated by the Max-Planck-Institut für Aeronomie in cooperation with ELAB, the Technical University of Norway, and the Finnish Meteorological Institute. I am grateful to Dr. P. Eglitis of the Swedish Institute of Space Physics Uppsala Division (IRFU), Sweden for providing the data of the STARE system and for his important advice.

I would like to express my gratitude to the track and field club, Nagoya University, and especially to Prof. H. Kunieda and Prof. Y. Kanao, for their support and friendship throughout my life at Nagoya University.

Finally, I wish to thank my parents for their continuously long and steady support of my study program.

Contents

Acknowledgment	i
Contents	iii
Figure List	vi
Notation	x
Abstract	xi
1 General Introduction	1
1.1 The Ionosphere	2
1.1.1 Temperatures in the Ionosphere	3
1.1.2 Electric Currents in the Ionosphere	7
1.2 Different Types of Electrostatic Waves	9
1.2.1 Electrostatic Waves in an Unmagnetized Plasma	10
Langmuir Waves	10
Ion Acoustic Waves	11
1.2.2 Unstable Electrostatic Waves in the E region	13
Farley-Buneman Wave	16
Gradient drift Wave	17
Unified dispersion relation of Farley-Buneman and Gradient drift instabilities	18

1.3	Scattering of Electromagnetic Waves by Electrostatic Waves	18
1.3.1	Coherent Scattering	19
1.3.2	Incoherent Scattering	19
2	Instruments	27
2.1	The EISCAT radar system	27
2.2	The STARE radar system	28
2.3	The Kilpisjärvi IRIS System	30
3	E region	35
3.1	Interaction Between the Farley-Buneman Wave and Electrons	36
3.1.1	Introduction	36
3.1.2	Tristatic Observation of Electron Temperatures by EISCAT	38
3.1.3	Discussion	42
3.2	Energy Balance of Electrons: Pedersen Current Carried by Electrons	43
3.2.1	Introduction	43
3.2.2	Methods	44
3.2.3	Observation	47
3.2.4	Discussion	49
3.3	Cosmic Noise Absorption: Comparison with observation by IRIS	57
3.3.1	Introduction	57
3.3.2	Observation	58
3.3.3	Discussion	59
3.4	Summary	64
4	F region	66
4.1	Introduction	66
4.2	Theory	69
4.3	Results of calculation and discussion	74
4.3.1	Incoherent scatter spectra with kappa distribution I: Ion lines	74

4.3.2	Difference of plasma parameters as a results of fitting with Maxwellian distribution	77
4.3.3	Incoherent scatter spectra with kappa distribution II: plasma lines .	83
4.4	Summary	88
5	Concluding Remarks	89
A	The Electromagnetic Wave Propagation in the Turbulent Plasma	93
A.1	The wave propagation problem	93
A.2	The riometer case.	97
B	Plasma Disersion Equation: Kinetic Treatment	101
B.1	Fourier Transforms	101
B.2	Laplace Transforms	102
B.3	Basic Equations	102
B.4	Plasma Dispersion Equation	104
C	Derivation of $Z_{\kappa,-}^*(\xi_{\kappa})$	106
C.1	Gamma Function	106
C.2	Cauchy Residue Theorem	107
C.3	Derivation	107
	Bibliography	111

List of Figures

1.1	Typical height profile of the electron density	4
1.2	Left panel: Typical height profiles of T_n , T_i , and T_e for a quiet condition. Right panel: The same as on the left, but for a disturbed condition.	6
1.3	Dispersion relation of a Langmuir wave	12
1.4	Dispersion relation of an ion acoustic wave	14
1.5	Geometry of the system considered in Sec. 1.2.2.	21
1.6	Electron and ion distribution functions for a $u_{e0} < C_s$, and b $u_{e0} > C_s$	22
1.7	Schematic drawing of the mechanism of the gradient drift instability. After Kelley (1989), Fig. 4.31	23
1.8	The four types of radar spectra that are observed in the auroral electrojet. After Kelley (1989) Fig. 8.27.	24
1.9	Schematic drawing of IS spectrum. a $k_{radar}\lambda_D \gg 1$, b $k_{radar}\lambda_D \ll 1$,	25
1.10	IS spectra with different parameters. When a n_e , b T_i , c T_e/T_i , d u_i , e ν_{in} , and f ion composition are changed.	26
2.1	Geographical locations of the EISCAT radars. Tx/Rx means that the radar both transmits and receives. Rx means that the radar only receives.	29
2.2	The STARE field of view. The position of the EISCAT Tromsø beam at field-aligned direction is also plotted.	31

2.3	The projection of Kilpisjärvi IRIS beams onto the ionosphere at 90 km altitude. The outline is the locus at which the sensitivity is 3 dB lower than at the beam center. (From IRIS homepage http://www.dcs.lancs.ac.uk/iono/iris http://www.dcs.lancs.ac.uk/iono/iris /) The position of the EISCAT Tromsø beam at a field-aligned direction is also plotted.	33
3.1	Overview of a data set with long periods of elevated T_e in the lower E region. The top panel shows $ \mathbf{E} $ with a time resolution of 5 minutes. The approximate threshold of the MTSI is about 20 mVm^{-1} . The middle and bottom panels show the electron and ion temperatures, respectively. . . .	40
3.2	a Scatter plot of the electron temperatures from different aspect angles observed with the Tromsø and Sodankylä EISCAT sites. The errors in fitting to the IS spectra are also plotted. b The same as a , but the ion temperatures are compared.	41
3.3	The same as Fig. 3.2, but Tromsø and Kiruna data are compared.	41
3.4	The same format as Fig. 3.1. But the electric field (top panel) is plotted with a 1 min resolution.	48
3.5	Height profile of (left) temperatures of ions, electrons and neutrals, and (right) Pedersen conductivity due to ions (blue) and electrons (red). . . .	50
3.6	Electron flow angles relative to the $\mathbf{E} \times \mathbf{B}$ directions at 108 km are plotted. The flow angle is measured in a counter-clockwise direction (from $\mathbf{E} \times \mathbf{B}$ to $-\mathbf{E}$). Flow angles are calculated both with and without taking the cooling by ions into account (solid line and dashed line, respectively).	51
3.7	Two-dimensional map of echo intensities and flow velocity vectors measured by the STARE system at 1149 UT on September 16, 1999 is shown. The echo intensities are measured in dB units with respect to the background noise level. The flow vectors are derived from two velocity components measured at Midstandan and Hankasalmi applying the cosine rule.	53

3.8	Similar to Fig. 3.6. Angles of flow derived from STARE data by applying the cosine rule are also plotted (dash-dotted line).	54
3.9	Semi-empirically obtained relation between height-integrated current and cross field voltage for a specific electron density profile. A straight line (linear Ohm's law, dashed line) would result without anomalous heating. However, above the threshold for the MTSI, the total height-integrated current $J_{P,total} = J_{P,e} + J_{P,i}$ (solid line) is higher.	56
3.10	Overview of a data set with long periods of elevated T_e in the lower E region with a time resolution of 1 min. The top panel shows the absorption measured by beam 9 of the Kilpisjärvi IRIS. The last four panels show observation by the EISCAT, $ \mathbf{E} $ (the second panel), T_e at 108 km (third), n_e at 108 km (fourth), and n_e at 90 km (fifth).	60
3.11	Absorptions estimated by the EISCAT data (red: $\nu_e = \nu_{en} + \nu_e^*$, green: $\nu_e = \nu_{en}$) and the IRIS measurements (blue line) are compared between 1400 and 1500 UT when $ \mathbf{E} $ is generally strong.	62
3.12	The same as Fig. 3.11. But the results are for the period when T_e is not enhanced, but n_e at 90 km is enhanced.	63
4.1	A comparison between Maxwellian and kappa distribution with $\kappa = 3, 5, 10$, and 40. Maxwellian distribution (<i>dashed line</i>) corresponds to $\kappa = \infty$. x -axes are indicated by velocities normalized by $v_{th,M}$ and $v_{th,\kappa=3}$.	72
4.2	IS spectral density functions of kappa distribution plasma for a different spectral index, $\kappa = 3, 5, 10$, and 40, together with one from Maxwellian plasma ($\kappa = \infty$) are shown. For this case, $n_e = 2 \cdot 10^{11} m^{-3}$, $T_i = 2000 K$, $T_e = 3000 K$, and $m_i = 16 a.m.u.$ x -axes are indicated by corresponding velocities normalized by $v_{th,M}$ and $v_{th,\kappa=3}$ as well as by a frequency in kHz	76

4.3	a, b. Solutions of dispersion equation for the ion acoustic waves for $\kappa = 3$ and Maxwellian. a Frequency b Damping rate are plotted over electron temperature. Ion temperature and electron density are fixed to 1000 K and $n_e = 2 \cdot 10^{11} \text{ m}^{-3}$, respectively	78
4.4	An example of fitting on an IS spectrum ($n_e S(\mathbf{k}, \omega)$) with kappa distribution by an IS spectrum with Maxwellian distribution. The model spectrum (<i>plotted by circles</i>) assumes $T_i = 2000 \text{ K}$, $T_e = 3000 \text{ K}$, $n_e = 2 \cdot 10^{11} \text{ m}^{-3}$, and $\kappa = 3$. Solid line shows fitted IS spectrum with Maxwellian distribution function with $T_i = 2002 \text{ K}$, $T_e = 1797 \text{ K}$, $n_e = 1.996 \cdot 10^{11} \text{ m}^{-3}$	80
4.5	The difference of parameters when kappa distribution IS spectra are interpreted by assuming Maxwellian distribution for T_i , T_e , and n_e are shown from the <i>top</i> to the <i>bottom</i> . They are plotted as relative errors to real (kappa distribution) parameters	81
4.6	The two spectra in Fig. 4.4 are shown for wider range of frequency. <i>y-axis</i> is shown in logarithmic scale.	82
4.7	Plasma lines (upshifted) for various electron temperatures (2000 - 10 000 K) for $\kappa = 3$ (<i>solid line</i>) and Maxwellian (<i>dashed line</i>) are shown. Electron density is fixed to $2 \cdot 10^{11} \text{ m}^{-3}$. <i>x-axis</i> ranges are all 3 - 7 MHz. But <i>y-axis</i> ranges are arbitrary for each plot	85
4.8	Plasma lines (upshifted) are plotted for a different spectral index, $\kappa = 3, 5, 10$, and 40, together with plasma line of Maxwellian plasma ($\kappa = \infty$)	86
4.9	Plasma lines (upshifted) are plotted for the sets of parameters appeared in Fig. 4.4, $(n_e, T_i, T_e, \kappa) = (2 \cdot 10^{11} \text{ m}^{-3}, 2000 \text{ K}, 3000 \text{ K}, 3)$ (<i>solid line</i>) and $(1.996 \cdot 10^{11} \text{ m}^{-3}, 2002 \text{ K}, 1797 \text{ K}, \infty(\text{Maxwellian}))$ (<i>dashed line</i>)	87
C.1	Contours of integration for signs and special values of ξ_κ are shown. The contour C_1 must be above a pole ξ_κ , because the Laplace transform is defined as $\text{Im}[\xi_\kappa] < 0$	110

Notation

General Notation

B	magnetic flux density	ϵ_0	permittivity of the vacuum
E	electric field	λ_D	Debye length
e	elementary charge	μ_0	permeability of the vacuum
j	current density	ν	collision frequency
k	wave vector	ρ_q	charge density
k_B	Boltzmann constant	ω	wave angular frequency
m	mass	Ω	gyrofrequency
n	number density		
p	pressure		
q	charge		
T	temperature		
u	bulk velocity		
v	velocity		

Subscripts

e	electron	en	electron-neutral
i	ion	in	ion-neutral
n	neutral	s	species of particles

Abstract

We have studied some effects of electrostatic waves and turbulences on the plasma in the auroral both E and F regions both experimentally and theoretically.

In the E region, electron heating by Farley-Buneman waves are studied using the EISCAT CP-1 data. We find that electrons are strongly heated in the magnetic field-line direction during high electric field events. The remote site data show that the electron temperature increases almost the same amount as in the field-perpendicular direction, and that electron heating by E region plasma turbulence is isotropic. We discuss the implementations of our observation for the “plasmon”-electron as well as the wave Joule heating models of the anomalous electron heating in the E region. St.-Maurice (1987)’s model which shows that Farley-Buneman waves have an electric field component both perpendicular and parallel to \mathbf{B} and effectively heat electrons can explain our results. We also suggest that if T_e enhancement is rather due to a direct scattering of electrons by wave fields not involving electron-neutral collisions, our observation implies that these waves should be isotropic.

Because the total energy is conserved, we argue that electrons must partly drift along the background electric field when the electron temperature is elevated above the background neutral temperature. We parameterize the effect of the waves by the anomalous (effective) electron collision frequency ν_e^* . We find that a rotation of the electron flow direction from a $\mathbf{E} \times \mathbf{B}$ direction can be up to $\sim 8^\circ$. Although we could not confirm the rotation with the STARE data, we point out the possibility of using an optical instrument to test our results. We also discuss the importance of electron heating on the Magnetosphere-Ionosphere coupling.

By using the Kilpisjärvi IRIS data, we examine the nature of the anomalous (effective) electron collision frequency. We find that including ν_e^* in the absorption model leads to overestimation of the cosmic noise absorption when compared with observation by the Kilpisjärvi IRIS. We find that ν_e^* has a limited range of application.

In the F region, we have studied incoherent scatter spectra which are a scattering of electromagnetic waves by electrostatic ion acoustic waves and Langmuir waves. We have theoretically calculated incoherent scatter spectra for a plasma that consists of electrons with kappa distribution function and ions with Maxwellian neglecting the effects of the magnetic field and collisions.

The ion line spectra have a double-humped shape similar to those from a Maxwellian plasma. The electron temperatures are underestimated, however, by up to 40% when interpreted assuming Maxwellian distribution. Ion temperatures and electron densities are affected little. Accordingly, actual electron temperatures might be underestimated when energy input maintaining a high energy tail exists. We have also calculated plasma lines with the kappa distribution function. They are enhanced in total strength, and the peak frequencies appear to be slightly shifted to the transmitter frequency compared to the peak frequencies for a Maxwellian distribution. The damping rate depends on the electron temperature. For lower electron temperatures, plasma lines for electrons with a κ distribution function are more strongly damped than for a Maxwellian distribution. For higher electron temperatures, however, they have relatively sharp peaks.

Chapter 1

General Introduction

Various waves can propagate in space and in plasmas which are important because they carry information (energy and momentum) and can even modify a plasma by interacting with particles, and even with other waves. Electrostatic waves are a part of plasma waves which propagate in a direction parallel to the wave's electric field. (Consequently They have no oscillating magnetic field component.) They can propagate only in plasmas because they need a density fluctuation of electric charges. Such waves contain information on plasmas in the ionosphere. Ground-based instruments such as radars utilize the scattering of transmitted radio waves to probe the ionosphere. Therefore, it is very important to study the effects of electrostatic waves not only as a natural plasma laboratory but also for the correct analysis of radar experiments. In this study, we examine certain phenomena in which electrostatic waves play important roles in the ionospheric E and F region. Among many interesting phenomena related to electrostatic waves, we explore some topics which have close relationships with the electron temperature which is one of the most basic and important parameters in the ionospheric plasma. In other words, the keywords of our study are 'electrostatic waves' and 'electron temperature.' With these keywords, we investigate how electrostatic waves interact with and modify the ionospheric plasma through the E and F region. They will be presented separately in Chap. 3 and Chap. 4, respectively.

For a general introduction, the earth's ionosphere and electrostatic waves are briefly

reviewed in this chapter. In Sec. 1.1, a brief summary of the earth's ionosphere is provided. In Secs. 1.1.1–1.1.2 the temperature is defined, and the heat production and the ionospheric current are briefly described. Some properties of electrostatic waves and a brief explanation of some important electrostatic waves are given in Sec. 1.2. Basic concepts of scattering of radio waves, both coherent and incoherent scattering, are dealt with in Sec. 1.3.

1.1 The Ionosphere

The ionosphere is the region where the earth's atmosphere is ionized. At the end of the 19th century the existence of an electrically conducting layer in the earth's upper atmosphere had been predicted by observations of the geomagnetic field. To explain the diurnal variation of the geomagnetic field, it was more reasonable to assume that an electric current system exists in the sky than to ascribe it to inside the solid earth. In the early 20th century, Kennelly and Heaviside pointed out that there was an electrical conducting layer in the upper atmosphere to explain a radio communication experiment across the Atlantic ocean by Marconi. The existence of this layer was confirmed in 1925 by Appleton and Barnett, and Breit and Tuve, by measuring the delay time between transmitting the radio wave vertically upward until the reflected wave was received to determine the height of the layer.

The earth's ionosphere consists of partially ionized gases which is created by ionizing neutral molecules and atoms of the atmosphere caused by certain ionizing sources. The main ionizing source is solar EUV radiation. Solar X-ray radiation, and high energy particles like cosmic rays, auroral particles, radiation belt particles, and solar protons can also ionize. But generally their contribution is smaller than that of solar EUV radiation.

The ionosphere has several peaks in density at different altitudes. Fig 1.1 shows the typical height profile of the electron density, n_e . The ionosphere is divided into layers by different electron densities and production mechanisms. Between about 90 ~ 150 km, it is called E region.

Above about 150 km is the F region, and below about 90 km is the D region. Because the density of the neutral atmosphere exponentially changes with altitude and the composition also changes in altitude, the dominant physical processes and dominant ionized species change in altitude as well. In the F region, the dominant ion is O^+ , while in the E region they are NO^+ and O_2^+ . The increasing neutral density increases the collision frequency between ionized species and neutrals. The collision frequency is important for the ionospheric electric current. Most of the currents flow in the E region. In the D region, negative ions and cluster ions become important. Large collision frequency between electrons and neutrals enhances cosmic noise absorption in the D region. All through the ionosphere, the ionization degree is very low. Even around the peak in the F region, it is $\sim 10^{-3}$, and it is $\sim 10^{-6}$ or less in the E region. Therefore, the ionosphere is weakly ionized plasma, where the effects of the neutral particles can be important.

In the polar ionosphere, the auroral particle precipitation can contribute significantly to the formation of the ionosphere. Both protons and electrons precipitate into the earth's ionosphere and ionize. The species and the energy of the precipitating particles determine the altitude of maximum ionization. For example, electrons with energy less than 1 keV ionize the F region. Electrons with energy of 10 keV ionize mainly the E region, about 110 km in altitude. Higher energy electrons can penetrate into the D region, and enhance the cosmic noise absorption which is measured in riometers.

1.1.1 Temperatures in the Ionosphere

First of all, the temperature must be defined. There are several ways of defining the temperature. Here we define the temperature T of one species with mass m by the second order moment of a distribution function $f(\mathbf{v})$, or by mean kinetic energy of particles,

$$\langle \frac{1}{2}m|\mathbf{v}|^2 \rangle = \int_{-\infty}^{+\infty} \frac{1}{2}mv^2 f(\mathbf{v})d\mathbf{v} \equiv \frac{3}{2}k_B T \quad (1.1)$$

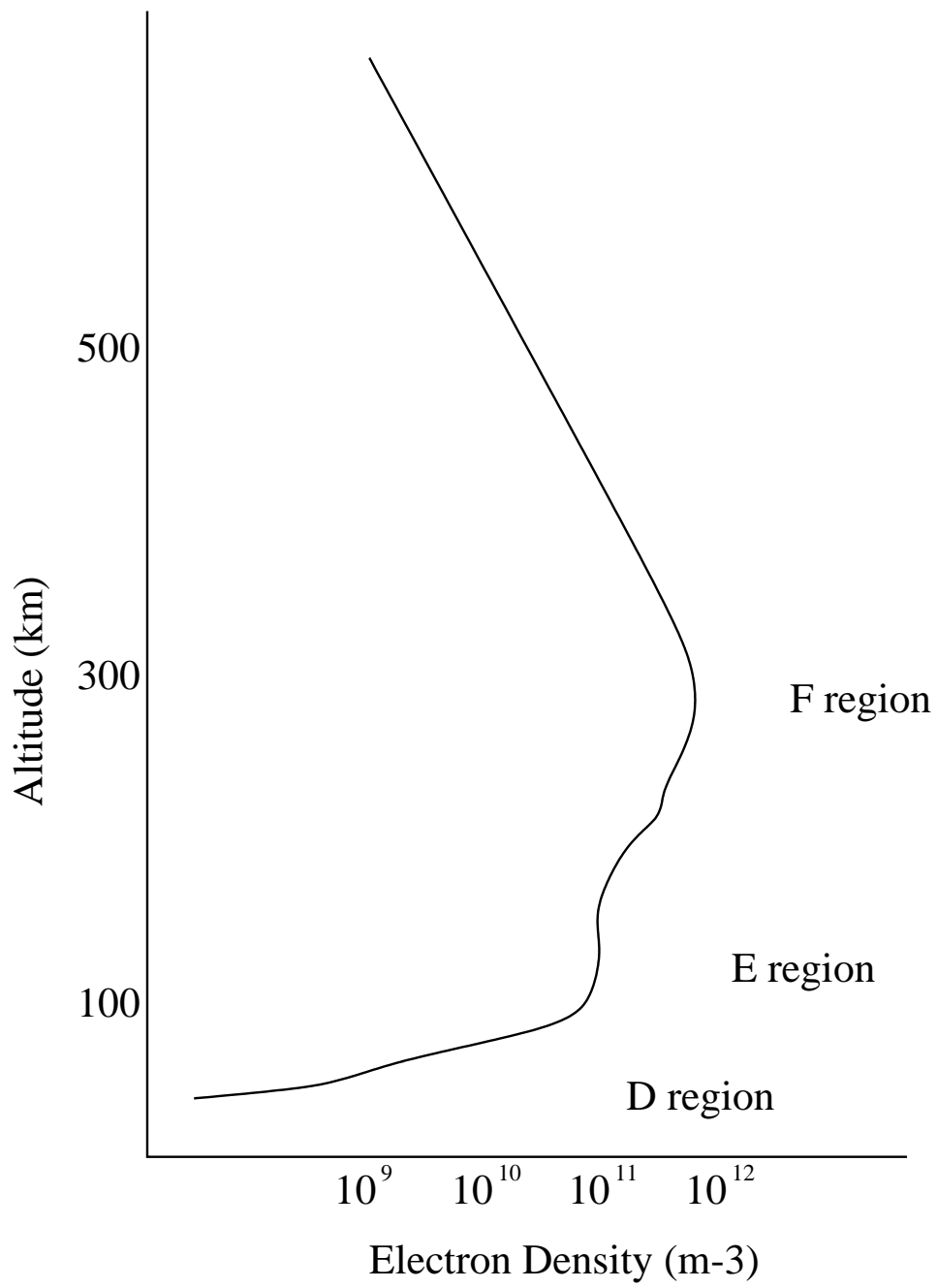


Figure 1.1: Typical height profile of the electron density

where k_B is the Boltzmann constant. For an anisotropic distribution function, we can define the temperature along a certain direction T_{\parallel} ,

$$\langle \frac{1}{2}mv_{\parallel}^2 \rangle = \int_{-\infty}^{+\infty} \frac{1}{2}mv_{\parallel}^2 f(v_{\parallel}) dv_{\parallel} \equiv \frac{1}{2}k_B T_{\parallel}. \quad (1.2)$$

In the ionosphere, ions, electrons, and neutrals can have different temperatures. Generally the neutral temperature increases above the mesopause. In lower altitudes ($\lesssim 110$ km), very frequent collisions between charged and neutral particles force them into a state of thermal equilibrium, i.e., $T_n \simeq T_i \simeq T_e$, where T_n , T_i , and T_e , are the temperatures of neutrals, ions, and electrons, respectively. Because of a huge difference of mass between an electron and a neutral particle, electrons more easily depart from thermal equilibrium with decreasing electron-neutral collision frequency than ions. In a geomagnetically quiet condition, the following relation is found in the ionosphere, $T_n \lesssim T_i \lesssim T_e$. In a geomagnetically disturbed condition, however, T_i can be higher than T_e at around 120 km due to the heat produced by an electric current flowing in the ionosphere. In Fig. 1.2, a schematic drawing of height profiles of temperatures for a disturbed condition is compared with those of a quiet condition.

The temperatures are determined by a balance between a heating rate and a cooling rate. There are various heating sources in the ionosphere. Solar illumination heats every species. Particle precipitation heats electrons efficiently in the F region. A strong electric field enhances the electric currents and produces heat by Joule heating. In the lower E region at around 110 km, it is known that electrons can be heated up to ~ 3000 K by electrostatic plasma waves excited when the relative drift velocity between electrons and ions is higher than the local ion acoustic velocity (Schlegel and St.-Maurice, 1981; St.-Maurice *et al.*, 1981; St.-Maurice and Laher, 1985; Robinson, 1986; Igarashi and Schlegel, 1987; Williams *et al.*, 1990; Jones *et al.*, 1991; Davies and Robinson, 1997). Elastic and inelastic collisions between charged and neutral particles transfer the thermal energy from heated charged particles to neutral particles. Hence, the neutral atmosphere acts as a heat sink in the ionosphere.

For ions, the energy balance of heating due to friction with neutrals and cooling by

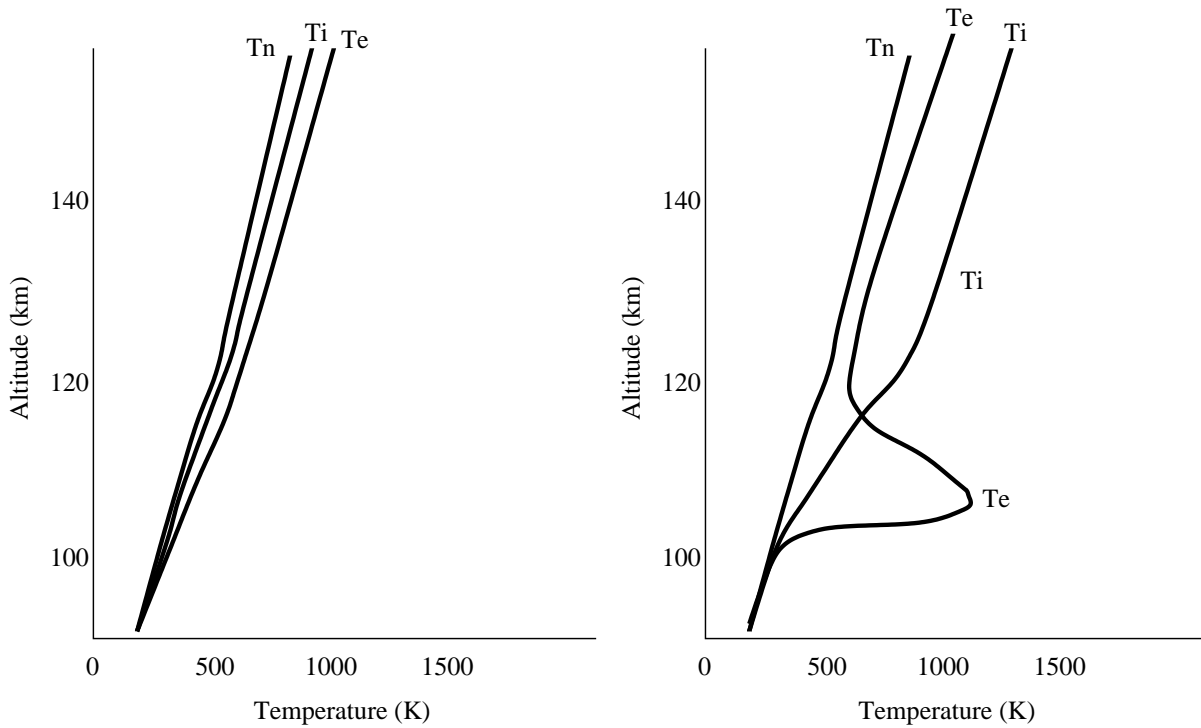


Figure 1.2: Left panel: Typical height profiles of T_n , T_i , and T_e for a quiet condition. Right panel: The same as on the left, but for a disturbed condition.

collisions with neutrals is given by (e.g. St.-Maurice and Hanson, 1982; Kelley, 1989; Rees, 1989)

$$\begin{aligned} \frac{m_i n_i \nu_{in}}{m_i + m_n} m_n |\mathbf{u}_i - \mathbf{u}_n|^2 \phi_{in} &= 2n_i \frac{m_i}{m_i + m_n} \psi_{in} \nu_{in} \frac{3}{2} k_B (T_i - T_n) \\ &+ 2n_i \frac{m_i}{m_i + m_e} \nu_{ie} \frac{3}{2} k_B (T_i - T_e) \end{aligned} \quad (1.3)$$

and this leads to

$$T_i = T_{eq} + \frac{m_n \phi_{in}}{3k_B \psi_{in}} |\mathbf{u}_i - \mathbf{u}_n|^2 \quad (1.4)$$

where

$$T_{eq} = T_n + \frac{(m_i + m_n) \nu_{ie}}{m_i \nu_{in} \psi_{in}} (T_e - T_i). \quad (1.5)$$

The dimensionless parameter ϕ_{in} and ψ_{in} depend on the nature of the collision between ions and neutrals. For collisions between O^+ and O (above about 200 km), ϕ_{in} and ψ_{in} are approximately unity.

For electrons, the temperature is determined by the energy balance (e.g. Rees, 1989; Jones *et al.*, 1991)

$$Q_e = L_{e,el} + L_{e,rot} + L_{e,vib} + L_{e,fO} + L_{e,ion} \quad \text{Watt m}^{-3} \quad (1.6)$$

where Q_e is the electron heating rate. $L_{e,el}$ is the cooling rate due to elastic collision with neutral species, $L_{e,rot}$ and $L_{e,vib}$ are the cooling rates due to excitation of rotational and vibrational levels of neutral molecules, respectively, and $L_{e,fO}$ is the cooling rate due to excitation of the fine structure level of the O atom. These cooling rates are modeled and reviewed by Schunk and Nagy (1978). $L_{e,ion}$ is the cooling rate by interaction with ions. These quantities are complicated functions of $T_e - T_n$ and $T_e - T_i$. Therefore, numerical calculation is necessary to solve the energy balance equation of electrons (Eq.(1.6)).

1.1.2 Electric Currents in the Ionosphere

Joule heating is caused by a dissipative current (parallel to the electric field). The energy source of the electron heating in the lower E region is a large electron-ion relative drift velocity, in other words, a current. Neglecting the effects of waves on charged particle

motions for the moment, solving the ion and electron mobility equations derives the ion and electron velocities (e.g. Kelley, 1989; Brekke, 1997),

$$\mathbf{u}_i = \frac{\kappa_i}{1 + \kappa_i^2} \frac{\mathbf{E}'_{\perp}}{B} + \frac{1}{1 + \kappa_i^2} \frac{\mathbf{E}'_{\perp} \times \mathbf{B}}{B} + \frac{e}{m_i \nu_{in}} \mathbf{E}'_{\parallel} \quad (1.7)$$

$$\mathbf{u}_e = -\frac{\kappa_e}{1 + \kappa_e^2} \frac{\mathbf{E}'_{\perp}}{B} + \frac{1}{1 + \kappa_e^2} \frac{\mathbf{E}'_{\perp} \times \mathbf{B}}{B} - \frac{e}{m_e \nu_{en}} \mathbf{E}'_{\parallel} \quad (1.8)$$

where $\kappa_{i,e}$ are the ratio of the ion- and the electron-neutral collision frequencies, $\nu_{in,en}$, to the ion- and the electron-gyrofrequencies, $\Omega_{i,e}$, respectively, and \mathbf{E}' is the electric field in the moving frame with neutral atmosphere, and \mathbf{B} is the geomagnetic field, respectively. Here we define the gyrofrequency as a positive value

$$\Omega_{i,e} = \frac{eB}{m_{i,e}}. \quad (1.9)$$

where e is the elementary charge. Then, by the definition of the current

$$\mathbf{j} = n_e e (\mathbf{v}_i - \mathbf{v}_e), \quad (1.10)$$

the ionospheric current is written as

$$\mathbf{j} = \sigma_P \mathbf{E}'_{\perp} - \sigma_H \frac{\mathbf{E}'_{\perp} \times \mathbf{B}}{B} + \sigma_{\parallel} \mathbf{E}'_{\parallel} \quad (1.11)$$

where σ_P , σ_H and σ_{\parallel} are Pedersen, Hall and parallel conductivities, respectively, given by

$$\sigma_P = \frac{n_e e}{B} \left[\frac{\kappa_e}{1 + \kappa_e^2} + \frac{\kappa_i}{1 + \kappa_i^2} \right] \quad (1.12)$$

$$\sigma_H = \frac{n_e e}{B} \left[\frac{1}{1 + \kappa_e^2} - \frac{1}{1 + \kappa_i^2} \right] \quad (1.13)$$

$$\sigma_{\parallel} = n_e e^2 \left[\frac{1}{m_e \nu_{en}} + \frac{1}{m_i \nu_{in}} \right] = \frac{n_e e}{B} \left[\frac{1}{\kappa_e} + \frac{1}{\kappa_i} \right] \quad (1.14)$$

The first term on the right-hand-side of Eq. (1.11) is called the *Pedersen current*, and the second term is called the *Hall current*. Since $\kappa_e \ll 1$, σ_{\parallel} is much larger than σ_P and σ_H . aligned current could be very large and would immediately cancel out the potential difference. Therefore, usually it is a good approximation for the magnetic field line to be an equipotential line. Because the Hall current is perpendicular to \mathbf{E} , only the Pedersen

current is dissipative and produces heat. Because $\kappa_e \ll 1$, the first term on the right-hand-side of Eq. (1.12) vanishes. Therefore, the Pedersen current is mostly carried by ions, and heats ions selectively at around 120 km altitude. For electron heating, the effects of the plasma waves must be taken into account (St.-Maurice *et al.*, 1981; St.-Maurice and Laher, 1985; Robinson, 1986). The microscopic mechanism of electron wave heating is still under debate.

1.2 Different Types of Electrostatic Waves

Electrostatic waves are plasma waves without a fluctuating magnetic field. Maxwell's equations governing electric and magnetic fields are given by

$$\nabla \cdot \mathbf{E} = \frac{\rho_q}{\epsilon_0} \quad (1.15)$$

$$\nabla \cdot \mathbf{B} = 0 \quad (1.16)$$

$$\nabla \times \mathbf{E} = \frac{\partial \mathbf{B}}{\partial t} \quad (1.17)$$

$$\nabla \times \mathbf{B} = \mu_0 \mathbf{j} + \mu_0 \epsilon_0 \frac{\partial \mathbf{E}}{\partial t} \quad (1.18)$$

For electrostatic waves, the wave vector \mathbf{k} is parallel to the wave electric field (longitudinal wave), and the right-hand-side of Eq. (1.17) is zero.

$$\nabla \times \mathbf{E} = 0 \quad (1.19)$$

Then Eq. (1.15) is the only way to create \mathbf{E} . Therefore, electrostatic waves must be associated with charge density fluctuations.

If we adopt a two-fluid plasma model, equations of continuity and momentum become as follows:

$$\frac{\partial n_s}{\partial t} + \nabla \cdot n_s \mathbf{u}_s = 0 \quad (1.20)$$

$$\frac{\partial \mathbf{u}_s}{\partial t} + \mathbf{u}_s \cdot \nabla \mathbf{u}_s - \frac{q_s}{m_s} (\mathbf{E} + \mathbf{u}_s \times \mathbf{B}) + \frac{\nabla p_s}{n_s m_s} = \frac{\mathbf{F}'}{n_s m_s} \quad (1.21)$$

Here we ignored the production and loss in the equation of continuity. \mathbf{F}' includes all other external forces like friction with other fluids. For a friction with neutrals,

$$\mathbf{F}' = -n_s m_s \nu_{sn} \mathbf{v}_s. \quad (1.22)$$

The current density \mathbf{j} and the charge density ρ_q are defined by

$$\mathbf{j} = \sum_s n_s q_s \mathbf{u}_s \quad (1.23)$$

and

$$\rho_q = \sum_s q_s n_s. \quad (1.24)$$

To obtain a closed set of equations, we add the polytropic law of the pressure and the density

$$p_s \propto n_s^{\gamma_s} \quad (1.25)$$

where γ_s is the ratio of specific heats. In the following sections, several examples of electrostatic waves are derived by using linear approximation of these equations.

1.2.1 Electrostatic Waves in an Unmagnetized Plasma

Although plasmas in the ionosphere are magnetized, waves in an unmagnetized plasma are still important in some cases where the effects of a magnetic field can be neglected. In this section, we derive linear dispersion relations of electrostatic waves in an unmagnetized plasma, where $\mathbf{B} = 0$.

Langmuir Waves

First we consider high frequency waves where ions can be regarded as an immobile background. We assume that there is no background electric field, $\mathbf{E}_0 = 0$, and no background electron drift, $\mathbf{u}_{e0} = 0$. In what follows, we denote perturbation terms by a subscript “1,” and background terms by a subscript “0.” Assuming further that perturbations are small, that all perturbations are proportional to $\exp(-ikx + i\omega t)$ and in one-direction only, and

that the process is adiabatic ($\gamma_e = 3$ for this one-dimensional case), we obtain

$$-i\omega n_{e1} + ikn_0 u_{e1} = 0 \quad (1.26)$$

$$-i\omega m_e n_0 u_{e1} + n_0 e E_1 + i3k k_B T_e n_{e1} = 0 \quad (1.27)$$

$$ikE_1 + \frac{en_{e1}}{\epsilon_0} = 0. \quad (1.28)$$

For non-trivial solutions of these equations, the next relation is obtained.

$$\omega^2 = \omega_{pe}^2 (1 + 3k^2 \lambda_D^2) \quad (1.29)$$

where

$$\omega_{pe} = \left(\frac{n_0 e^2}{m_e \epsilon_0} \right)^{\frac{1}{2}} \quad (1.30)$$

is the plasma frequency and

$$\lambda_D = \left(\frac{\epsilon_0 k_B T_e}{n_0 e^2} \right)^{\frac{1}{2}} \quad (1.31)$$

is the Debye length. A plasma wave that obeys this dispersion relation is called a *Langmuir wave*. This dispersion relation is schematically shown in Fig. 1.3. The frequencies of Langmuir waves are higher than the plasma frequency which is, in the ionosphere, 1~10 MHz. For cold plasma or for long wavelengths, i.e., $k\lambda_D \ll 1$, Langmuir waves are found to be close to the plasma frequency.

Ion Acoustic Waves

Next we consider low frequency waves where effects of ions must be included. By the same procedure as for Langmuir waves but assuming isothermal plasma for a slowly oscillating system ($\gamma_{i,e} = 1$), we obtain

$$-i\omega n_{e1} + ikn_0 u_{e1} = 0 \quad (1.32)$$

$$-i\omega n_{i1} + ikn_0 u_{e1} = 0 \quad (1.33)$$

$$-i\omega m_e n_0 u_{e1} + n_0 e E_1 + ik k_B T_e n_{e1} = 0 \quad (1.34)$$

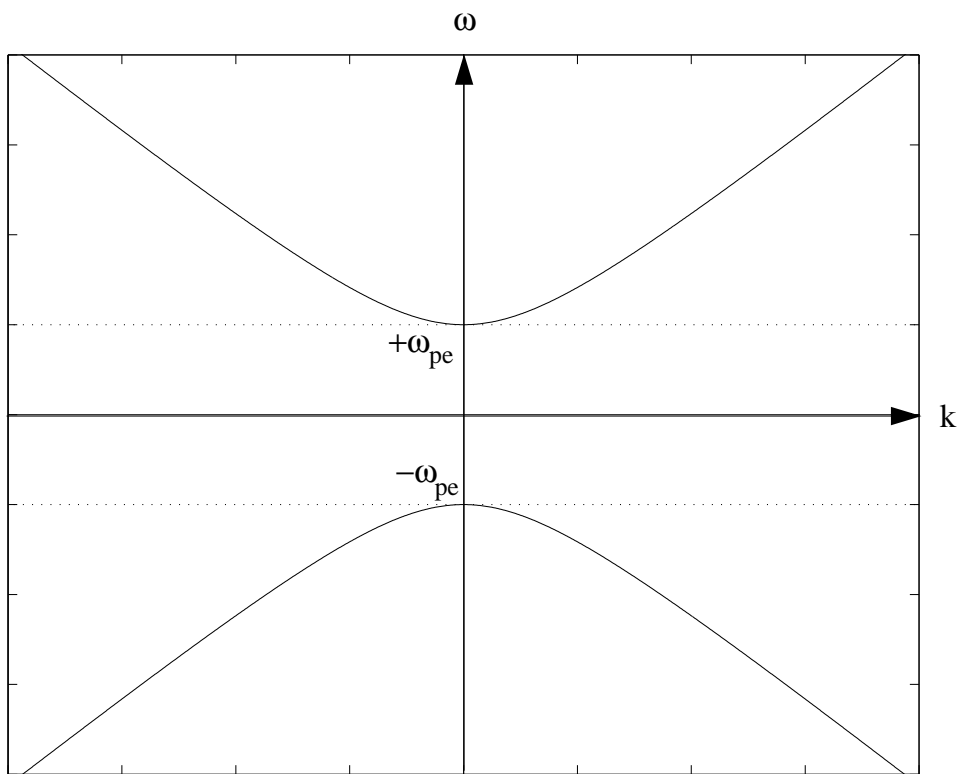


Figure 1.3: Dispersion relation of a Langmuir wave

$$-i\omega m_i n_0 u_{i1} + n_0 e E_1 + i k k_B T_i n_{e1} = 0 \quad (1.35)$$

$$i k E_1 - \frac{e n_{i1} - n_{e1}}{\epsilon_0} = 0. \quad (1.36)$$

Using the fact $m_e \ll m_i$, we obtain the dispersion relation of an *ion acoustic wave*

$$\omega^2 = \frac{k^2 k_B T_i}{m_i} + \frac{k^2 k_B T_e / m_i}{1 + k^2 \lambda_D^2}. \quad (1.37)$$

For long wavelengths where $k \lambda_D \ll 1$, the dispersion relation is reduced to

$$\omega^2 = k^2 C_s^2 \quad (1.38)$$

where

$$C_s = \left(k_B \frac{T_i + T_e}{m_i} \right)^{\frac{1}{2}}. \quad (1.39)$$

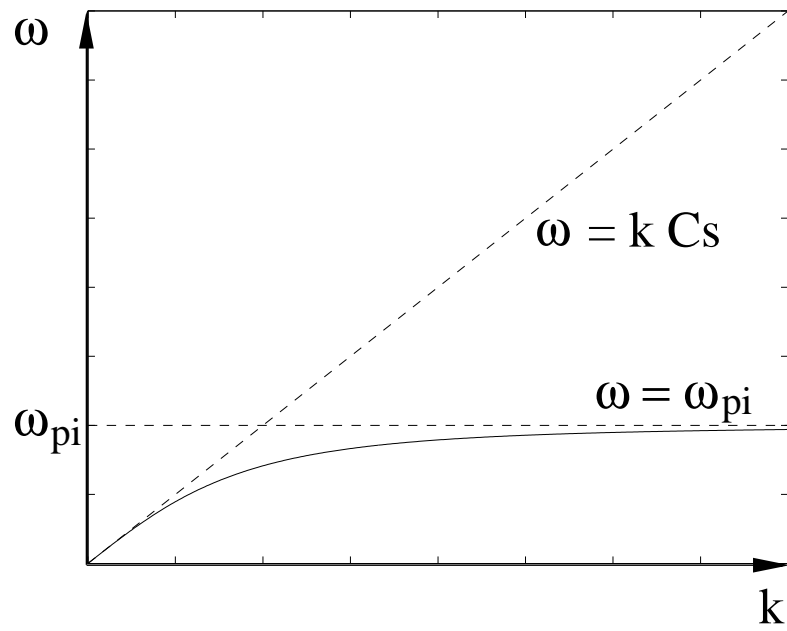
Fig. 1.4 schematically shows the dispersion relation of an ion acoustic wave.

Langmuir waves and ion acoustic waves are fundamental waves which always exist in a plasma as thermal fluctuations. A kinetic treatment of these waves is given in Appendix B.

1.2.2 Unstable Electrostatic Waves in the E region

When certain conditions are satisfied, thermal fluctuations of a plasma grow exponentially. This is called *instability*. Many kinds of instabilities are known to exist in the ionosphere. In this section, so called electrojet instabilities in the E region are described. They are observed by radars in the E region electrojet as coherent echoes. It is known that there are two mechanisms which are important for the electrojet instability. One is the modified two-stream instability (MTSI). Farley (1963), using kinetic theory, and Buneman (1963), using fluid theory, independently developed the theory of instability for the equatorial electrojet. This instability is also called the Farley-Buneman instability after these two scientists. The other important instability is the gradient drift instability which was first studied by Simon (1963) and Hoh (1963) for laboratory plasmas, and by Maeda *et al.* (1963) for the equatorial ionospheric E region. These instabilities are also important for

(a) $T_i = 0$



(b) $T_i \neq 0$

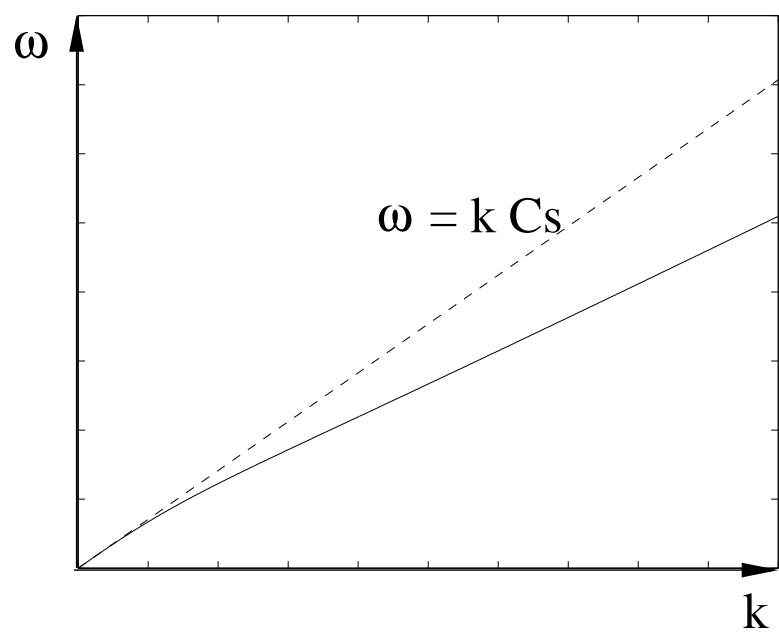


Figure 1.4: Dispersion relation of an ion acoustic wave

the polar ionosphere where the auroal electrojet which is typically more intense than the equatorial electrojet exists. In what follows, we briefly describe the linear theory of these instabilities following Kelley (1989).

In the following derivations, we assume that neutrals are at rest (or equivalently our system is moving with neutrals), that the magnetic field is in a -z-direction (downward), ($\mathbf{B} = -B\mathbf{e}_z$), the background electric field is in a y-direction, ($\mathbf{E}_0 = E_0\mathbf{e}_y$, northward), and that all the perturbations are proportional to $\exp(-ikx + i\omega t)$, $\mathbf{k} = k\mathbf{e}_x$. Here $\mathbf{e}_{x,y,z}$ means a unit vector in an x, y, and z-direction, respectively. Electrons which rarely collide with neutrals,

$$\Omega_e \gg \nu_{en} \quad (1.40)$$

drift in a -x-direction (westward). However, ions can be assumed to be at rest in the zero-order because of frequent collisions with neutrals.

$$\Omega_i \ll \nu_{in} \quad (1.41)$$

Eqs. (1.40) and (1.41) are justified when we look at the lower E region ($\lesssim 110$ km). The geometry is sketched in Fig 1.5.

Farley-Buneman Wave

The electron continuity equation which is in equilibrium in the zero-order becomes

$$i\omega n_1 - ikn_1 u_{e0} - ikn_0 u_{e1x} = 0. \quad (1.42)$$

Neglecting the electron inertia which is much smaller than the ion, the electron momentum equation yields

$$0 = \frac{eB}{m_e} u_{e1x} - \nu_{en} u_{e1y} \quad (1.43)$$

in a y-direction, and

$$0 = -\frac{e}{m_e} E_1 - \frac{eB}{m_e} u_{e1y} + ik \frac{k_B T_e}{m_e} \frac{n_1}{n_0} - \nu_{en} u_{e1x} \quad (1.44)$$

in an x-direction. For ions, the continuity equation is

$$i\omega n_1 - ik u_{i1x} n_0 = 0 \quad (1.45)$$

Because $\mathbf{v}_{i0} = 0$, only the x-component of the ion momentum equation is relevant. For ions, keeping the inertia term $\partial u_{i1x}/\partial t$,

$$i\omega u_{i1x} = \frac{e}{m_i} E_1 + ik \frac{k_B T_i n_1}{m_i n_0} - \nu_{in} u_{i1x} \quad (1.46)$$

Here we have used $\Omega_i \ll \nu_{in}$. From Eqs. (1.42)–(1.46), we obtain a dispersion relation

$$\omega - k u_{e0} = -\frac{\Psi_0}{\nu_{in}} [\omega(i\omega + \nu_i) - ik^2 C_s^2] \quad (1.47)$$

where

$$\Psi = \frac{\nu_i \nu_e}{\Omega_i \Omega_e} \quad (1.48)$$

and C_s is the ion acoustic velocity given by Eq. (1.39). If we set $\omega = \omega_r - i\gamma$ and assume $\gamma \ll \omega_r$, we obtain for the real part

$$\omega_r = \frac{k u_{e0}}{1 + \Psi_0} \quad (1.49)$$

and for the imaginary part

$$\gamma = \frac{\Psi_0 \omega_r^2 - k^2 C_s^2}{\nu_{in} (1 + \Psi_0)} \quad (1.50)$$

For $\gamma > 0$, the waves grow exponentially. So the condition for the instability is

$$u_{e0} > (1 + \Psi_0) C_s \quad (1.51)$$

Hence, when electrons drift at a higher velocity than the approximate ion acoustic velocity, the system is unstable. This condition can be understood approximately as follows: Fig. 1.6 shows the electron and ion distribution functions in the frame of ions. Fig. 1.6a is the case when the electron drift velocity u_{e0} is less than the ion acoustic velocity C_s . Then the derivative of the electron distribution function at C_s is negative, and the system is stable. When u_{e0} exceeds C_s (Fig. 1.6b), however, the derivative of the electron distribution function at C_s is positive. Then the wave gains more energy from electrons than it loses to electrons, and the wave grows. From the equations above, electron density fluctuations have the following relationship with the amplitude of wave electric fields. When we set $\Omega_e \gg \nu_{en}$,

$$\frac{E_1}{E_0} = \frac{\nu_i}{\Omega_i (1 + \Psi)} \frac{n_1}{n_0} \quad (1.52)$$

This means that the relative amplitude of the wave electric field is smaller than the density fluctuation by a factor $\nu_{in}/\Omega_i(1 + \Psi_0)$ which is much less than unity. Therefore, the wave electric field cannot be so large compared to the background electric field.

Gradient drift Wave

For the gradient drift instability, the zero-order gradient of the electron density plays an important role. In Fig. 1.7, an unstable geometry is shown. In the region where the perturbation electron density n_{e1} is negative, the perturbation electron velocity $u_{e1y} = E_{1x}/B$ is in the y-direction, and the lower density region is transported into a higher density region. Then the density fluctuation is intensified and the perturbation electric field is also intensified. This is clearly unstable. So the necessary condition of instability is

$$\mathbf{E}_0 \cdot \nabla n > 0 \quad (1.53)$$

Unified dispersion relation of Farley-Buneman and Gradient drift instabilities

Fejer *et al.* (1975) have proposed the complete linear theory including a finite zero-order ion drift \mathbf{u}_{i0} and recombination which introduces a term $-\alpha n^2$ in the continuity equations, and allows \mathbf{k} to have a component parallel to \mathbf{B} .

$$\omega_r = \frac{\mathbf{k} \cdot (\mathbf{u}_{e0} + \Psi \mathbf{u}_{i0})}{1 + \Psi} \quad (1.54)$$

$$\begin{aligned} \gamma = \frac{1}{1 + \Psi} \left\{ \frac{\Psi}{\nu_{in}} [(\omega_r - \mathbf{k} \cdot \mathbf{u}_{e0})^2 - k^2 C_s^2] \right. \\ \left. + \frac{1}{Lk} (\omega_r - \mathbf{k} \cdot \mathbf{u}_{i0}) \frac{\nu_{in}}{\Omega_i} k_{\parallel} \right\} - 2\alpha n_0 \end{aligned} \quad (1.55)$$

where L is the gradient scale length

$$\frac{1}{L} = \frac{1}{n_0} \frac{\partial n_0}{\partial y} \quad (1.56)$$

and

$$\Psi = \Psi_0 \left[\left(\frac{k_{\perp}}{k} \right)^2 + \left(\frac{\Omega_e}{\nu_{en}} \right)^2 \left(\frac{k_{\parallel}}{k} \right)^2 \right] \quad (1.57)$$

It is important that the wave vector can have a component along the magnetic field line. Even if the wave electric field is small, the current associated with the electric field could be significant because of very high conductivity along the magnetic field line as mentioned in Sec. 1.1.2, and the energy dissipation as heat could be large (St.-Maurice, 1987).

1.3 Scattering of Electromagnetic Waves by Electrostatic Waves

In the previous sections, we described electromagnetic waves in a plasma. When electromagnetic waves pass through a plasma, electron density fluctuations associated with those electrostatic waves scatter the electromagnetic waves. The scatterings are classified into two categories by their nature, *coherent scattering* and *incoherent scattering*. Both scatterings are used to probe the ionosphere by sending radio waves and measuring scattered waves by radar. In this section, coherent and incoherent scatter are briefly explained referring to Hunsucker (1991).

1.3.1 Coherent Scattering

Coherent scattering echoes are usually detected in the disturbed ionosphere where electron density fluctuations are amplified by instabilities. Radio waves are scattered by sharp electron density gradients associated with unstable waves and the spectrum widths are narrow, typically less than 1 kHz (sometimes less than 100 Hz). For example, STARE radars in Scandinavia use VHF waves and measure echoes from the auroral E region. SuperDARN radars use HF waves and measure echoes from both the E and F region. The waves responsible for the scattering in the E region are the Farley-Buneman and the Gradient drift waves. The scattered spectrum reflects the nature of the scattering waves. The Farley-Buneman waves are thought to be so called *type 1*, and when the Farley-Buneman waves are strong enough to heat electrons, *type 4* echoes of which the spectral widths are very narrow occur. *type 2* echoes of which the spectral widths are

rather wide are thought to be due to the Gradient drift waves. The types of coherent radar spectra are summarized in Fig. 1.8.

1.3.2 Incoherent Scattering

In contrast to coherent echoes, incoherent scattering (IS) echoes can be detected at any time and at any altitudes in the ionosphere. Each electron is moved by the electric field of incident radio waves and re-radiate radio waves. This mechanism is called *Thomson scattering*. The cross section is very small,

$$\sigma_T \simeq 6.653 \cdot 10^{-29} \text{ m}^2 \quad (1.58)$$

The echo power is much weaker than the power of a coherent echo. When the wavelength of the probing radio wave is smaller than the Debye length, $k_{radar}\lambda_D \gg 1$, where k_{radar} is the radar wave number, a radar observes motions of each “free” electron. In this case, the spectrum has a shape just similar to the electron distribution function. When the radar wavelength is larger than the Debye length, $k_{radar}\lambda_D \ll 1$, however, a collective motion of electrons becomes important. A radar observes a collection of waves scattered by thermal fluctuations of electron density which is described as ion acoustic and the Langmuir waves in unmagnetized plasma as described in Sec. 1.2.1. Therefore, the scattered spectrum consists of two features, the low frequency part (the ion line) and the high frequency part (the plasma line) corresponding to ion acoustic and Langmuir waves, respectively. Fig. 1.9 shows schematically the typical IS spectrum (the ion and the plasma lines) together with a gaussian shape spectrum which corresponds to a spectrum when the radar wavelength λ_{radar} is much shorter than the local Debye length λ_D . Because the ion line contains information about ions as well as electrons, IS radars can measure such parameters as the electron density, the line-of-sight ion drift velocity, the ion temperature, the electron temperature (or the ratio of the electron temperature to the ion temperature), the ion-neutral collision frequency, and ion composition (if the signal-to-noise ratio is very high). Fig. 1.10 shows how IS spectra change with some of these parameters.

In actual measurements, very powerful echoes of which one of or both peaks of the

ion line are strongly enhanced are sometimes observed (Foster, 1988; Collis *et al.*, 1991; Rietveld *et al.*, 1991). Such spectra cannot be explained by thermal fluctuations. Those spectra are rather coherent echoes and indicate that some instabilities intensify the ion acoustic waves. These anomalous spectra are often observed associated with phenomena where ions flow up and away from the earth. The mechanism of how such anomalous echoes are created, and its relationship with ion upflow phenomena are still controversial topics.

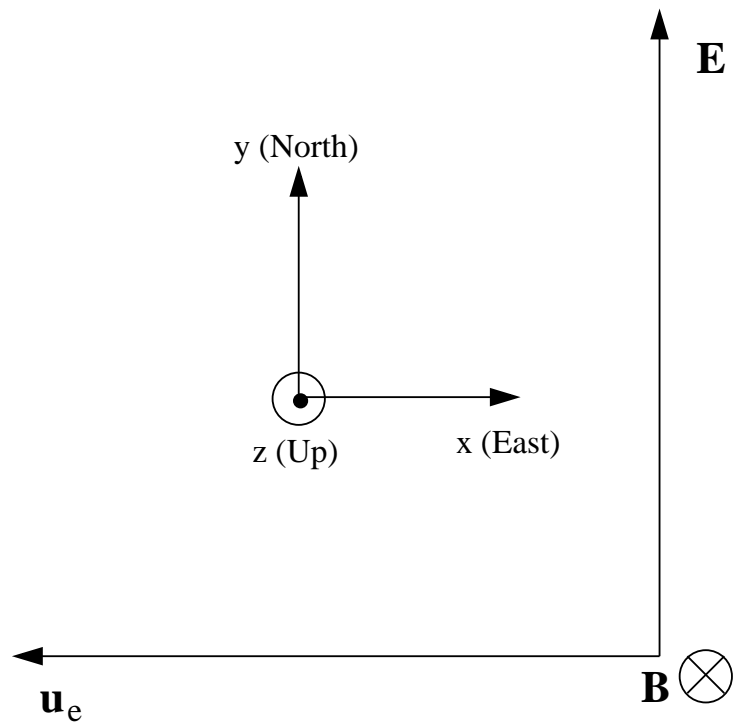


Figure 1.5: Geometry of the system considered in Sec. 1.2.2.

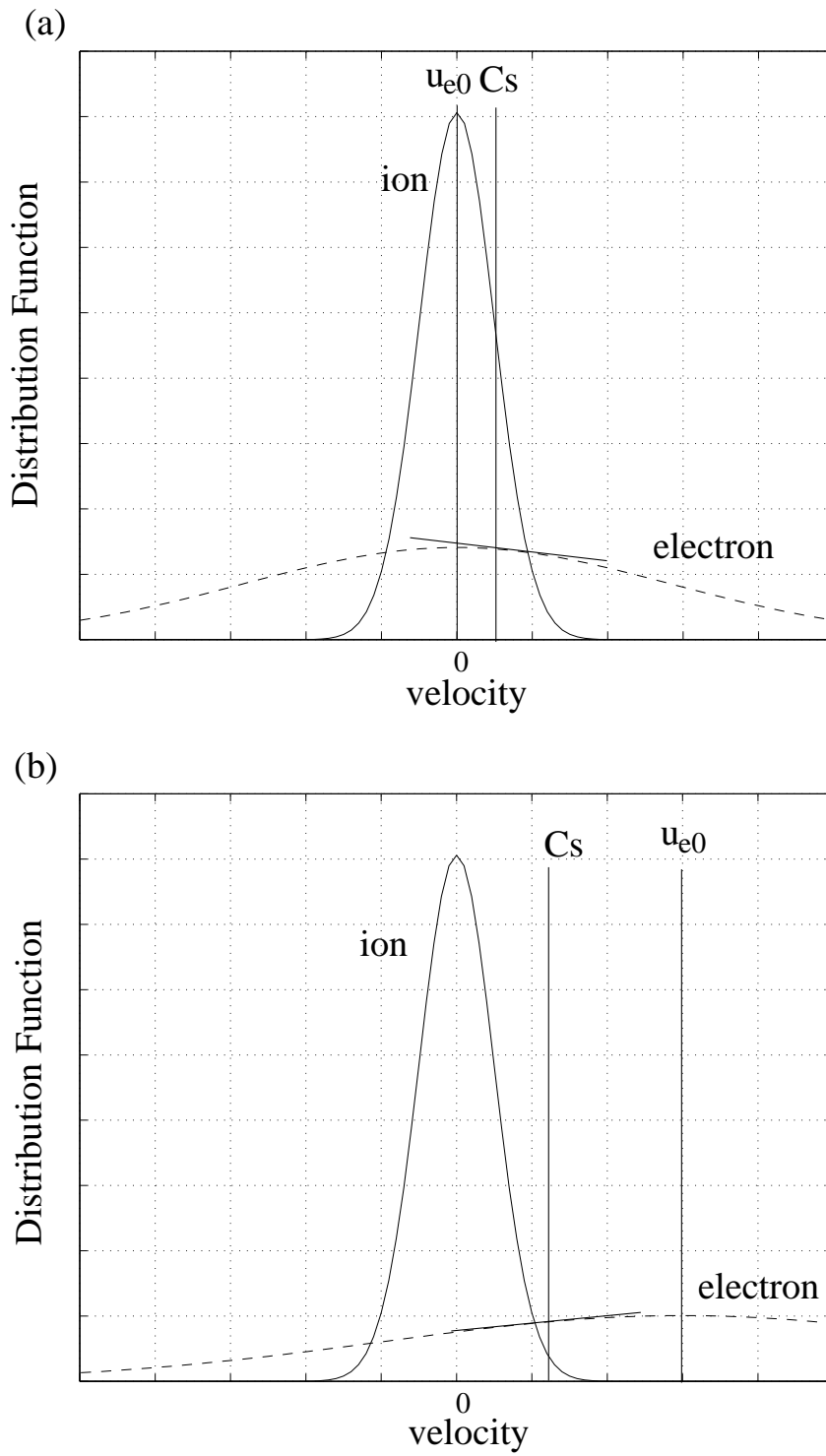


Figure 1.6: Electron and ion distribution functions for **a** $u_{e0} < C_s$, and **b** $u_{e0} > C_s$.

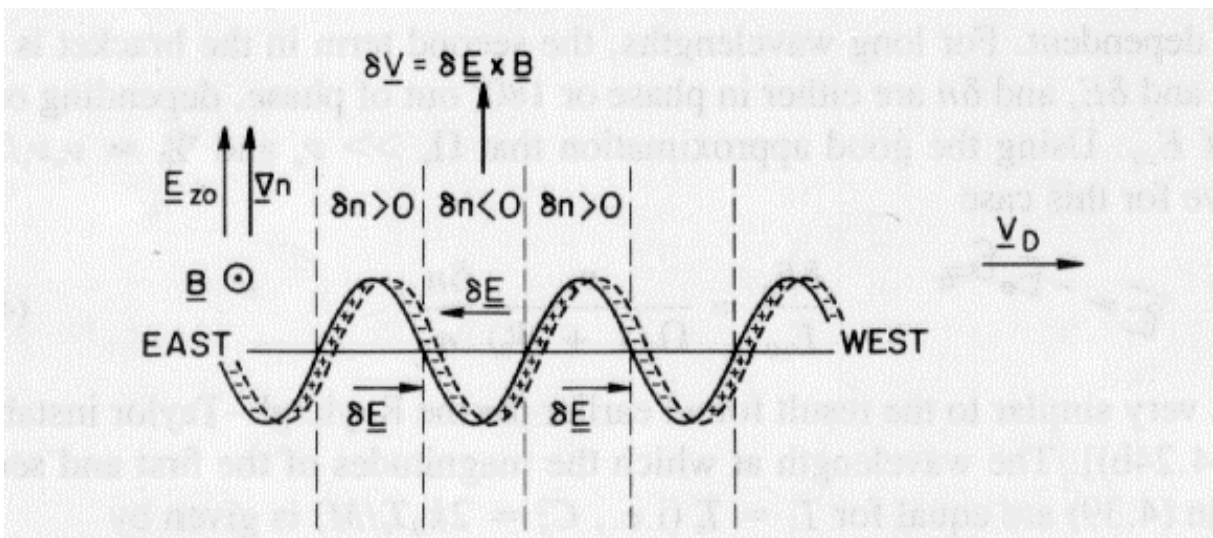


Figure 1.7: Schematic drawing of the mechanism of the gradient drift instability. After Kelley (1989), Fig. 4.31.

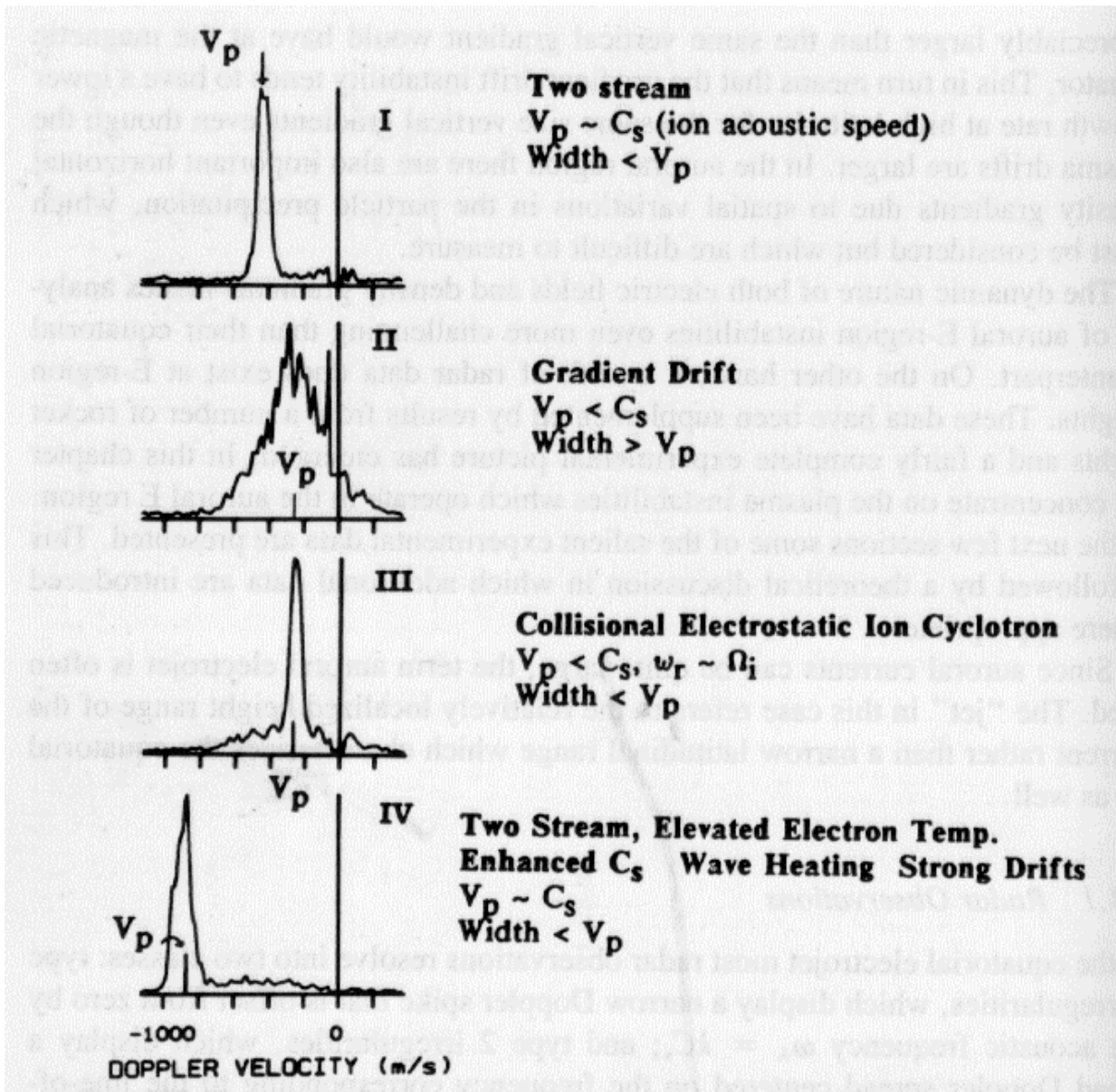


Figure 1.8: The four types of radar spectra that are observed in the auroral electrojet. After Kelley (1989) Fig. 8.27.

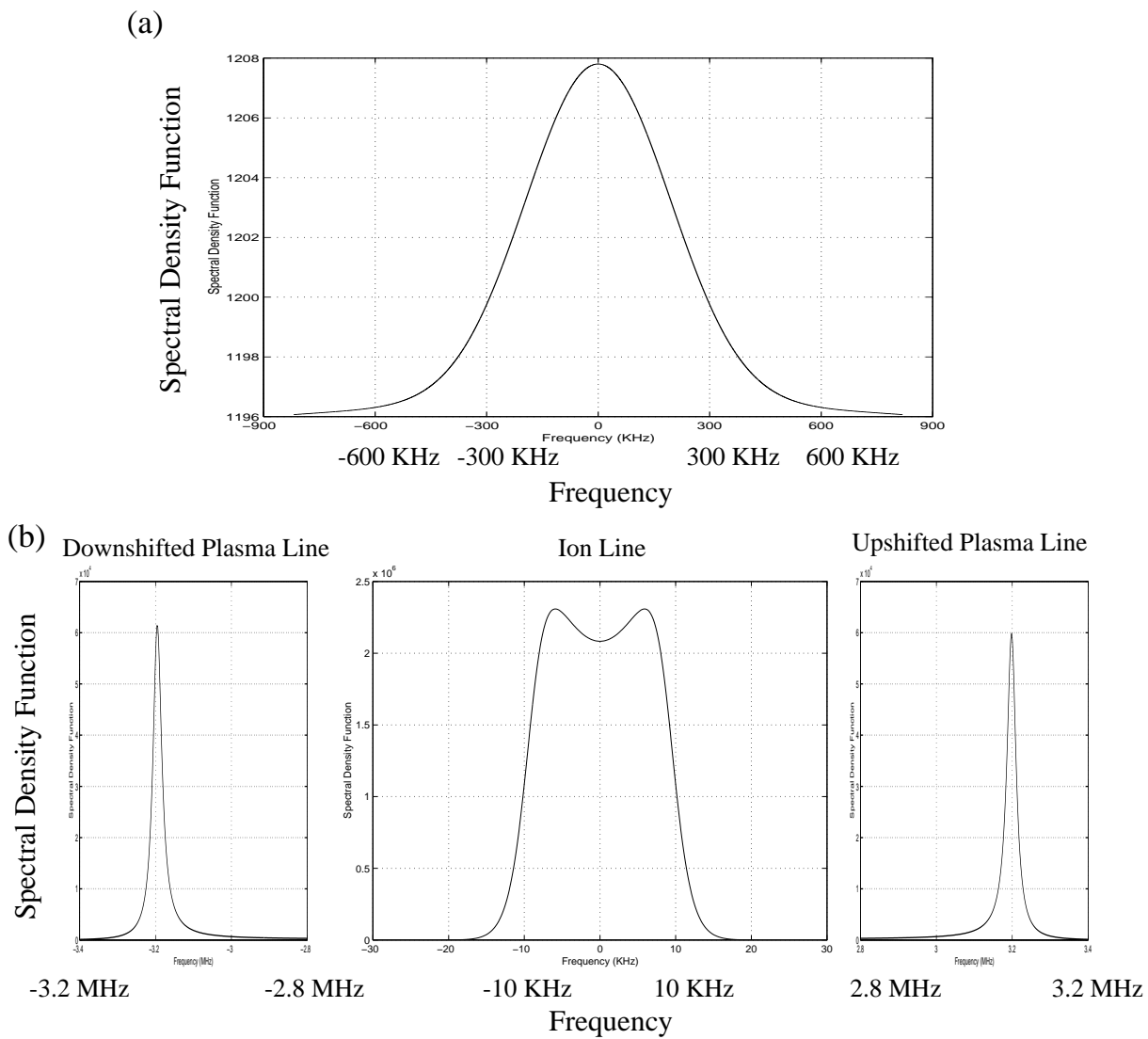


Figure 1.9: Schematic drawing of IS spectrum. **a** $k_{radar} \lambda_D \gg 1$, **b** $k_{radar} \lambda_D \ll 1$.

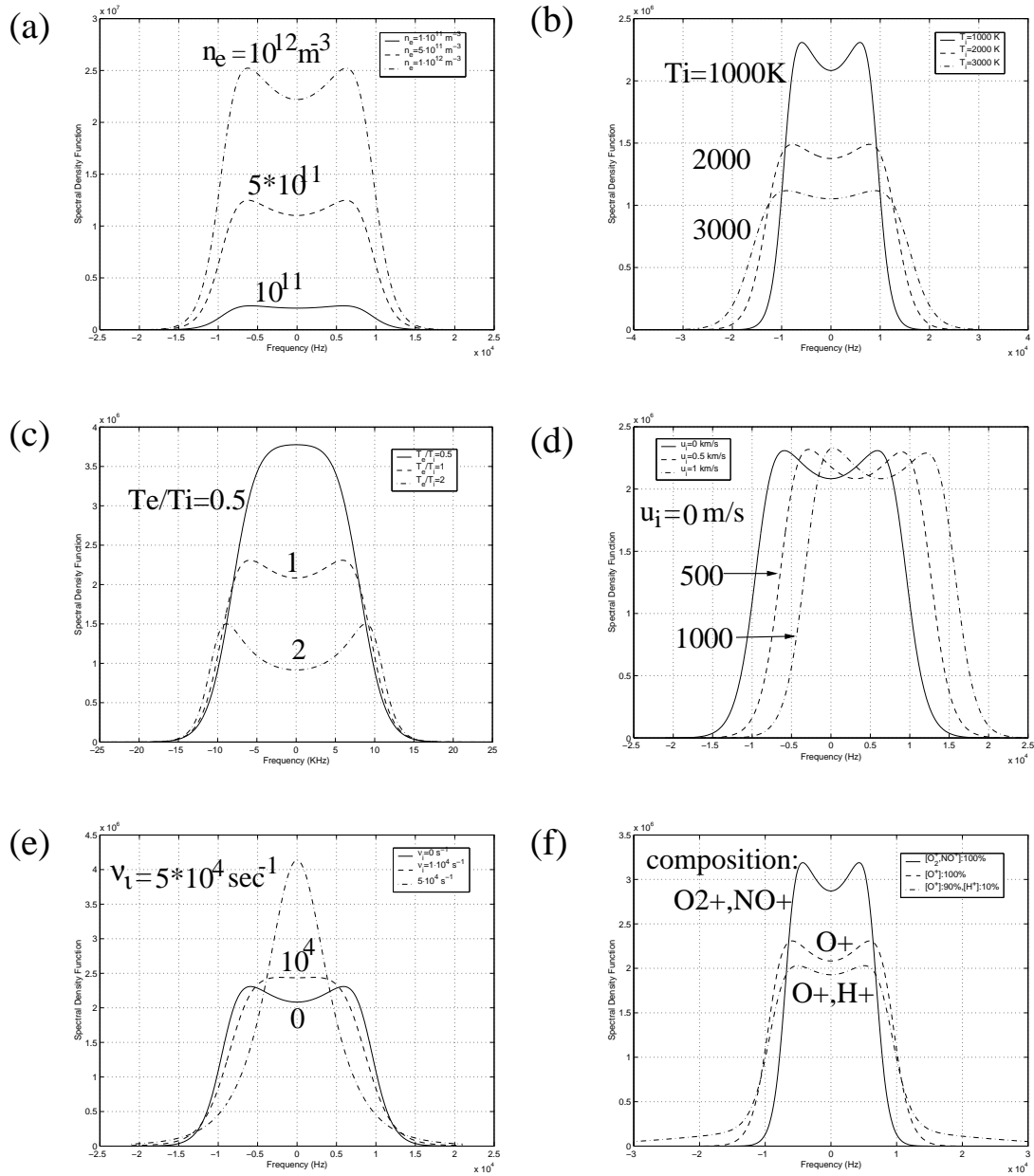


Figure 1.10: IS spectra with different parameters. When **a** n_e , **b** T_i , **c** T_e/T_i , **d** u_i , **e** v_{in} , and **f** ion composition are changed.

Chapter 2

Instruments

In this study, data obtained by the European Incoherent SCATter (EISCAT) radar system are mainly used. In addition, data from the Scandinavian Twin Auroral Radar Experiment (STARE) radars and from the Imaging Riometer for Ionospheric Studies (IRIS) at Kilpisjärvi, Finland, are used. In this chapter, these facilities are briefly described.

2.1 The EISCAT radar system

The EISCAT radar system is a set of incoherent scatter radars operated by the EISCAT Scientific Association supported by Finland, France, Germany, Japan, Norway, Sweden, and the United Kingdom. The EISCAT radar system consists of one tristatic radar system at UHF frequencies and one monostatic radar at VHF frequencies located in northern Scandinavia in the auroral zone, and two monostatic UHF radars in the Svalbard archipelago in the polar cap region. The transmitter of the tristatic radar system is located in Tromsø (69.58°N, 19.21°E), Norway, and its receiving antennas are located in Kiruna (67.86°N, 20.44°E), Sweden, and Sodankylä (67.37°N, 26.65°E), Finland, as well as in Tromsø. They operate at 933 MHz. These radars are all parabolic dishes (32 m diameter). This is the only IS radar system in the world which can determine the 3-dimensional ion velocity vector without any assumptions. At Tromsø, there is another VHF radar operating at 224 MHz. With its longer wavelength and large antenna aperture

(40×120 m cylindrical parabola), the VHF radar can reach the topside ionosphere at an altitude of more than 2000 km. This radar is also suitable for the D region study. The radars in Longyearbyen (78.15°N , 16.05°E), Svalbard, Norway, are two independent UHF radars both operating at 500 MHz called the EISCAT Svalbard Radar (ESR). One of them is a steerable parabolic dish (32 m diameter). The other is the latest antenna which has been in use since 2000, not steerable but fixed in the direction along the magnetic field line. It is a parabolic dish (42 m diameter) with better antenna gain. Geographical positions of the EISCAT radars are shown in Fig. 2.1.

By fitting a theoretical spectrum to a received spectrum, the EISCAT radars can derive n_e , u_i , T_i , T_e/T_i , ν_{in} , and, if the signal-to-noise ratio is very high, the ion composition. n_e , u_i , T_i can be derived at all the altitudes. The effect of T_e/T_i and ν_{in} are so similar that it is practically impossible to measure those two parameters at the same time. Therefore, above about 105 km where the electron-neutral collision is less important for IS spectra, T_e (or T_e/T_i) is fitted with a model ν_{in} . And below about 105 km where a large value of ν_{in} allows us to assume $T_e = T_i$, ν_{in} is derived. When the electric field is strong enough to heat electrons in the lower E region (down to ~ 100 km) as mentioned in Sec. 1.1.1, the boundary of the altitude must be changed to a lower altitude.

2.2 The STARE radar system

The STARE facility is operated jointly by Max-Planck-Institut für Aeronomie (MPAe) in Germany, and the Finnish Meteorological Institute (FMI) in Finland in cooperation with ELAB (the Technical University of Trondheim) in Norway. It consists of two coherent radars located at Midtsandan (63.6667°N , 10.73°E), Norway, and at Hankasalmi (62.3047°N , 26.6494°E), Finland. The radars operate at 140 MHz and 143.8 MHz, respectively, and measure the phase velocities of meter-scale field-aligned irregularities in the E region which are created by the plasma instabilities as mentioned in Sec. 1.2.2. Therefore, the disturbed conditions (a strong electric field) are suitable, and the echoes vanish when the electric field is too weak. Each radar has 8 beams, and the field of

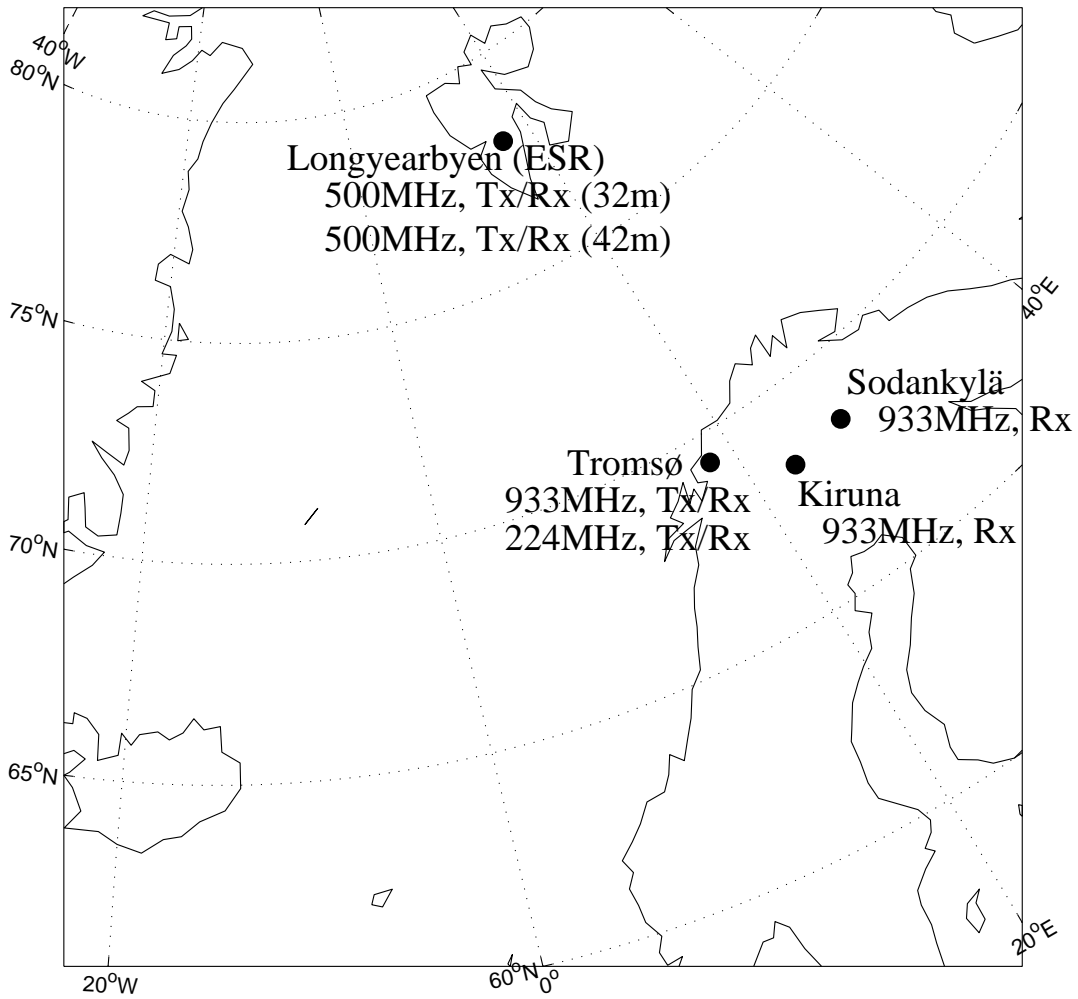


Figure 2.1: Geographical locations of the EISCAT radars. Tx/Rx means that the radar both transmits and receives. Rx means that the radar only receives.

view commonly covered by the two radars is about $400 \text{ km} \times 400 \text{ km} \sim 160000 \text{ km}^2$ which covers northern Scandinavia including the ionosphere over EISCAT Tromsø. (Fig. 2.2) The beams are wide in the elevation, and they illuminate the ionosphere at almost all the altitudes. The radars detect signals from the point where the radar wave vectors are parallel to the irregularity wave vectors which are perpendicular to the local magnetic fields. By combining the velocities measured at common volumes, the two-dimensional velocity field can be derived over the wide field of view. The phase velocities of the E region waves are thought to be approximately equal to the relative drift velocities between electrons and ions, $\mathbf{u}_d = \mathbf{u}_e - \mathbf{u}_i$. Since \mathbf{u}_i is almost zero in the lower E region due to very frequent collisions between ions and neutrals, \mathbf{u}_d is approximately equal to \mathbf{u}_e which is thought to drift at the local $\mathbf{E} \times \mathbf{B}$ velocity. Thus it approximates the two-dimensional map of the electric field that can be derived from the STARE radar system. When the condition $\mathbf{k}_{STARE} \perp \mathbf{B}$ is achieved at a slightly higher altitude than 110 km, however, contamination by the ion velocity causes the measured velocity to depart from the $\mathbf{E} \times \mathbf{B}$ velocity. It is also known that the STARE underestimates the $\mathbf{E} \times \mathbf{B}$ velocity when the electric field is strong ($\sim 17 \text{ mV/m}$), which is known as the saturation at the ion acoustic velocity (Nielsen and Schlegel, 1983, 1985; Robinson, 1993). These facts should be kept in mind when the velocities measured by STARE are interpreted.

2.3 The Kilpisjärvi IRIS System

IRIS is a modern version of a very sophisticated riometer. In contrast to the EISCAT and the STARE system described above, a riometer is a passive instrument which measures radio noise from extraterrestrial sources. When cosmic noise passes through the ionosphere, it is absorbed by ionospheric plasma. If the ionosphere is modified, for example, by an electron precipitation, the absorption is enhanced and, as a result, the observed cosmic noise becomes weaker. By comparing the observed noise power with the quiet-day curve (QDC) which represents the power without ionospheric absorption, the absorption is obtained in dB. Cosmic noise is absorbed most effectively in the D region where elec-

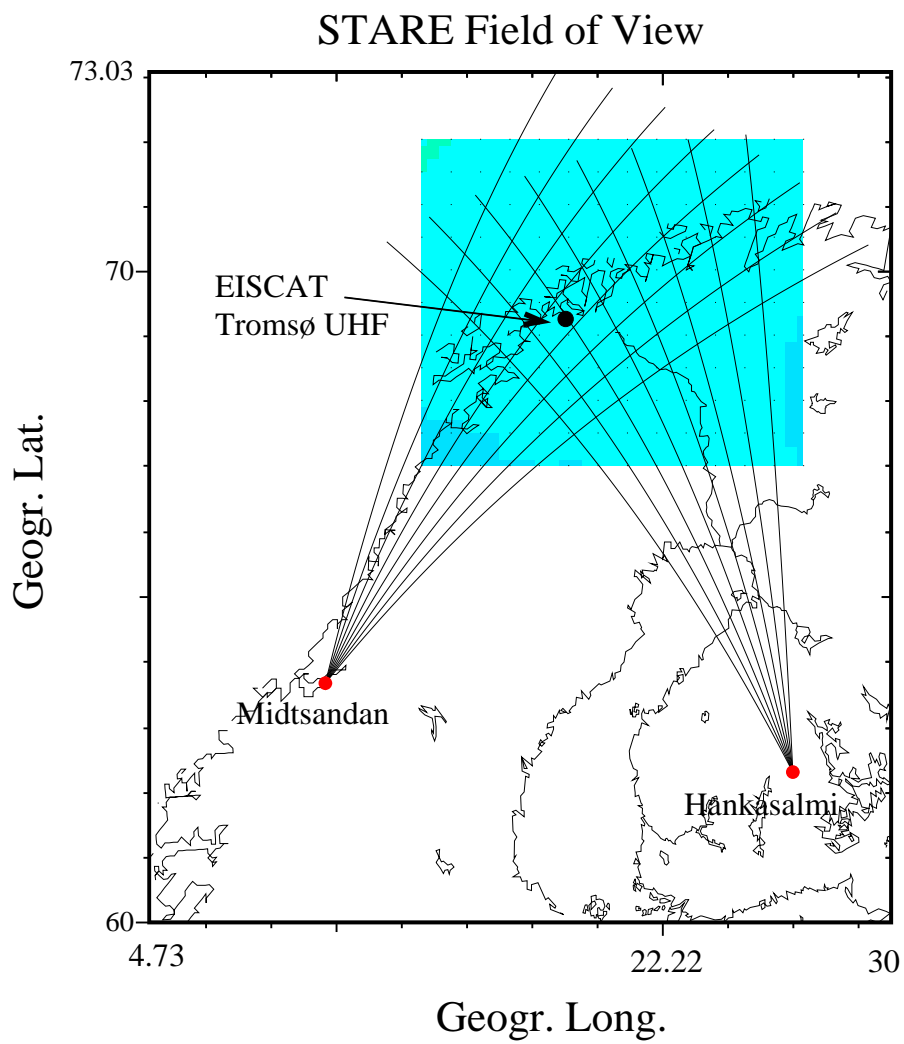


Figure 2.2: The STARE field of view. The position of the EISCAT Tromsø beam at field-aligned direction is also plotted.

trons collide very often with neutrals. IRIS consists of a square array of antennae. It produces an array of antenna beams which covers a wide field of view and enables us to obtain a two-dimensional snapshot image of ionospheric absorption.

The Kilpisjärvi IRIS system is supervised by Lancaster University, UK, and operated in conjunction with Sodankylä Geophysical Observatory (SGO), Finland. It is located in Kilpisjärvi (69.05°N, 20.79°E) in northern Finland. It operates at 38.2 MHz and produces an array of 49 beams. The projection of beams onto the ionosphere at 90 km is shown in Fig. 2.3. Each beam is numbered from 1 to 49 from the northeast corner to the southwest corner as shown in Table 2.1. The projection of the beam of the EISCAT Tromsø UHF radar at a field-aligned position (Azimuth 183.2°, Elevation 77.3°) at 90 km is in beam 9.

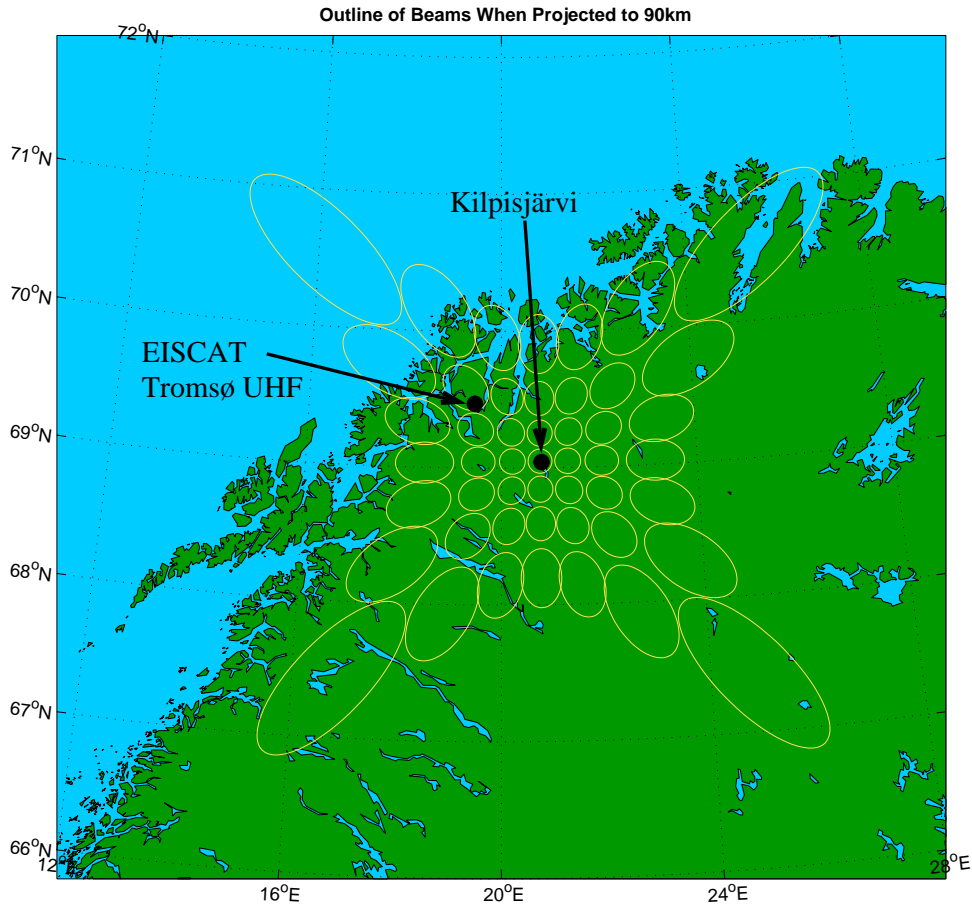


Figure 2.3: The projection of Kilpisjärvi IRIS beams onto the ionosphere at 90 km altitude. The outline is the locus at which the sensitivity is 3 dB lower than at the beam center. (From IRIS homepage <http://www.dcs.lancs.ac.uk/iono/iris> <http://www.dcs.lancs.ac.uk/iono/iris/>) The position of the EISCAT Tromsø beam at a field-aligned direction is also plotted.

North								
	1	2	3	4	5	6	7	
	8	9	10	11	12	13	14	
	15	16	17	18	19	20	21	
West	22	23	24	25	26	27	28	East
	29	30	31	32	33	34	35	
	36	37	38	39	40	41	42	
	43	44	45	46	47	48	49	
South								

Table 2.1: Number of each IRIS beam.

Chapter 3

E region

In this chapter, we deal with interactions between the ionospheric plasma and electrostatic waves in the E region. We take up an electron temperature enhancement phenomenon which is often observed in the lower E region and is believed to be resulted in by plasma waves excited by a strong electric field. In Sec. 3.1, we show the results of tristatic electron temperature measurements in the lower E region. This section is mostly a reproduction of Saito *et al.* (2001). Next, in Sec. 3.2, we consider the energy balance of electrons and parameterize the effects of waves by the anomalous (or effective) electron collision frequency, ν_e^* . We interpret ν_e^* into a rotation angle of an electron velocity vector from $\mathbf{E} \times \mathbf{B}$ direction, and discuss its relationship with a flow angle difference between $\mathbf{E} \times \mathbf{B}$ direction measured by the EISCAT and plasma flow velocity vector observed by the STARE system. This section mainly consists of Buchert and Saito (1997) and its extension. Finally, in Sec. 3.3, we examine the nature of ν_e^* . The cosmic noise absorption is selected as one example. By referring to data from the Kilpisjärvi IRIS, we make one aspect of ν_e^* clear.

3.1 Interaction Between the Farley-Buneman Wave and Electrons

3.1.1 Introduction

The knowledge and understanding of irregularities in the E region was recently reviewed (Sahr and Fejer, 1996). Usually dominant is the modified two-stream (or Farley-Buneman) instability (MTSI). It causes echoes in the HF and VHF ranges at angles nearly perpendicular to the geomagnetic field. Radars like the STARE and also SuperDARN detect such echoes and measure geophysical parameters such as the electric field. Understanding of the non-linear plasma physics involved in the MTSI is not only essential for the correct analysis of these radar data. The unstable E region is also an important natural example of plasma turbulence.

The plasma in the E region is strongly influenced by collisions between charged and neutral particles. This normally enforces thermal equilibrium below about 110 km, i.e., temperatures of neutrals, ions, and electrons, T_n , T_i , and T_e , respectively, are equal. Only at higher altitudes selective heat sources, like frictional heating of the ions, precipitating particles, or ionizing solar radiation, can easily raise T_i or T_e above T_n . Therefore, strong enhancements of T_e higher than 1000 K below 110 km, first reported by Schlegel and St.-Maurice (1981) using the Chatanika, were unexpected. Further observations were done with the EISCAT radar (Igarashi and Schlegel, 1987; Williams *et al.*, 1990; Jones *et al.*, 1991). Davies and Robinson (1997) also showed the electron heating in the E region on a statistical basis using 900 hours of EISCAT CP-1 and CP-2 data. Generally it was found that T_e starts to increase when the electric field strength $|\mathbf{E}|$ exceeds the threshold for excitation of the MTSI, E_{th} . T_e increases approximately linearly with $|\mathbf{E}| - E_{th}$.

Above ~ 90 km, the Joule (or frictional) heating of electrons are very small because $\nu_{en} \ll \Omega_e$. In the lower E region, precipitating particles can raise T_e by typically only 20–50 K (Schlegel and St.-Maurice, 1981) which is quite insufficient to explain the measured T_e enhancements of more than 1000 K. St.-Maurice *et al.* (1981) first realized that the

electron heating is due to electrostatic waves generated in the MTSI. Schlegel *et al.* (1983) has shown that E region electron temperature profiles obtained with a rocket experiment in Antarctica are in very good agreement with theoretical electron temperatures estimated with a heating model by unstable plasma waves suggested by St.-Maurice and Schlegel (1982). From in-situ observations with rockets Primdahl and Bahnsen (1985) argued that the heating can be explained by assuming an anomalous collision frequency ν^* applying to the electrons drifting in the background electric field. ν^* parameterizes all macroscopic effects due to waves. Also Robinson (1986) put forward a more self-consistent model where all macroscopic effects can be parameterized by a ν^* representing collisions between electrons and “plasmons”. The model is supported by mean-field turbulence theory (Sudan, 1983) and was further extended (Robinson and Honary, 1990). Ogawa *et al.* (1980) has shown that when the electric field is strong, the effective collision frequency of electrons should be enhanced by a factor of 6 to explain the observed aspect angle dependence of phase velocities of E region irregularities. Because the wave fronts seen at VHF frequencies are close to field-aligned, Farley (1985) has argued that the ν^* applies only to the field-perpendicular direction. The E region turbulent transport coefficient should be strongly anisotropic.

The in-situ observed VHF wave amplitudes and density fluctuation are often too weak to explain the heating rates derived from radar observations if the electrons are driven in the perpendicular direction only. St.-Maurice and Laher (1985) postulated therefore the existence of a small wave field component parallel to the magnetic field, $\delta\mathbf{E}_{\parallel}$. This would greatly enhance the average Joule heating rate

$$\begin{aligned} W_e &= \langle \delta\mathbf{j}_{\perp} \cdot \delta\mathbf{E}_{\perp} \rangle + \langle \delta\mathbf{j}_{\parallel} \cdot \delta\mathbf{E}_{\parallel} \rangle \\ &= \sigma_P \langle \delta E_{\perp}^2 \rangle + \sigma_{\parallel} \langle \delta E_{\parallel}^2 \rangle \end{aligned} \quad (3.1)$$

because the parallel conductivity σ_{\parallel} is much bigger than the Pedersen conductivity σ_P , $\sigma_{\parallel} \gg \sigma_P$. The existence of $\delta\mathbf{E}_{\parallel}$ was noted as an open question in the text book by Kelley (1989).

Experimental studies of anisotropy so far concentrated on the waves by using radar

backscatter from the ground. VHF radar echoes are observed at angles further away from perpendicularity to the earth's magnetic field than expected from linear theory. Also at higher frequencies, 930 MHz, the backscattering is not only surprisingly strong, but occurs at aspect angles even further away from perpendicular (Moorcroft *et al.*, 1988; Eglitis *et al.*, 1996). Obviously the E region plasma turbulence becomes more isotropic at shorter wavelengths.

In this work we search for a directional dependence of the electron temperature during heating event using tristatic EISCAT UHF radar. If we find anisotropic temperatures, the heating would have to be caused by perpendicular wave fields directly because electron-neutral collisions heat isotropically irrespective of the direction of \mathbf{E}_0 and $\delta\mathbf{E}$. On the other hand, the finding of isotropic temperatures would be consistent with St.-Maurice's model as well as with Robinson's electron-plasmon scattering. However, for the latter viewpoint, a finding of isotropic temperatures implies restrictions which will be discussed later in this work. Thus our analysis can potentially help to decide between two hitherto indistinguishable interpretations of experimental results.

In the next section, we present a comparison of electron temperatures measured with different aspect angles to the geomagnetic field, \mathbf{B} . In Sec. 3.1.3 we interpret the results of Sec. 3.1.2 and discuss the implementation on the E region plasma turbulence.

3.1.2 Tristatic Observation of Electron Temperatures by EISCAT

Fig. 3.1 shows a summary of the data obtained by the EISCAT CP-1-I experiment from 1200 to 1700 UT on June 12, 1990 when we found several distinctive T_e enhancement events. The antenna of the transmitting and receiving site in Tromsø, Norway, was directed along \mathbf{B} . The remote antennas in Kiruna, Sweden, and Sodankylä, Finland, measured alternately a common volume at 278 km altitude for electric field determination and six common volumes in the E region that can be used to detect any plasma anisotropy. The dwell times of the remote antennas are 50 to 60 sec. For E region measurements, the

Tromsø site uses a five-pulse code with a range resolution of approximately 3 km. The remote sites receive a long pulse of 350 μsec . The height resolution of the remote data is determined by the antenna beam width which is 0.8° . In the E region, this corresponds to approximately 2.9 km for the Kiruna antenna and 5.5 km for Sodankylä. Thus the height resolutions of both Tromsø and remote data are comparable.

During a period shown in Fig. 3.1, the electric fields measured in the F region are generally high, except after 1555 UT. Strong electron heating between 100 and 115 km with amplifications at around 1240, 1450, and 1515 UT are associated with high $|\mathbf{E}|$. In the most intense event T_e reaches about 1700 K between 1454 and 1455 UT. Ions are heated up by frictional (Joule) heating above 115 km. The electron temperatures in the lower E region below about 115 km are generally enhanced over both the neutral and ion background temperatures.

Using the E region measurements from the remote EISCAT sites, we have checked the thermal isotropy of the electrons and also the ions. Figs. 3.2 and 3.3 show scatter plots of temperatures obtained simultaneously from two different sites using all the data from 0800 UT, June 12 to 1345 UT, June 13, 1990. At 108 km the aspect angle of the Sodankylä data is 39° , while that of Tromsø is 0° . In Fig. 3.2a the electron temperatures from these two directions are compared with each other. At the highest T_e of 1700 K observed by Tromsø, no simultaneous observation by the remote sites is available at this altitude, therefore the plotted T_e reaches only about 1100 K. In Fig. 3.2b the ion temperatures from the two sites are compared. The comparisons of the electron and the ion temperatures at 108 km between Tromsø and Kiruna where the aspect angle is 35° are shown in Fig. 3.3a and 3.3b, respectively. Occasionally some preferentially transverse ion heating seems to occur even at this low altitude, but to a much lesser degree than the electron heating. The important point in this context is that the plots indicate clearly the isotropy of T_e at all temperatures. Although not shown here, comparisons at other altitudes are similar.

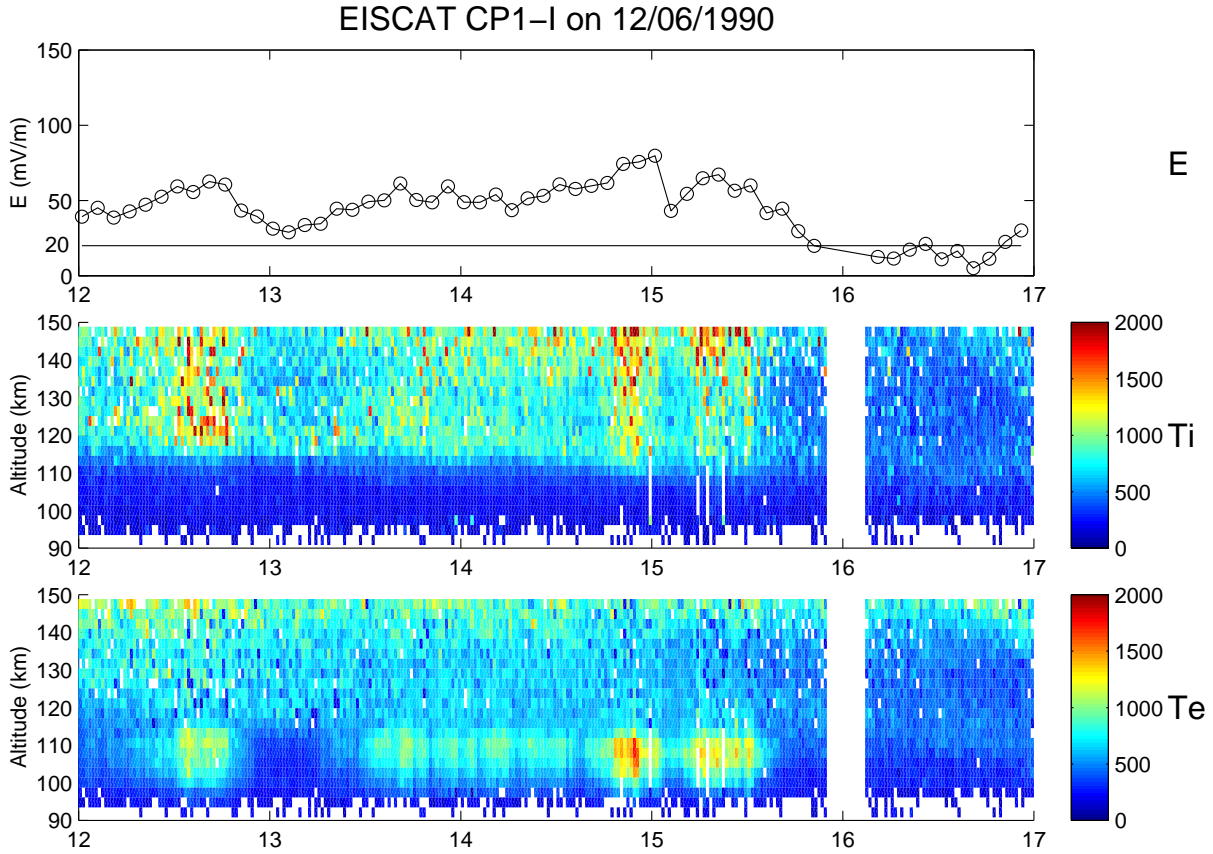


Figure 3.1: Overview of a data set with long periods of elevated T_e in the lower E region. The top panel shows $|\mathbf{E}|$ with a time resolution of 5 minutes. The approximate threshold of the MTSI is about 20 mVm^{-1} . The middle and bottom panels show the electron and ion temperatures, respectively.

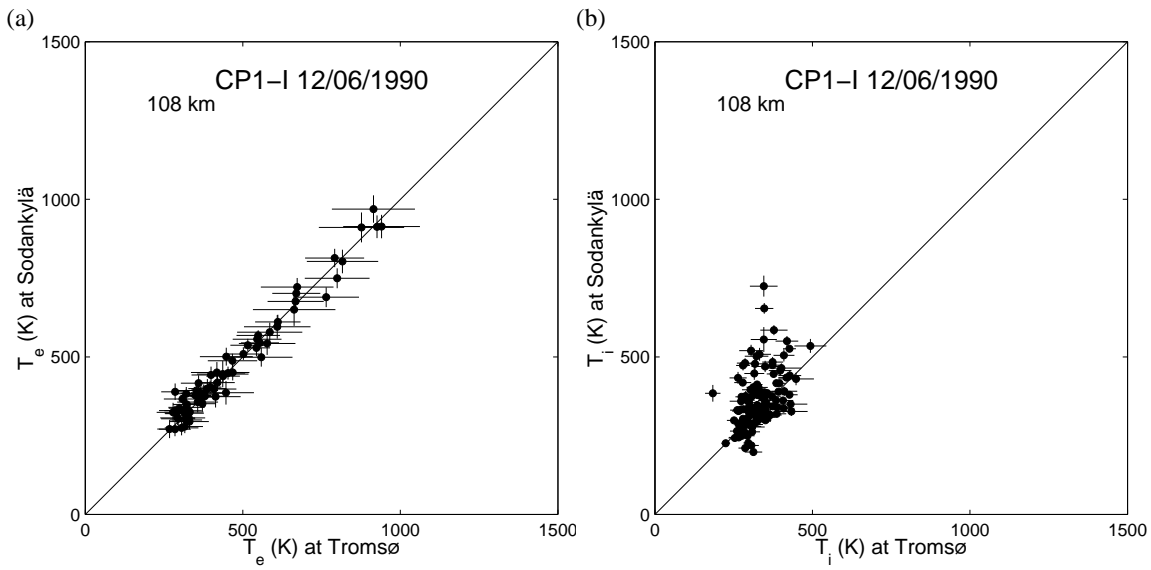


Figure 3.2: **a** Scatter plot of the electron temperatures from different aspect angles observed with the Tromsø and Sodankylä EISCAT sites. The errors in fitting to the IS spectra are also plotted. **b** The same as **a**, but the ion temperatures are compared.

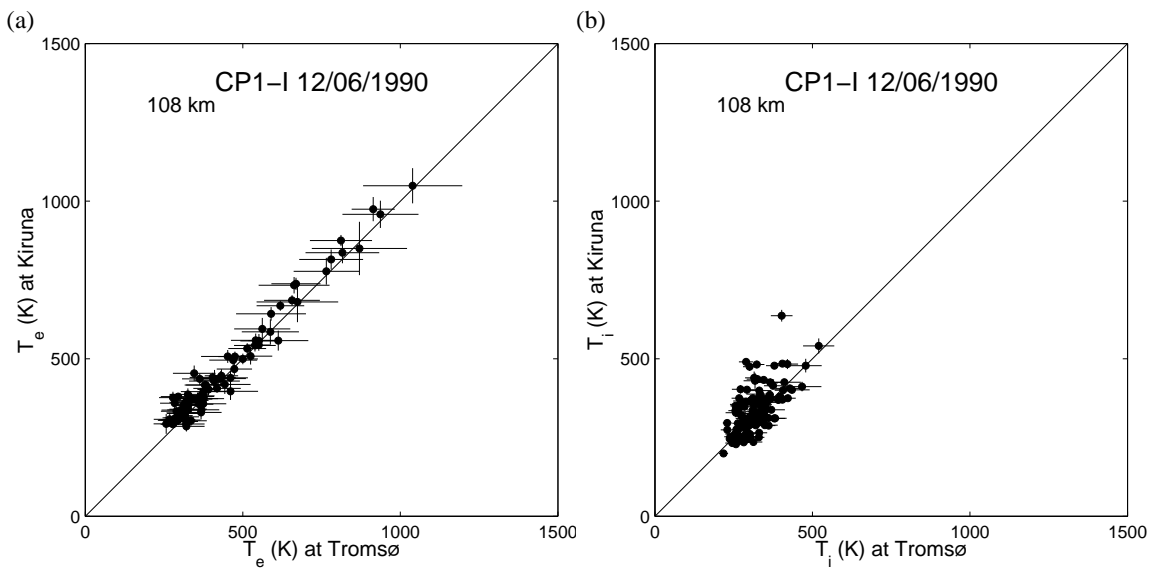


Figure 3.3: The same as Fig. 3.2, but Tromsø and Kiruna data are compared.

3.1.3 Discussion

The E region plasma waves, which are assumed to be the cause of electron heating, are highly anisotropic with respect to \mathbf{B} . From coherent radar observations it is known that at wavelengths above about a meter the back-scattered wave amplitudes fall off within aspect angles of about 2° away from the magnetic field. From this, one might expect anisotropic electron temperatures. Nevertheless, our results show that the T_e enhancement is clearly isotropic.

If electrostatic waves heat electrons directly, the wavelengths must be smaller than the electron gyroradius r_g (~ 1 cm). Otherwise the wave-particle interaction is ineffective in giving electrons enough energy to heat them up. For long wave lengths ($\gg r_g$) and low frequencies (\ll the electron gyrofrequency $\Omega_{ce} \sim 9$ MHz) the electrons perform alternating, deterministic $\mathbf{E} \times \mathbf{B}$ drifts. In-situ observations show that the wave amplitudes at shorter wavelengths decrease substantially (Pfaff *et al.*, 1984). Extrapolating this trend to (unobserved) cm wavelengths, we find that direct heating by such waves is an unlikely explanation for our observed isotropic enhancements of T_e .

When taking into account also electron-neutral collisions, the strong but slow and anisotropic Farley-Buneman waves can lead to isotropic electron heating. The electrons' deterministic $(\mathbf{E} + \delta\mathbf{E}) \times \mathbf{B}$ drift gets in each elastic collision with a neutral completely and isotropically randomized. Due to the huge mass difference between electrons and neutrals, an electron loses practically no energy in elastic collisions, but the energy is converted from flow energy to heat. About every 100th collision with a neutral is inelastic, exciting vibrational and rotational modes of N_2 and O_2 molecules as well as fine structure levels of O (Schunk and Nagy, 1978). In an inelastic collision, the electron transfer typically a large fraction of its energy to the neutrals. The efficiency of this processes enforces that T_e gets hardly elevated above neutral temperature in the lower E region even when there are DC electric fields of the order of 100 mV/m (which is typical for the auroral zone). The amplitudes of Farley-Buneman waves δE do not become larger than the DC background field even in the non-linear stage of the instability. Therefore purely per-

pendicular waves cannot explain the large observed enhancements of T_e . Consequently St.-Maurice (1987) postulated a field-parallel component of $\delta\mathbf{E}$, $\delta\mathbf{E}_{\parallel}$, which would heat electrons very efficiently due to high parallel transportability as discussed in the introduction. Our observation of isotropic T_e enhancements is in accordance with St.-Maurice's model, although we cannot add any quantitative estimates of the size of $\delta\mathbf{E}_{\parallel}$.

3.2 Energy Balance of Electrons: Pedersen Current Carried by Electrons

3.2.1 Introduction

It is obvious that electron heating must be associated with dissipative currents. In the literature, electrons are said to drift in a $\mathbf{E} \times \mathbf{B}$ direction which is dissipationless Hall drift. Therefore, there must be an additional dissipative current which is carried by electrons. Robinson (1993) has also pointed out that due to the drag effect of the waves the electron drift motion should depart from $\mathbf{E} \times \mathbf{B}$ drift. Although his approach is based on a concept of a microscopic electron-plasmon collision, it is basically the same as ours from the point of view that electromagnetic energy must be dissipated. In our hypothesis, microscopic heating processes are in fact in a black box. Instead of going into the details of microscopic heating processes, we parameterize all the heating effects of waves by a dissipative electron drift.

To accomplish this, a first task is to obtain an estimate of the true average azimuthal direction of the electron drift. Haldoupis *et al.* (1993) compared the observed azimuthal direction of VHF wave fronts with the $\mathbf{E} \times \mathbf{B}$ direction and found systematic differences up to 20 deg. We would expect a similar result with the electron drift. Here, we first estimate how much the deviation of electron drift velocity could be based on observed electron temperatures. The isotropy of T_e shown in Sec. 3.1 allows us to assume that the T_e measured by the EISCAT Tromsø radar in the field-aligned direction applies in all directions. We then try to compare the electron drift with results obtained by STARE as

Haldoupis *et al.* (1993) has done.

3.2.2 Methods

Our new method is based on measurements of the electron temperature T_e . Electron heating is observed regularly over several minutes, and to a certain extent, it can be described as a stationary process. Therefore, the dissipative currents must be rather stationary and similar to classical Pedersen currents. The local heating rate of electrons must be equal to $\mathbf{j} \cdot \mathbf{E}$.

Now we start from the momentum equation of electrons and ions (Eq. (1.21)). Because we are interested in low frequencies and large scales, we set the left-hand-side of Eq. (1.21) to 0. We also neglect the pressure gradient force. Since the energy to heat electrons is extracted from the relative drift between electrons and ions, or the DC electric field, the waves should act as a kind of drag force against the electron drift. We then assume as external forces \mathbf{F}' , and we introduce

$$\mathbf{F}' = -n_e m_e \nu_{en} \mathbf{u}_e - n_e m_e \nu_e^* (\mathbf{u}_e - \mathbf{u}_i) \quad (3.2)$$

for electrons, and

$$\mathbf{F}' = -n_e m_i \nu_{in} \mathbf{u}_i - n_e m_i \nu_i^* (\mathbf{u}_i - \mathbf{u}_e) \quad (3.3)$$

The first term of each equation represents a frictional force with neutrals. For electrons, since $\nu_{en} \ll \Omega_e$, the effect is rather small. And we have assumed $\mathbf{u}_n = 0$. The last terms of each equation represent the momentum exchange between ions and electrons which are anomalously enhanced due to waves and turbulence. Because the effects of electrostatic waves mostly originate in forces between ions and electrons, they should appear as terms which represent interaction between ions and electrons. ν_e^* and ν_i^* include both classical and anomalous interactions between ions and electrons,

$$\nu_e^* = \nu_{ei} + \nu_{ei}^* \quad (3.4)$$

$$\nu_i^* = \nu_{ie} + \nu_{ie}^* \quad (3.5)$$

where ν_{ei} and ν_{ie} are the classical electron-ion and ion-electron collision frequencies which are usually much smaller than ν_{en} and ν_{in} , respectively, and ν_{ei}^* and ν_{ie}^* are the anomalous (or effective) electron-ion and ion-electron collision frequencies which are assumed to describe effectively the effects of waves and turbulences, respectively. Whatever the microprocesses of waves are, contributions of waves and turbulences to the total momentum balance in the system must be in these forms, if $\nu_{ei,ie}^*$ can effectively parameterize them. These drag forces should be internal forces and should cancel each other out. This requires

$$\nu_i^* = \frac{m_e}{m_i} \nu_e^* \quad (3.6)$$

The anomalous collision frequency for ions is much less than that for electrons. But it can be dominant over ν_{in} when ν_e^* is strongly enhanced.

For a steady state, the electron heating rate is equal to the electron cooling rate. According to Poynting's theorem, the divergence of the electromagnetic energy is equal to $\mathbf{j} \cdot \mathbf{E}$. From Eq. (1.6), the energy balance of electrons becomes

$$\mathbf{j} \cdot \mathbf{E} = L_{e,el} + L_{e,in} + L_{e,ion} \quad (3.7)$$

where $L_{e,in}$ represents all the cooling rates per unit volume due to inelastic collisions with neutrals. Jones *et al.* (1991) and also Buchert and Saito (1997) used only the first two terms on the right-hand-side of this equation. As those authors above did, we use the model for the first two terms which are given in Schunk and Nagy (1978) in which isotropic electron temperatures are assumed. We can take this model, since we know from Sec. 3.1 that T_e is isotropic even when T_e is strongly enhanced. For the last term, the cooling rate by ions, based on the analogy of the cooling rate of ions by electrons (the second term of Eq. (1.3)), is given by

$$L_{e,ion} = 2n_e \frac{m_e}{m_e + m_i} \nu_e^* \frac{3}{2} k_B (T_e - T_i) \quad (3.8)$$

It should be noted that the current density \mathbf{j} which is effective in heating electrons is essentially carried by electrons, because the ultimate energy source is the DC electric field which is applied to the ionosphere from the magnetosphere and drives electrons in a

$\mathbf{E} \times \mathbf{B}$ direction at the zero-th order. At ~ 108 km where observed electron temperature enhancements are strongest, we can assume $\mathbf{u}_i \sim \mathbf{u}_n \sim 0$ because $\nu_i n \gg \Omega_i$. Then a simpler equation can be used for the electron drift motion by just replacing ν_{en} by $\nu_{en} + \nu_e^*$ in the classical equation. This is the same as replacing κ_e in Eq. (1.8) by an anomalously enhanced one

$$\kappa_e^* = \frac{\nu_{en} + \nu_e^*}{\Omega_e} \quad (3.9)$$

and we obtain

$$\mathbf{u}_e = -\frac{\kappa_e^*}{1 + \kappa_e^{*2}} \frac{\mathbf{E}_\perp}{B} + \frac{1}{1 + \kappa_e^{*2}} \frac{\mathbf{E}_\perp \times \mathbf{B}}{B} - \frac{e}{m_e(\nu_{en} + \nu_e^*)} \mathbf{E}'_\parallel \quad (3.10)$$

Now let us assume there is no DC electric field parallel to \mathbf{B} . Since the second term of the right-hand-side of this equation is perpendicular to \mathbf{E}_\perp , only the first term contributes to electron heating. It carries the Pedersen currents which are, however, anomalously enhanced by the effects of waves and turbulences. The enhanced Pedersen currents which are carried by electrons are now given by

$$\mathbf{j}_{Pe} = n_e e \frac{\kappa_e^*}{1 + \kappa_e^{*2}} \frac{\mathbf{E}_\perp}{B} \equiv \sigma_{Pe}^* \mathbf{E}_\perp \quad (3.11)$$

where σ_{Pe}^* is the anomalously enhanced (or effective) Pedersen conductivity by electrons which is partly drifting in a $-\mathbf{E}$ direction due to effects of waves and turbulences. Finally we obtain the energy balance equation of the electrons

$$n_e e \frac{\kappa_e^*}{1 + \kappa_e^{*2}} \frac{|\mathbf{E}_\perp|^2}{B} = L_{e,el} + L_{e,in} + 2n_e \frac{m_e}{m_e + m_i} \nu_e^* \frac{3}{2} k_B (T_e - T_i) \quad (3.12)$$

This is valid as far as the ν_{ei}^* is concerned which is included in ν_e^* and can parameterize well the effects of waves and turbulences. This equation is a third-order equation of κ_e . Out of three possible solutions, one solution should be adopted which converges to ν_{en}/Ω_e when $|\mathbf{E}_\perp|$ is weaker than the threshold of the instability.

It should be noted that according to Poynting's theorem, $\mathbf{j} \cdot \mathbf{E}$ is equal to the divergence of the electromagnetic energy flux. Our argument in relation to the total energy balance is equivalent to that of Magnetosphere-Ionosphere (MI) coupling in which the electromagnetic energy is supplied from the magnetosphere to the ionosphere by the Field-Aligned-Currents (FACs) and dissipated by the Pedersen currents which close the FACs in the

ionosphere. The electron heating by plasma waves and the classical Joule heating can be macroscopically understood in the same frame of MI-coupling although their microscopic processes are quite different.

3.2.3 Observation

We have applied the method described above to data obtained by the EISCAT CP-1-K experiment on September 16, 1999. In contrast to the EISCAT CP-1-I used in Sec. 3.1, the remote antenna directions are fixed to the common volume in the F region which enables continuous observation of the three-dimensional ion velocity vector which can be regarded as the $\mathbf{E} \times \mathbf{B}$ plasma drift velocity vector, which enables us to determine the electric field. Overview plots between 0900 and 1600 UT are shown in Fig. 3.4. Below we use data obtained between 1100 and 1200 UT when the electric fields are strong and electrons are heated up in the lower E region.

The cooling rates in Eq. (3.7) are essentially functions of temperature differences. If we take the parameters of neutrals from the existing model, the MSIS-90 model (Hedin, 1991) in our study, the parameters to be supplied by measurements are T_i and T_e . Since we know that these temperatures are isotropic in the lower E region from the study in Sec. 3.1, or by Saito *et al.* (2001), we can use T_i and T_e measured by the EISCAT Tromsø radar along the magnetic field line. For a representative integration period, Fig. 3.5 (left panel) shows the height profiles of the observed T_e and T_i as well as T_n according to the MSIS90 model. Below 105 km where significant ion frictional heating is not expected, T_n is very close to T_i . This we take as an indicator of the accuracy of the MSIS-90 model for this specific time and place. Between 100 and 115 km, T_e is greatly enhanced with the maximum enhancements at 108 km. Above 111 km, T_i is enhanced by frictional heating. In Fig. 3.5(right panel), the profile of $\sigma_{P,e}^*$ is shown together with $\sigma_{P,i}$. The latter ion Pedersen conductivity is computed classically and $\sigma_{P,e}^*$ using (3.7). The contribution of $\sigma_{P,e}^*$ to the total height-integrated conductivity is only up to about 20 %. Relatively, however, $\sigma_{P,e}^*$ becomes significant below 110 km, and is comparable to $\sigma_{P,i}$. The flow

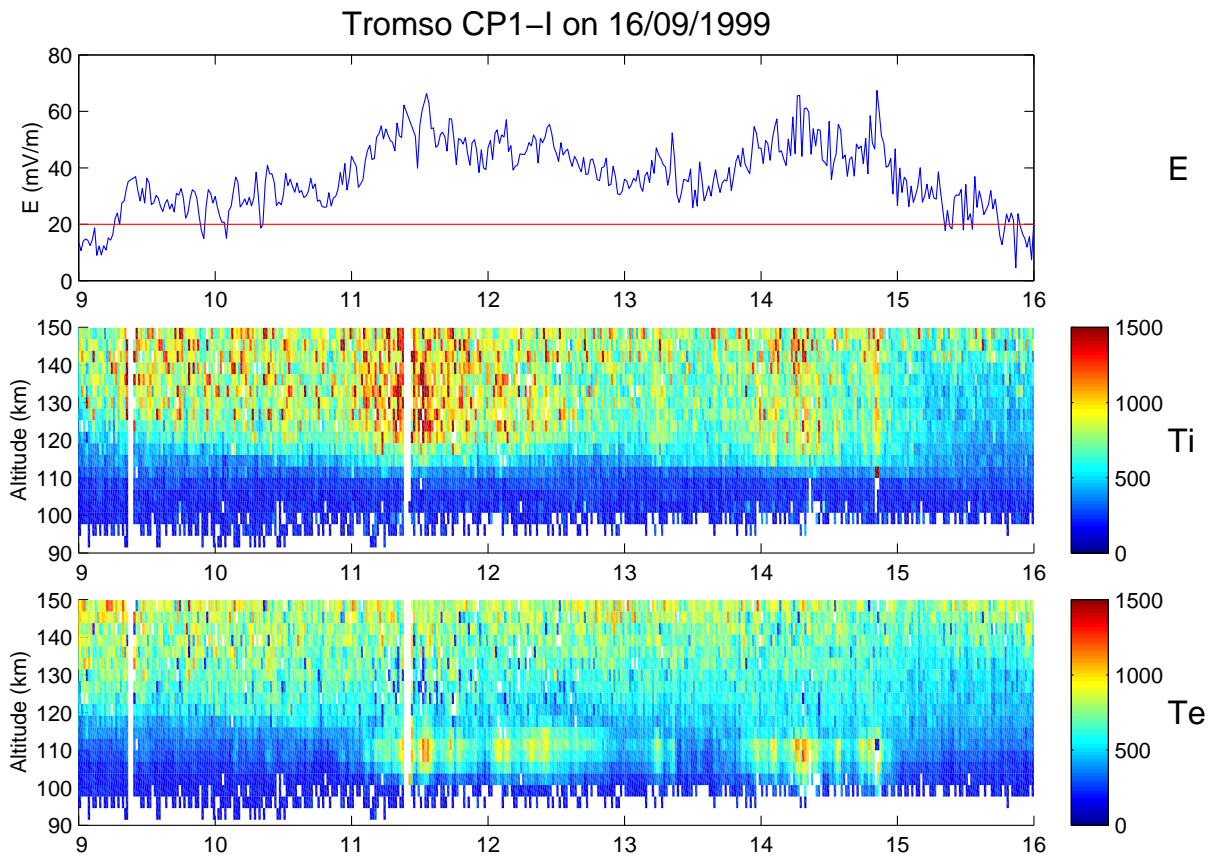


Figure 3.4: The same format as Fig. 3.1. But the electric field (top panel) is plotted with a 1 min resolution.

angle rotation decreases the Hall current by a factor of $1/(1 + \kappa_e^{*2})$. For the angle 7° , this factor is about 1.5 %, and the Hall current is almost unchanged by ν_{ei}^* .

In Fig. 3.6, estimated electron flow directions with respect to the $\mathbf{E} \times \mathbf{B}$ direction by using the procedure described in Sec. 3.2.2 are shown. Corresponding to the variation of the electric field strength and of the electron temperature, the flow angles change their value and become up to 7° which corresponds to $\nu_e^* \sim 30\nu_{en}$. In the same plot, we plot the flow angles estimated without the cooling effect of ions as Jones *et al.* (1991) and Buchert and Saito (1997) did. Compared to the case without taking the cooling rate by ions into account, the angles are markedly increased by factors of $1.5 \sim 2$. This can be understood as follows: Typically, $L_{e,el}$ is $0.05 \sim 0.1$ of $L_{e,in}$. $L_{e,ion}$ works basically in the same way as $L_{e,el}$. Therefore, without the waves and turbulences it should be very small because ν_{ei} is much smaller than ν_{en} . With the existence of the waves and turbulences, however, the effective collision frequency between electrons and ions is anomalously enhanced up to several tens times larger than ν_{en} . This leads to $L_{e,ion} \sim L_{e,in}$, and dissipated energy, and equivalently the flow angle with respect to the $\mathbf{E} \times \mathbf{B}$ direction is doubled compared to the case without the cooling rate by ions.

3.2.4 Discussion

In the previous section, we have estimated the rotation of electron velocity from a $\mathbf{E} \times \mathbf{B}$ direction to a $-\mathbf{E}$ direction based on the hypothesis that the effects of the waves and turbulences can be parameterized by anomalous (or effective) electron-ion collision frequency ν_{ei}^* . It is necessary to confirm the electron flow angle rotation by other independent methods. As Haldoupis *et al.* (1993) did, we compare the electron flow velocities estimated by our method with those derived from the STARE system.

As mentioned in Sec. 2.2, the STARE radars measure the line-of-sight velocities of 1 m scale irregularities. Assuming that the radars observe the line-of-sight projection of the velocity vector of the irregularities which are also assumed to be equal to the electron flow velocity (the so called *cosine rule*), the two-dimensional velocity vector can

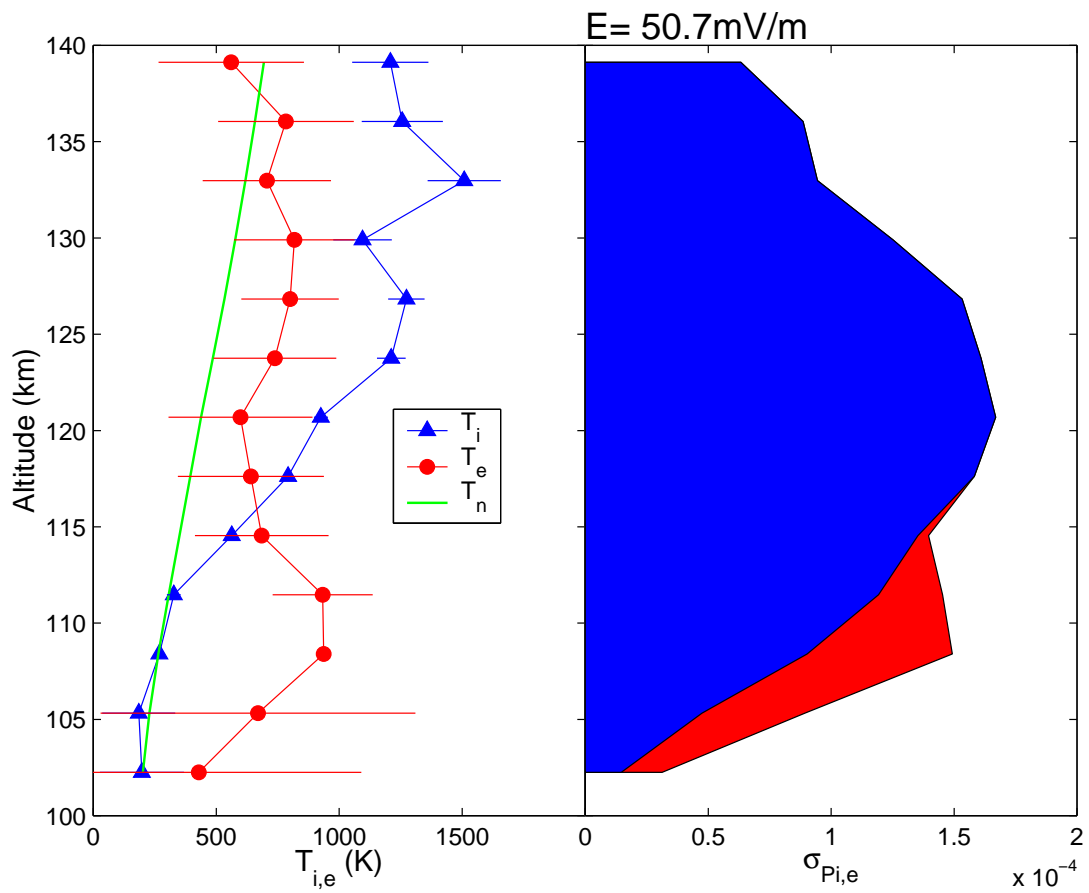


Figure 3.5: Height profile of (left) temperatures of ions, electrons and neutrals, and (right) Pedersen conductivity due to ions (blue) and electrons (red).

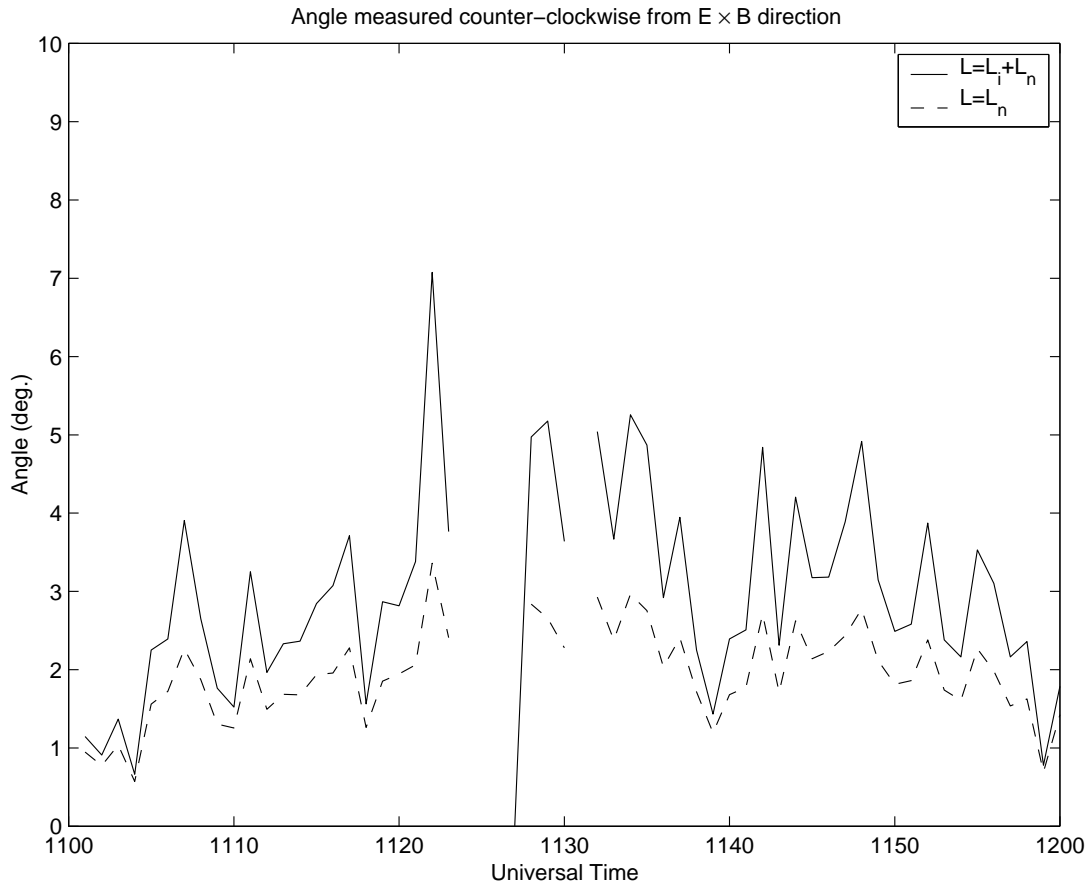


Figure 3.6: Electron flow angles relative to the $\mathbf{E} \times \mathbf{B}$ directions at 108 km are plotted. The flow angle is measured in a counter-clockwise direction (from $\mathbf{E} \times \mathbf{B}$ to $-\mathbf{E}$). Flow angles are calculated both with and without taking the cooling by ions into account (solid line and dashed line, respectively).

be reconstructed. Fig.3.7 shows an example of the STARE measurements. Red colors indicate strong echoes, and blue colors weak. The arrows show the direction and the magnitude of flow velocities. We select the data at the common volume of the STARE beams and the EISCAT Tromsø beam (field-aligned) in the lower E region. Since the electric field vector can be determined by the EISCAT measurements, the flow angle measured by the STARE system with respect to a $\mathbf{E} \times \mathbf{B}$ direction can be derived. In Fig. 3.8, the angles obtained from the STARE measurements are compared with those of our estimation. Although the directions of flow rotation are systematically the same, in the $-\mathbf{E}$ direction, the angles measured with the STARE are much larger than our estimation. This result can be understood by the following two reasons: First, the measured flow velocities can be contaminated by the ion velocity when $\mathbf{k}_{STARE} \perp \mathbf{B}$ is achieved at a slightly higher altitude than 108 km. The ion velocity rotates the relative drift velocity between electrons and ions in a counter-clockwise direction. Although we have not checked the altitude where $\mathbf{k}_{STARE} \perp \mathbf{B}$ is achieved, this explanation is quite probable because the ion velocity effect always gives a counter-clockwise flow angle rotation. Second, as pointed out and discussed by previous works (Nielsen and Schlegel, 1983, 1985; Robinson, 1993), the phase velocity of the MTSI waves is saturated at the local ion acoustic velocity C_s . When one of or both of the velocities measured by the two STARE radars is saturated, the velocity vectors derived by applying the cosine rule are no longer true electron velocity vectors. In this time period, the common volume is in the eastward electrojet (westward electron drift). Due to the geometry of the STARE system, radar beams of the Midstandan site may be in the unstable cone where the line-of-site electron drift velocities are faster than C_s more often than those of the Hankasalmi site. This leads to the consequence that the velocity saturation at C_s tends to rotate the flow vectors derived with the cosine rule in a counter-clockwise direction with respect to a $\mathbf{E} \times \mathbf{B}$ to a $-\mathbf{E}$ direction. Therefore, it is impossible to confirm our hypothesis by measurements using the STARE system.

One possible method of testing our estimation is to use a very high resolution camera which can detect meter-scale irregularities. Trondsen and Cogger (1997) has made such a camera which has a ~ 2 m resolution and is sensitive to emissions typically from around

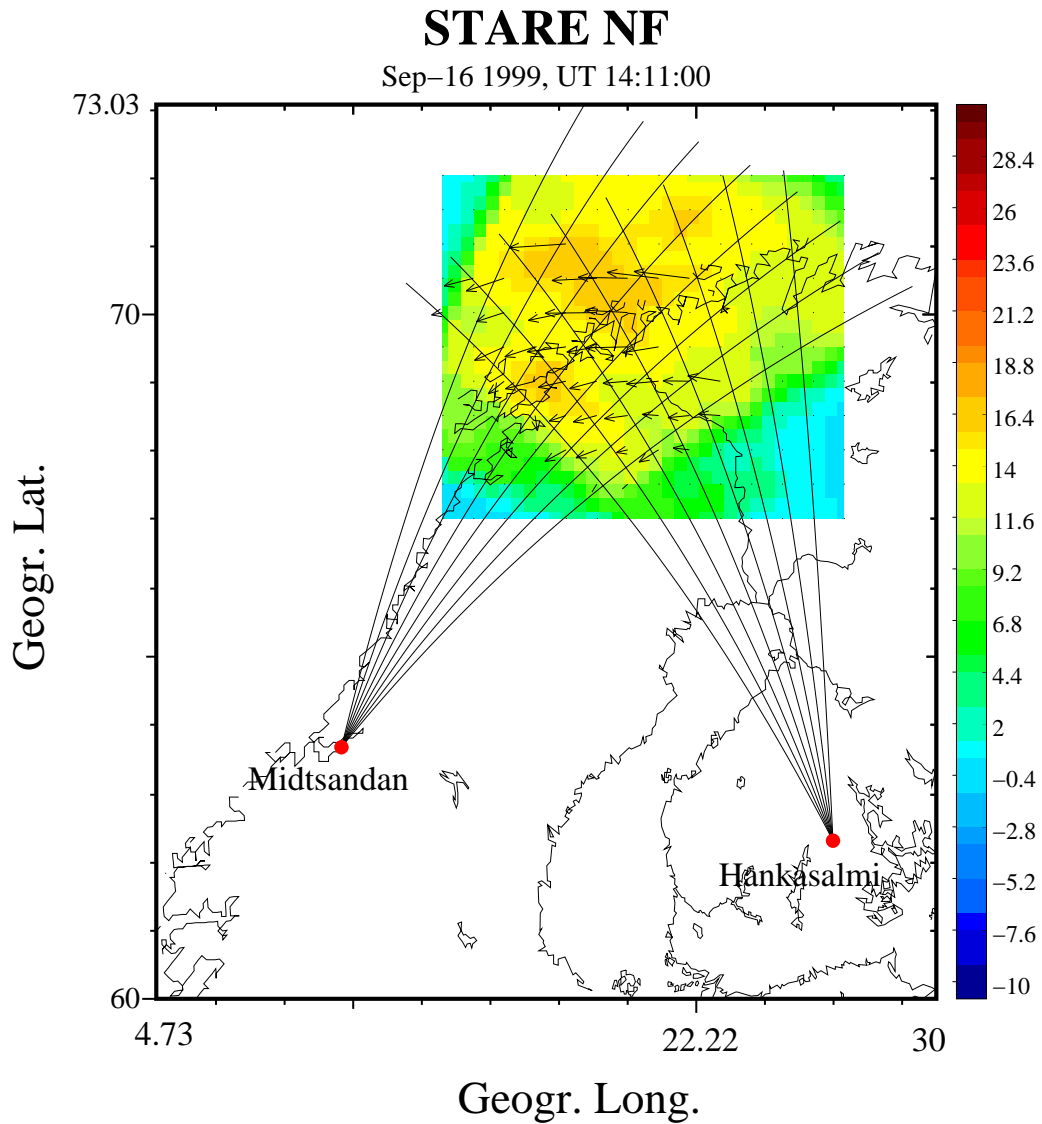


Figure 3.7: Two-dimensional map of echo intensities and flow velocity vectors measured by the STARE system at 1149 UT on September 16, 1999 is shown. The echo intensities are measured in dB units with respect to the background noise level. The flow vectors are derived from two velocity components measured at Midstandan and Hankasalmi applying the cosine rule.

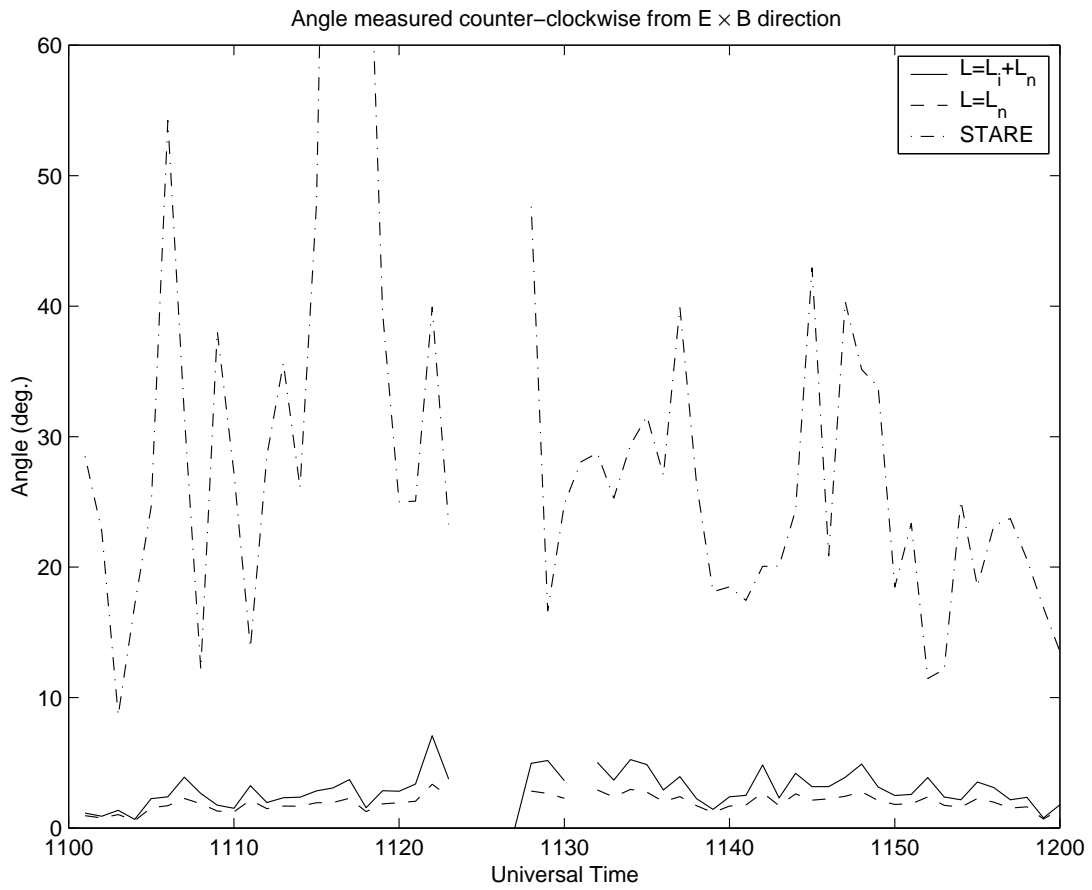


Figure 3.8: Similar to Fig. 3.6. Angles of flow derived from STARE data by applying the cosine rule are also plotted (dash-dotted line).

105 km altitude. If the camera could detect such meter-scale irregularities, however, wave propagation directions could be determined from its two dimensional images. Simultaneous observation by the camera and the EISCAT radars could be a good combination of testing our estimation of electron flow directions.

Another implication of our results is the effects of the electron drift parallel to $-\mathbf{E}$ on the magnetosphere-ionosphere coupling by modifying the ionospheric current system. The dissipative component of height-integrated Ohm's law for the ionosphere, $\mathbf{J}_P = \Sigma_P \mathbf{E}_\perp$, is slightly non-linear. Fig. 3.9 shows semi-empirically the relationship between the height-integrated Pedersen current, Σ_P , and $|\mathbf{E}|$ for a representative profile of n_e . To obtain the plot, observations of T_e at different altitudes were plotted over $|\mathbf{E}|$. Straight lines were then fitted to the increase of T_e (see also Schlegel and St.-Maurice, 1981; Jones *et al.*, 1991) Using (3.7) \mathbf{j}_e was calculated for a range of electric fields. Height integration gives the total current $J_{P,total} = J_{P,e} + J_{P,i}$, $J_{P,(e,i)} = \int j_{P,(e,i)} dh$, which is plotted in Fig. 3.9. We can see that at the onset of the MTSI at about 20 mVm^{-1} , the current-voltage relation has a small non-linear kink.

That Σ_P depends (weakly) on $|\mathbf{E}|$ could potentially destabilize MI coupling. When $|\mathbf{E}| > E_{th}$, the E region draws more than the proportional current from the magnetosphere. This ionospheric non-linearity potentially generates higher harmonics in geomagnetic pulsations, and in Alfvén waves. However, as already expressed, the deviation from the linear Ohm's law is rather small.

Finally, macroscopic consideration of the effects of the electrojet irregularities on the flow of the current through the ionospheric plasma could be done in the same way as Hagfors (1984). Although we have not estimated the effect in detail, the effect of the irregularities on the mean current flow does seem to lead to a deviation in the direction of the current flow. The detailed assessment requires numerical calculations with knowledge of the power spectrum of the density irregularities and is left for our future study.

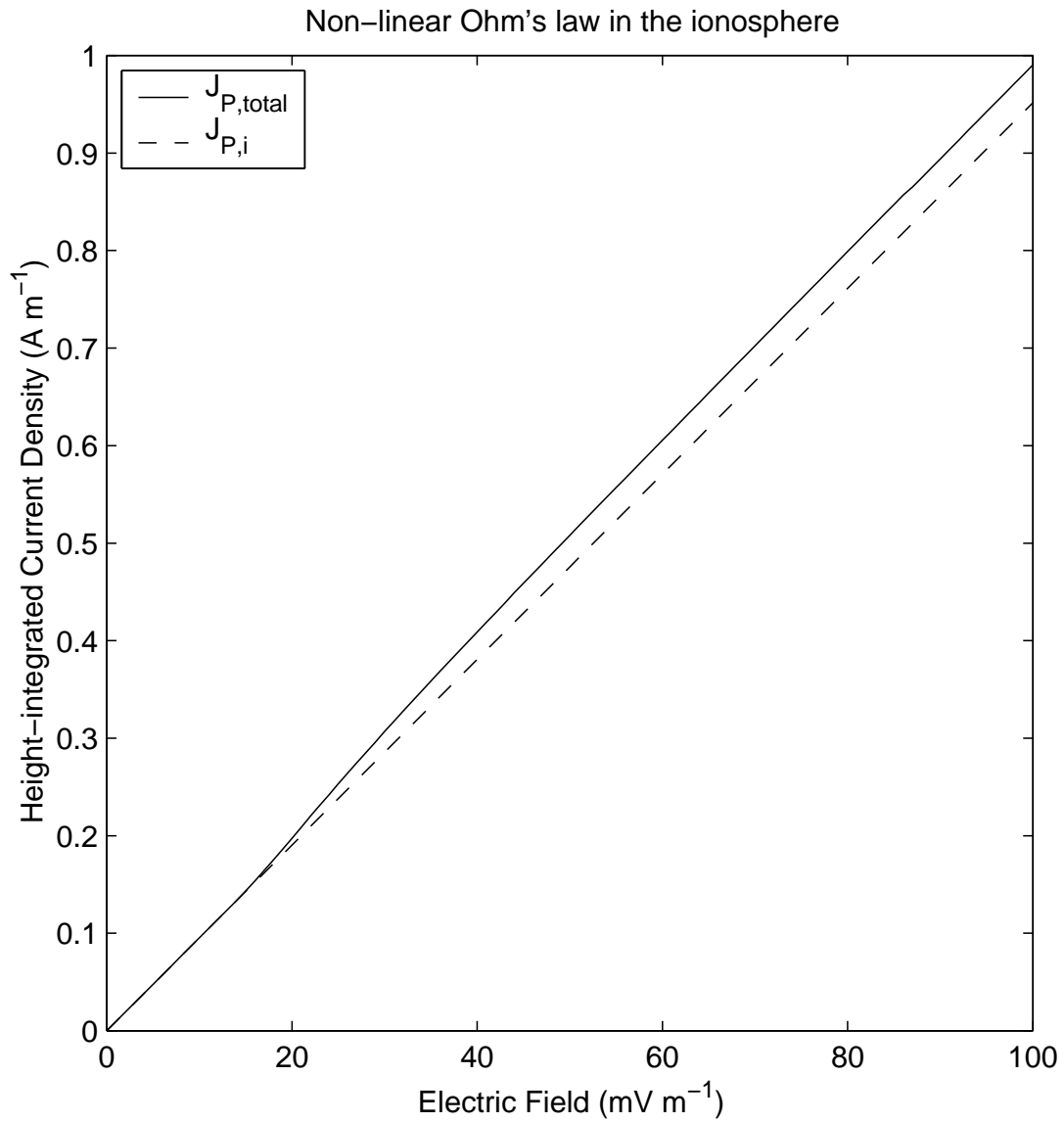


Figure 3.9: Semi-empirically obtained relation between height-integrated current and cross field voltage for a specific electron density profile. A straight line (linear Ohm's law, dashed line) would result without anomalous heating. However, above the threshold for the MTSI, the total height-integrated current $J_{P,total} = J_{P,e} + J_{P,i}$ (solid line) is higher.

3.3 Cosmic Noise Absorption: Comparison with observation by IRIS

3.3.1 Introduction

In Sec. 3.2, we have introduced the anomalous electron collision frequency ν_e^* which macroscopically parameterizes all the microscopic effects. It is an effective collision frequency based on the analogy of the classical collision frequency to represent the amount of an electron Pedersen drift (energy dissipation), or deflection angles of electron drift velocity from a $\mathbf{E} \times \mathbf{B}$ direction. To know the nature of ν_e^* , it is important to examine whether the ν_e^* can act in the same way as the classical collisions in other phenomena where collisions of electrons play an important role.

Cosmic Noise Absorption (CNA) is an effect of the ionosphere that absorbs a fraction of radio waves from extraterrestrial sources. As mentioned in Sec. 2.3, it is measured in riometers. In CNA, collisions of electrons are essential to dissipate a fraction of energy of incident extraterrestrial radio waves. The absorption rate K in dB/km when radio waves pass through the plasma is given by Hunsucker (1991)

$$K \simeq 4.6 \cdot 10^{-2} \left(\frac{n_e \nu_e}{\omega^2 + \nu_e^2} \right) \quad (\text{db/km}) \quad (3.13)$$

for wave propagation perpendicular to \mathbf{B} or for unmagnetized plasma, and

$$K \simeq 4.6 \cdot 10^{-2} \left(\frac{n_e \nu_e}{(\omega \pm \Omega_e)^2 + \nu_e^2} \right) \quad (\text{db/km}) \quad (3.14)$$

for propagation parallel to \mathbf{B} . For extraordinary waves, the minus sign and the plus sign for ordinary waves must be used. For riometer frequencies of $\sim 40 \text{ MHz} \gg \nu_e$, K is proportional to ν_e as well as n_e . The balance between decreasing n_e and increasing ν_e with a decreasing altitude causes a peak of K in the D region. The absorption measured by riometers is given by an integral along the line of sight, [Eq.] If the ν_e^* acts as a real collision frequency, we expect enhancement of absorption associated with ν_e^* in the E region.

Using an IS radar and a riometer at Sondre Strømfjord, Greenland, however, Stauning (1984) and Stauning and Olesen (1989) have shown that the absorptions observed by the riometer can be explained by the absorption model (Eq. (3.14)) with the classical effective electron-neutral collision frequency which can be slightly enhanced by elevated T_e , and that adopting anomalous collision frequencies given by Robinson (1986) lead to significant overestimation, for example, 15.9 dB when 0.5 dB is observed. A macroscopic theory which is not concerned with the microphysics of the waves also predicts that the anomalous absorption associated with the presence of the turbulences is negligible. (See Appendix A) In this section, we do a similar analysis as Stauning (1984) and Stauning and Olesen (1989) with higher time resolution data in good quality from the EISCAT Tromsø UHF radar and the Kilpisjärvi IRIS.

3.3.2 Observation

Fig. 3.10 shows the summary of data obtained by the Kilpisjärvi IRIS and the EISCAT UHF radar between 0900 and 1600 UT on September 16, 1999 when the electric fields are enhanced several times and electrons are heated. The absorption data were measured by beam No. 9 which covers the ionosphere over Tromsø (see Fig. 2.3 and Table 2.1) and corrected to values which would be observed if the line of sight is vertical by taking into account the obliqueness of the line of sight. Between 0900 and 1030 UT, prominent absorptions are found. After 1030 UT, the absorptions are generally weak. Occasionally some negative absorptions, which indicates an *increase* of radio wave power, are observed around 1130, 1200, 1300, 1420, and 1530 UT. They are due to solar radio emission and not relevant for this study. The EISCAT UHF radar operated in the CP-1-K mode where the Tromsø radar was pointed along the geomagnetic field line and the remote sites (Kiruna and Sodankylä) looked continuously at a common volume in the F region for the determination of \mathbf{E} . Above 90 km, we have used the data obtained by using the alternating-code which enables us to derive parameters like n_e and T_e . Below 90 km where it can be rather safely assumed that $T_e = T_n$, data are obtained by power-profile which

provides n_e down to 62 km with an assumption that $T_e = T_i$ which can be safely justified in this altitude range. At 108 km where electron heating is generally strongest, several T_e enhancements up to about 1200 K are seen at around 1127, 1133, 1206, 1220, 1419, and 1448 UT associated with strong electric fields. In general, the trend of n_e at 90 km and the absorption are correlated well, and T_e enhancements (or strong $|\mathbf{E}|$) seem to have poor correlation.

3.3.3 Discussion

To check whether the electron anomalous collision frequency ν_e^* is effective in CNA, we have estimated the ionospheric absorptions with EISCAT data based on two different assumptions:

1. $\nu_e = \nu_{en} + \nu_e^*$
2. $\nu_e = \nu_{en}$

and compared them with the absorption measured by the IRIS. If the absorption estimated by the anomalous collision frequency (case 2) was the same order as the observed absorption, the possibility for the anomalous collision frequency to act as the 'real' collision frequency is not excluded, although it is still uncertain. However, if the estimated absorption with the anomalous collision frequency is much larger than the observations, and if the classical collision frequency without the anomalous one (case 1) instead accounts for the observation, it is clear that the anomalous collision frequency is not completely equivalent to the classical collision frequency. We have argued this approach for two reasons. First, in fact, it has been shown by Stauning and Olesen (1989) that the calculation of absorption with the anomalous collision frequency introduced by Robinson (1986) with the quasi-linear theory overestimates the absorption. Therefore, we had expected that our anomalous collision frequency would not be effective on the radio wave absorption. Second, it is difficult to estimate the collision frequency profile required for the observed absorption, since the observed absorption is integrated along the line of sight. To solve

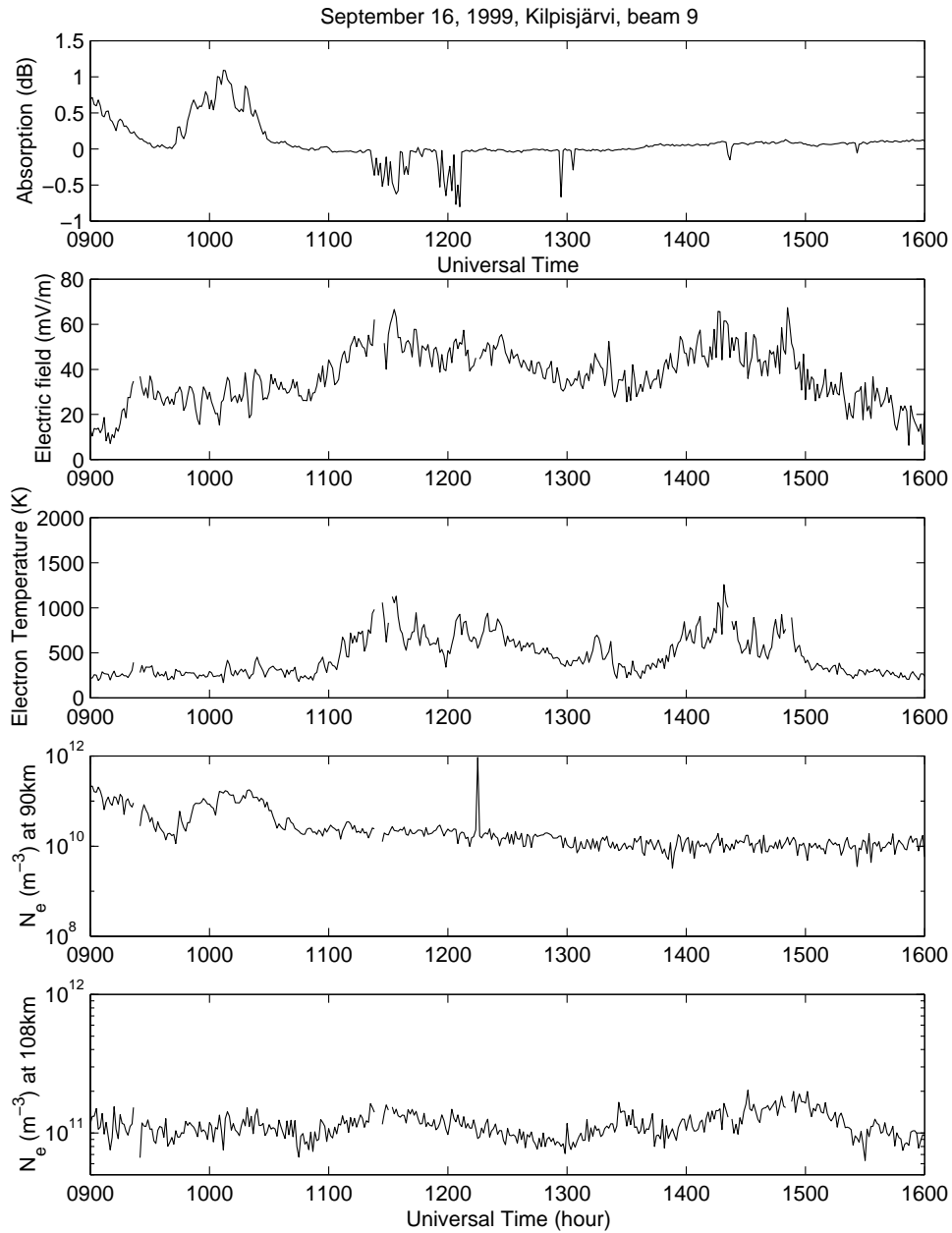


Figure 3.10: Overview of a data set with long periods of elevated T_e in the lower E region with a time resolution of 1 min. The top panel shows the absorption measured by beam 9 of the Kilpisjärvi IRIS. The last four panels show observation by the EISCAT, $|\mathbf{E}|$ (the second panel), T_e at 108 km (third), n_e at 108 km (fourth), and n_e at 90 km (fifth).

the equation of absorption for the collision frequency, a certain collision frequency model must be assumed. In the case of 2, T_e contributes to absorption only through the weak dependence of ν_{en} on T_e , because ν_{en} is approximately proportional to $T_e^{1/2}$ in the E region where the absorption is weak. On the other hand, for the case 1, T_e contributes to absorption through both ν_{en} and ν_e^* . In estimating absorption, we have neglected the effect of the geomagnetic field even if the IRIS beam 9 measures radio waves propagating obliquely to the geomagnetic field line. This is justified because $\omega \gg \Omega_e$. This assumption allows us to use Eq. (3.13) in our estimation. Then we have integrated K over an altitude from 80 to 120 km.

$$A = \int K dh = 4.6 \cdot 10^{-2} \int_{80 \text{ km}}^{120 \text{ km}} \frac{n_e \nu_e}{\omega^2 + \nu_e^2} dh \quad (\text{dB}) \quad (3.15)$$

Fig. 3.11 shows the results of the comparison between 1400 and 1500 UT. It is clear that the estimated absorption with $\nu_e = \nu_{en} + \nu_e^*$ is too high while the estimation with $\nu_e = \nu_{en}$ shows very good agreement with the observation by IRIS. To check the accuracy of our calculation, we have also done the same analysis for a period when the absorption observed by IRIS is strong (Fig. 3.12). In this figure, red circles ($\nu_e = \nu_{en} + \nu_e^*$) are almost hidden by green ones ($\nu_e = \nu_{en}$) because mostly $\nu_e^* = 0$ due to weak $|\mathbf{E}|$. The estimated absorption with $\nu_e = \nu_{en}$ is in excellent agreement with absorption measured by the IRIS.

Our results confirm the analysis by Stauning (1984) and Stauning and Olesen (1989), although our ν_e^* is introduced differently from the anomalous electron collision frequency in Robinson (1986). Also our results agree well with the macroscopic consideration given in Appendix A. Therefore, our analysis strongly suggests that ν_e^* introduced to parameterize the effect of the Farley-Buneman waves in heating electrons is not effective in the absorption of radio waves. The anomalous collision can represent the electron heating rate, but it has nothing to do with CNA phenomena, and it is not necessarily equivalent to the classical collision frequency, but it rather has a limited range of application, although it can represent the drag effect of the waves equivalent to collisions of ν_e^* times per second.

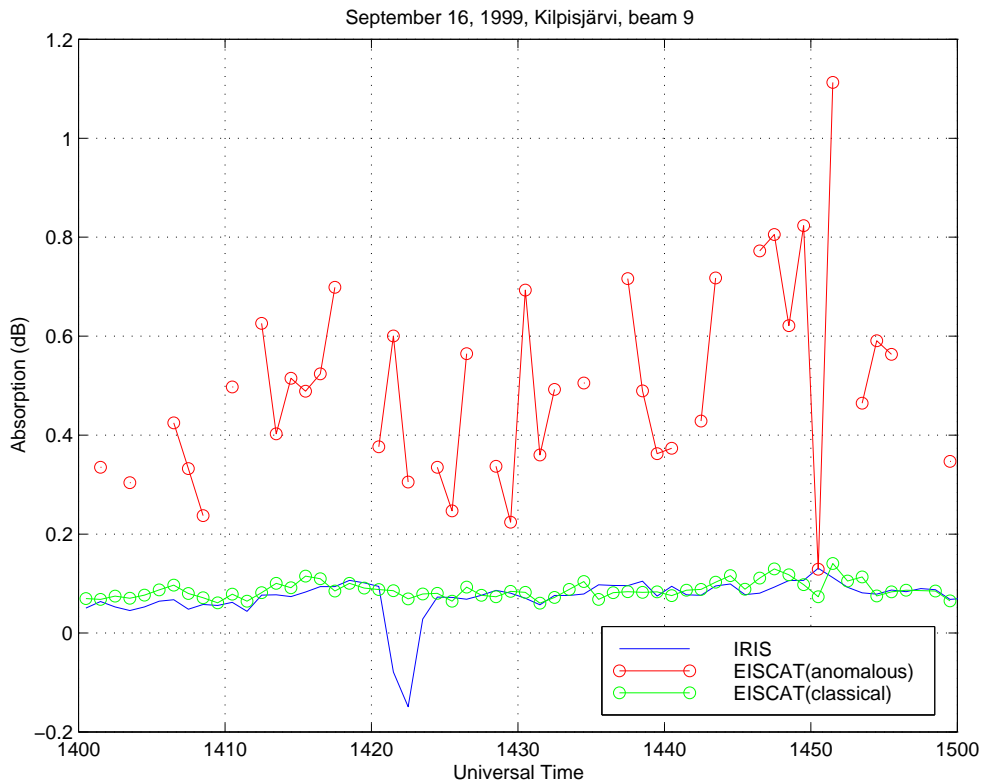


Figure 3.11: Absorptions estimated by the EISCAT data (red: $\nu_e = \nu_{en} + \nu_e^*$, green: $\nu_e = \nu_{en}$) and the IRIS measurements (blue line) are compared between 1400 and 1500 UT when $|\mathbf{E}|$ is generally strong.

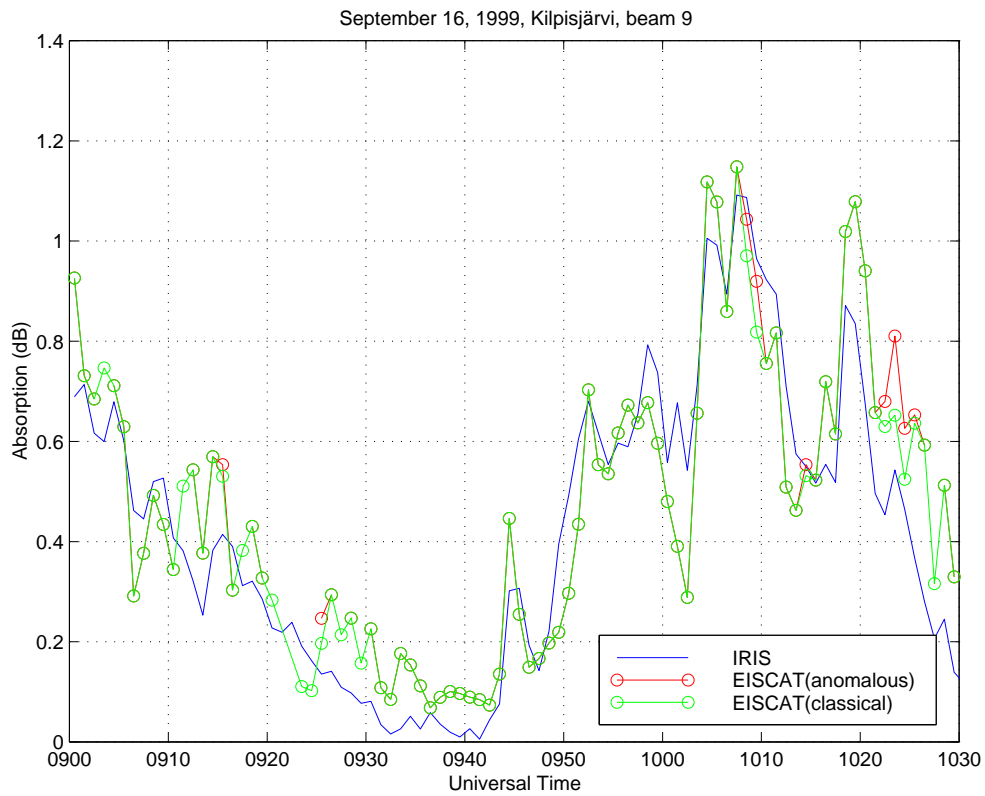


Figure 3.12: The same as Fig. 3.11. But the results are for the period when T_e is not enhanced, but n_e at 90 km is enhanced.

3.4 Summary

We have studied electron heating by Farley-Buneman waves in the lower E region using data obtained by the EISCAT radar system, the STARE system, and the Killpisjärvi IRIS. The results obtained in this study are as follows.

The electron temperatures observed in the E region are clearly isotropic over aspect angles from 0° to about 40° even when they are strongly enhanced. If the actual heating process is through electron-neutral collisions which have no directional preferences, it is natural to expect isotropic T_e . The very high heating rates suggest that Farley-Buneman waves have an electric field component both perpendicular and parallel to \mathbf{B} as proposed by St.-Maurice (1987). If T_e enhancement is instead due to a direct scattering of electrons by wave fields not involving electron-neutral collisions, our observation implies that these waves should be isotropic.

Because the total energy is conserved, electrons must carry a dissipative current which means that the electron drift velocity should deviate from the $\mathbf{E} \times \mathbf{B}$ direction to the $-\mathbf{E}$ direction. We have found an angle between \mathbf{u}_e and $\mathbf{E} \times \mathbf{B}$ of about 7° ($\nu_e^* \sim 30\nu_{en}$) during events with high $|\mathbf{E}|$. This flow angle rotation could not be confirmed by observations by the STARE system probably due to the effect of the ion velocity and the saturation of the irregularity phase velocity at C_s . We have examined the importance of the electron Pedersen currents and have found that at altitudes $\lesssim 110$ km this current can become the main Pedersen current. Consequently, the current-voltage relation in the Earth's ionosphere is slightly non-linear.

We have shown that the cosmic noise absorption observed by the Killpisjärvi IRIS can be well explained by the model in which only the classical electron-neutral collision frequency is taken into account, even when the anomalous electron collision frequencies greatly exceed the classical ones associated with strong electric fields and strong electron temperature enhancements. From this result, we concluded that ν_e^* has nothing to do with the absorption of radio waves in the ionosphere. Therefore, ν_e^* introduced to parameterize the heating effect of the Farley-Buneman waves has a rather limited range of application.

We conclude that the waves should have the drag effect equivalent to the collisions of ν_e^* times per second on the electrons drift, but ν_e^* is not necessarily equivalent to the classical collision frequency in the other phenomena.

Chapter 4

F region

In this chapter, we move to the F region. Incoherent scattering which is an interaction between radio waves and electrostatic (the ion acoustic and the Langmuir) waves are dealt with. We calculate IS spectra for plasmas with electrons with the kappa distribution function, and their differences from Maxwellian IS spectrum are shown. Possible misinterpretation of the ionospheric parameters are estimated. Finally we discuss the plasma line with electrons with the kappa distribution function, and point out the possibility to measure deviation of an electron distribution function from a Maxwellian one. This chapter is mostly a reproduction of Saito *et al.* (2000).

4.1 Introduction

Incoherent scattering is a very powerful tool to investigate plasma in the Earth's upper atmosphere and in the laboratory. Using incoherent scatter (IS) spectra, one can derive various parameters such as n_e , T_i , T_e , u_i . Incoherent scattering allows us to see directly properties of the two basic types of electrostatic waves in a plasma, the ion acoustic waves and the Langmuir waves, and these wave properties can tell us not only the plasma parameters such as n_e , T_i , T_e , and u_i but also something about the plasma itself like the particle distribution functions. It is well known that the velocity distribution functions of ions and electrons in a plasma are Maxwellian, if the ions and the electrons are in thermal

equilibrium. Often, however, external energy input causes significant deviations of the distribution functions from a Maxwellian. For example, in the Earth's ionosphere a high electric field in combination with ion-neutral interaction leads to a bi-Maxwellian or even a toroidal distribution function of the ions (St.-Maurice and Schunk, 1979). The corresponding incoherent scatter (IS) ion line was explored in detail (Raman *et al.*, 1981). Zheng *et al.* (1997) have calculated the spectrum of another type of non-Maxwellian electron distribution function, the super-Gaussian distribution ($f(v) \propto \exp(-(v/v_{th})^x), x > 2$). In this work we investigate the effects of a kappa distribution function of electrons on the IS spectrum.

Theoretically it has been shown that the velocity distribution function obeys a power-law at energies higher than critical energy when a superthermal radiation field is present (Hasegawa *et al.*, 1985). Such a power-law functional dependence is an approximation to the more general distribution, the generalized Lorentzian or kappa distribution (Baumjohann and Treumann, 1996). Measurements of electron energy spectra with space craft have been successfully modeled with kappa distributions (Vasyliunas, 1968; Christon *et al.*, 1988; Bryant, 1999). Also plasma turbulence can interact with both thermal and suprathermal particles and generate suprathermal tails of the particle velocity distribution (Galeev, 1989). For plasmas in which both electrons and ions have kappa distribution, Summers and Thorne (1991) have calculated the modified plasma dispersion function theoretically, and found general properties of the ion acoustic waves and the Langmuir waves (See also Summers *et al.*, 1996). Since incoherent scatter spectra are closely related to those waves, some qualitative expectation of the spectra can be obtained, although it is actually assumed that only electrons have kappa distribution while ion distribution function remains Maxwellian.

An IS spectrum consists of two characteristic features, the ion line and the plasma line. The ion line is an echo that corresponds to the ion acoustic waves found in the low frequency range (for a transmitter frequency of several hundred MHz, in the range of a few kHz). Since the ion line contains information about ions as well as electrons, it is the ion line that is used to derive the ionospheric parameters. Therefore, it is important to know

the effects of the kappa distribution function on the ion line for the correct derivation of the parameters. This knowledge would be very important, for example, for estimating the momentum balance of the ionosphere or the threshold of plasma instabilities. The other characteristic feature is that plasma lines are received in the high frequency range. This feature corresponds to the Langmuir waves found around $(\omega_{pe}/2\pi)(1 + 3k^2\lambda_D^2)^{\frac{1}{2}}$, where λ_D is the electron Debye length. Usually the lines appear at several MHz up- and downshifted from the transmitter frequency depending on electron density and temperature. Since ions are too heavy to oscillate at the high frequency range, the contribution of ions to the Langmuir waves is negligible. The shape and position of the plasma lines are determined by electrons (and also by the radar k-vector). Therefore, it is expected that a kappa distribution of electrons has clearer effects on the plasma line than on the ion line. This may be useful in obtaining a correct analysis of the ion line by providing more information about electrons.

In the Earth's topside ionosphere the European Incoherent Scatter (EISCAT) radars observe frequently considerably enhanced electron temperatures. Unlike the electron heating in the E region, it is caused by soft precipitation. Candidates for the heating mechanisms are direct collisions and indirectly via the Langmuir waves and turbulence generated for example by a bump-in-tail instability. Both of these mechanisms could in principle enhance velocity-space diffusion and distorts the electron distribution function and cause a high-energy tail in the electron distribution function. Therefore, one cannot exclude the possibility that the electron distribution develops a high energy tail. It is known that the electron heating by particle precipitation is also associated with ion upflow and downflow (Wahlund *et al.*, 1992; Ogawa *et al.*, 2000). This field-aligned ion flow could be explained by ambipolar diffusion. The data analysis is usually carried out under the assumption of Maxwellian distribution functions. In order to get more reliable, quantitative understanding from incoherent scatter data, we need to consider the possibility that the electrons have a high energy tail which might influence the fits of ionospheric parameters in the data analysis. In this work, we try to model the electron distribution function with a kappa distribution. We calculate the IS ion and plasma lines for a plasma with

electron kappa distributions. The effects and possible misinterpretations of a Maxwellian analysis are investigated. In Sec. 4.2 the theoretical basis for calculating the IS spectra is presented. In Sec. 4.3.1 the ion line is discussed, and the errors caused by a Maxwellian analysis are examined in Sec. 4.3.2. Sec. 4.3.3 investigates the plasma lines resulting from an electron kappa distribution.

4.2 Theory

The procedure of the theoretical calculation of an IS spectrum is described by Sheffield (1975). We follow Sheffield (1975) for the following derivation. Scattered power in the frequency range $d\omega$ and in the solid angle $d\Omega$ with wave vector \mathbf{k} is given by

$$P_s d\Omega d\omega \propto n_{e0} S(\mathbf{k}, \omega) \quad (4.1)$$

where n_{e0} is the electron density. $S(\mathbf{k}, \omega)$ is the *spectral density function* given by

$$S(\mathbf{k}, \omega) = \lim_{\gamma \rightarrow 0} \frac{2\gamma}{V} \left\langle \frac{|n_e(\mathbf{k}, \omega - i\gamma)|^2}{n_{e0}} \right\rangle \quad (4.2)$$

where $n_e(\mathbf{k}, \omega - i\gamma)$ is the Fourier- in space and Laplace- in time transform of the electron density $n_e(\mathbf{r}, t)$,

$$\begin{aligned} n_e(\mathbf{k}, \omega - i\gamma) &= \int_{-\infty}^{+\infty} e^{i\mathbf{k}\cdot\mathbf{r}} d\mathbf{r} \int_{-\infty}^{+\infty} n_e(\mathbf{r}, t) e^{-i(\omega - i\gamma)t} dt \quad (\gamma > 0) \end{aligned} \quad (4.3)$$

When no magnetic field exists, or \mathbf{k} is parallel to the magnetic field, the spectral density function is given by

$$S(\mathbf{k}, \omega) = 2 \left| \frac{(1 + C_i)}{\epsilon} \right|^2 B_e + 2Z \left| \frac{C_e}{\epsilon} \right|^2 B_i \quad (4.4)$$

where Z is the charge number of ions. Functions $C_{e,i}$, $B_{e,i}$, and ϵ in Eq. (4.4) are defined taking into account the effect of collisions through a BGK model as follows:

$$C_j = \frac{1}{1 + D_j} \int_{-\infty}^{+\infty} d\mathbf{v} \frac{q_j^2 n_{j0}}{m_j \epsilon_0 k^2} \frac{\mathbf{k} \cdot \partial f_{j0}(\mathbf{v}) / \partial \mathbf{v}}{\omega - \mathbf{k} \cdot \mathbf{v} - i\nu_j} \quad (4.5)$$

$$\begin{aligned} B_j &= \frac{\nu_j}{|1 + D_j|^2} \int_{-\infty}^{+\infty} d\mathbf{v} \frac{f_{j0}(\mathbf{v})}{(\omega - \mathbf{k} \cdot \mathbf{v})^2 + \nu_j^2} \\ &\quad - \frac{|D_j|^2}{\nu_j |1 + D_j|^2} \end{aligned} \quad (4.6)$$

where

$$D_j = i\nu_j \int_{-\infty}^{+\infty} d\mathbf{v} \frac{f_{j0}(\mathbf{v})}{\omega - \mathbf{k} \cdot \mathbf{v} - i\nu_j} \quad (4.7)$$

ν_j is the collision frequency, $f_{j0}(\mathbf{v})$ the distribution function, m_j the mass, q_j the electric charge, n_{j0} the density, ϵ_0 the electric permittivity of the vacuum, and ω the angular frequency. Here j can be e or i to denote electrons or ions, respectively. $\epsilon(\mathbf{k}, \omega, \nu_e, \nu_i)$ is the plasma dielectric function,

$$\epsilon(\mathbf{k}, \omega, \nu_e, \nu_i) = 1 + C_i + C_e \quad (4.8)$$

In integrating Eqs. (4.5) and (4.6), the integrals of a form need to be calculated.

$$\int_{-\infty}^{+\infty} d\mathbf{v} \frac{f_{j0}(\mathbf{v})}{\omega - \mathbf{k} \cdot \mathbf{v} - i\nu_j} \quad (4.9)$$

The integrand has a pole at $\mathbf{k} \cdot \mathbf{v} = \omega - i\nu_j$. The integration path must be above the pole because we have defined the Laplace transform with negative imaginary part of frequency and taken the limit of $\gamma \rightarrow 0$ even in the case of a collisionless plasma.

Eqs (4.4)–(4.8) are valid for arbitrary distribution functions as long as a plasma is stable. It is well known that the particle distribution function becomes Maxwellian when the particles are in thermal equilibrium. Therefore, in usual incoherent scatter analysis one can assume that f_{j0} is Maxwellian,

$$f_M(v) = \frac{1}{(\sqrt{\pi}v_{th,M})^3} \exp\left(-\frac{v^2}{v_{th,M}^2}\right) \quad (4.10)$$

where $v_{th,M}$ is the characteristic velocity (or thermal velocity) of the Maxwellian distribution function given by

$$v_{th,M} = \sqrt{\frac{2k_B T}{m}} \quad (4.11)$$

Later, the temperature of different distribution functions is discussed. Therefore, the temperature must be clearly defined in a consistent way for any distribution functions. Eq. (4.11) has been derived according to the definition of temperature, Eq. (1.2). However, as mentioned in Sec. 4.1, distribution functions with high energy tail have been often observed in space plasmas when energy input maintaining the high energy tail exists. It is

known that such distribution functions can be well modeled by a generalized Lorentzian function with spectral index κ (kappa distribution). The one-dimensional kappa distribution function is given by

$$f_{\kappa}^{(1)}(v) = \frac{1}{\sqrt{\pi}v_{th,\kappa}} \frac{\Gamma(\kappa + 1)}{\kappa^{3/2}\Gamma(\kappa - 1/2)} \left(1 + \frac{v^2}{\kappa v_{th,\kappa}^2}\right)^{-\kappa} \quad (4.12)$$

where $v_{th,\kappa}$ is also the characteristic velocity (or thermal velocity) of the kappa distribution function given by

$$v_{th,\kappa} = \sqrt{\frac{2\kappa - 3}{\kappa} \frac{k_B T}{m}} \quad (4.13)$$

which satisfies the relation (1.2) when $\kappa > \frac{3}{2}$. (Summers and Thorne, 1991) Kappa distribution functions for different values of κ are compared with Maxwellian in Fig. 4.1. It should be noted that the smaller the index κ is, the more high energy electrons exist. In the limit of $\kappa \rightarrow \infty$, the kappa distribution converges to Maxwellian.

To evaluate the spectral density function, it is assumed that the ion distribution function is Maxwellian because it is unlikely to be influenced severely by plasma waves or turbulence. Following Sheffield (1975), Eqs. (4.5)–(4.7) for ions become as follows:

$$C_i = \frac{1}{1 + D_i} \frac{1}{Z} \frac{2\omega_{pi}^2}{k^2 v_{th,M}^2} [1 + \xi_M Z_-(\xi_M)] \quad (4.14)$$

$$D_i = -\frac{i\nu_i}{k v_{th,M}} Z_-(\xi_M) \quad (4.15)$$

$$B_i = -\frac{1}{k v_{th,M} |1 + D_i|^2} \text{Im}[Z_-(\xi_M)] - \frac{|D_i|^2}{\nu_i |1 + D_i|^2} \quad (4.16)$$

where

$$Z_-(\xi_M) = \frac{1}{\sqrt{\pi}} \int_{-\infty}^{+\infty} \frac{e^{-s^2}}{s - \xi_M} ds \quad (4.17)$$

$$= i\sqrt{\pi} \exp(-\xi_M^2) (\text{erf}(i\xi_M) - 1) \quad (4.18)$$

and

$$\xi_M = \frac{\omega - i\nu_i}{k v_{th,M}} \quad (4.19)$$

‘erf’ is the complex error function. Here the ion plasma frequency defined is introduced by

$$\omega_{pi} = \left(\frac{n_{i0} Z^2 e^2}{m_i \epsilon_0} \right)^{\frac{1}{2}} \quad (4.20)$$

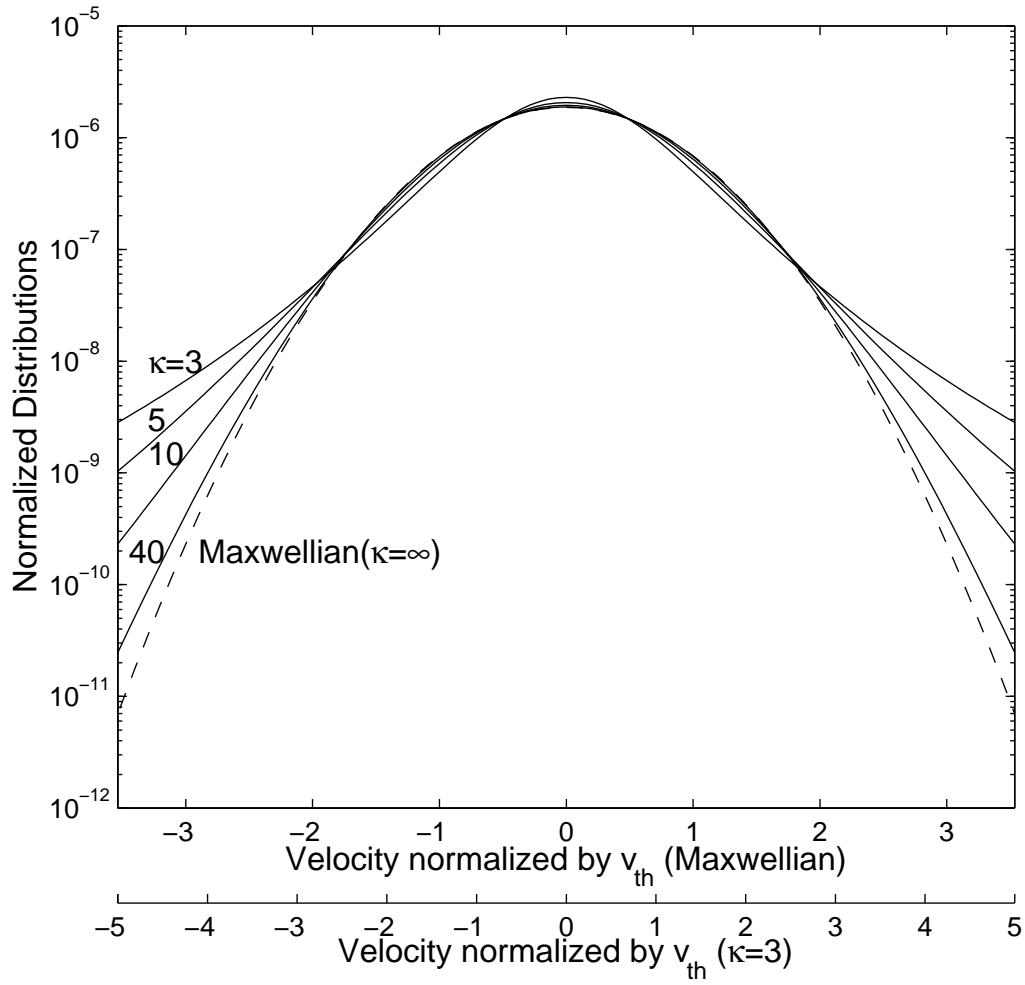


Figure 4.1: A comparison between Maxwellian and kappa distribution with $\kappa = 3, 5, 10,$ and 40 . Maxwellian distribution (*dashed line*) corresponds to $\kappa = \infty$. *x-axes* are indicated by velocities normalized by $v_{th,M}$ and $v_{th,\kappa=3}$

The function $Z_-(\xi_M)$ given by Eq. (4.17) is very similar to the plasma dispersion function (Fried and Conte, 1961) except for the sign of the second term of the right hand side. When the electron distribution function along the line-of-sight is a generalized Lorentzian distribution (kappa distribution), i.e. $\int_{-\infty}^{+\infty} d\mathbf{v}_\perp f(\mathbf{v}) = f_\kappa^{(1)}(v_\parallel)$, where \mathbf{v}_\perp and v_\parallel are the velocities perpendicular to and parallel to the line-of-sight, respectively, we can write

$$C_e = \frac{1}{1 + D_e} \frac{2\omega_{pe}^2}{k^2 v_{th,\kappa}^2} \left[1 - \frac{1}{2\kappa} + \xi_\kappa Z_{\kappa,-}^*(\xi_\kappa) \right] \quad (4.21)$$

$$D_e = -\frac{i\nu_e}{kv_{th,\kappa}} \left(\frac{\kappa}{\kappa - 3/2} \right) \left(\frac{\kappa - 1}{\kappa} \right)^{3/2} \\ \times Z_{\kappa-1,-}^* \left(\sqrt{\frac{\kappa-1}{\kappa}} \xi_\kappa \right) \quad (4.22)$$

$$B_e = -\frac{1}{kv_{th,\kappa} |1 + D_e|^2} \left(\frac{\kappa}{\kappa - 3/2} \right) \left(\frac{\kappa - 1}{\kappa} \right)^{3/2} \\ \times \text{Im} \left[Z_{\kappa-1,-}^* \left(\sqrt{\frac{\kappa-1}{\kappa}} \xi_\kappa \right) \right] - \frac{|D_e|^2}{\nu_e |1 + D_e|^2} \quad (4.23)$$

where

$$Z_{\kappa,-}^*(\xi_\kappa) = \frac{\kappa^{\kappa-1/2} \Gamma(\kappa + 1)}{\sqrt{\pi} \Gamma(\kappa - 1/2)} \int_{-\infty}^{+\infty} \frac{ds}{(s - \xi_\kappa)(s^2 + \kappa)^{\kappa+1}} \quad (4.24)$$

and

$$\xi_\kappa = \frac{\omega - i\nu_e}{kv_{th,\kappa}} \quad (4.25)$$

$Z_{\kappa,-}^*(\xi_\kappa)$ can be analytically expressed for positive integer κ as

$$Z_{\kappa,-}^*(\xi_\kappa) = -\frac{\kappa - 1/2}{2\kappa^{3/2}} \frac{\kappa!}{(2\kappa)!} \\ \times \sum_{l=0}^{\kappa} \frac{(\kappa + l)!}{l!} (-i)^{\kappa-l} \left(\frac{2}{(\xi_\kappa/\sqrt{\kappa}) - i} \right)^{\kappa+1-l}. \quad (4.26)$$

Our $Z_{\kappa,-}^*$ is the complex conjugate of the modified dispersion function Z_κ^* introduced by Summers and Thorne (1991) because we use a different complex frequency definition in the Laplace transform. The derivation of $Z_{\kappa,-}^*$ from Eq. (4.24) to Eq. (4.26) is demonstrated in Appendix. C.

4.3 Results of calculation and discussion

4.3.1 Incoherent scatter spectra with kappa distribution I: Ion lines

We have calculated IS spectra for a kappa distribution plasma for different values of κ and compared them with those from a Maxwellian plasma with the same set of parameters, n_e , T_i , and T_e . In our calculation, the following assumptions were made.

1. Electron distribution function along the magnetic field line is a kappa distribution and that in the plane perpendicular to the line-of-sight is Maxwellian, while that of the ions (in all directions) remains Maxwellian because of their heavy mass.
2. Effects of the magnetic field are not taken into account. This assumption should be justified when calculating the IS spectra from a field-aligned measurement.
3. The probing radio wave frequency is 933 MHz (wave number $k_0 = 19.55 \text{ m}^{-1}$) corresponding to the Tromsø UHF radar, one of the EISCAT radar systems. Assuming backscattering (the transmitting and receiving site are the same), this means that the wave number k becomes $39.1 \text{ m}^{-1} (= 2k_0)$.
4. Although we can take the effects of collisions into account, we set $\nu_{i,e} = 0$ for simplicity since we are interested in phenomena in the F region where the collisions are too rare to deform an IS spectrum noticeably.
5. In the case of the F region, we assume that the dominant ion is O^+ ($m_i = 16 \text{ a.m.u.}$).
6. The mean drift velocity of ions, \mathbf{v}_i , is zero.

Fig. 4.2 shows an example of our calculations of the IS spectra for various κ at the low frequency range which corresponds to the ion acoustic fluctuations (ion lines). The spectra show double-humped shapes similar to the case of Maxwellian plasma. For the same set of n_e , T_i , and T_e , the total scattered power becomes stronger, the spectral width remains

almost the same, the spectral peaks are slightly downshifted, and the depth of the valley between two spectral peaks becomes shallower. With increasing κ , the spectrum converges to a Maxwellian spectrum. Indeed, the IS spectra for a kappa distribution plasma are quite different from those for a Maxwellian plasma, although ion distribution function which mainly contributes to the ion lines is assumed to remain Maxwellian.

The increase in the total scattered power can be understood in the following way. The level of excitation of the ion line is, among other functions, a function of the local electron density for velocities around the phase velocity of the corresponding the ion acoustic waves. For the chosen set of parameters, $v_{th,M} \sim 3 \cdot 10^5 \text{msec}^{-1}$, the ion acoustic waves at frequencies around ± 10 kHz correspond to $v/v_{th,M} \sim \pm 0.0053$. Looking at Fig. 4.1, it is easy to see that in this velocity range the kappa distribution function has higher values than the Maxwellian distribution. Therefore, the excitation level of the ion line is higher.

To explain the differences of the IS spectra from the viewpoint of thermal fluctuations in a plasma more quantitatively, we have numerically solved the following dispersion equation,

$$1 + \frac{2\omega_{pe}^2}{k^2 v_{th,e}} \left[\left(1 - \frac{1}{2\kappa}\right) \frac{\omega}{k v_{th,e}} Z_{\kappa,-}^* \left(\frac{\omega}{k v_{th,e}}\right) \right] + \frac{2\omega_{pi}^2}{k^2 v_{th,i}} \left[1 - \frac{\omega}{k v_{th,i}} Z_- \left(\frac{\omega}{k v_{th,i}}\right) \right] = 0 \quad (4.27)$$

where ω is a complex frequency. For derivation of this equation, see Appendix B. For the ion acoustic waves, we have obtained the results represented in Fig. 4.3. It can be seen that the frequencies of the ion acoustic waves for $\kappa = 3$ are downshifted compared to the Maxwellian case. This corresponds to our result (Fig. 4.2) that the spectral peaks are slightly downshifted for kappa distribution. The damping rates of the ion acoustic waves for kappa distribution are stronger than those for Maxwellian. This also corresponds to the fact that the valley between the two spectral peaks becomes shallower.

If the spectra from a kappa distribution plasma are interpreted by assuming a Maxwellian plasma, the derived parameters would be quite different. So it is worth knowing quantitatively how much the differences of interpreted plasma parameters, such as n_e , T_i , and T_e , could be by using Maxwellian spectra in fitting. In the next section, we

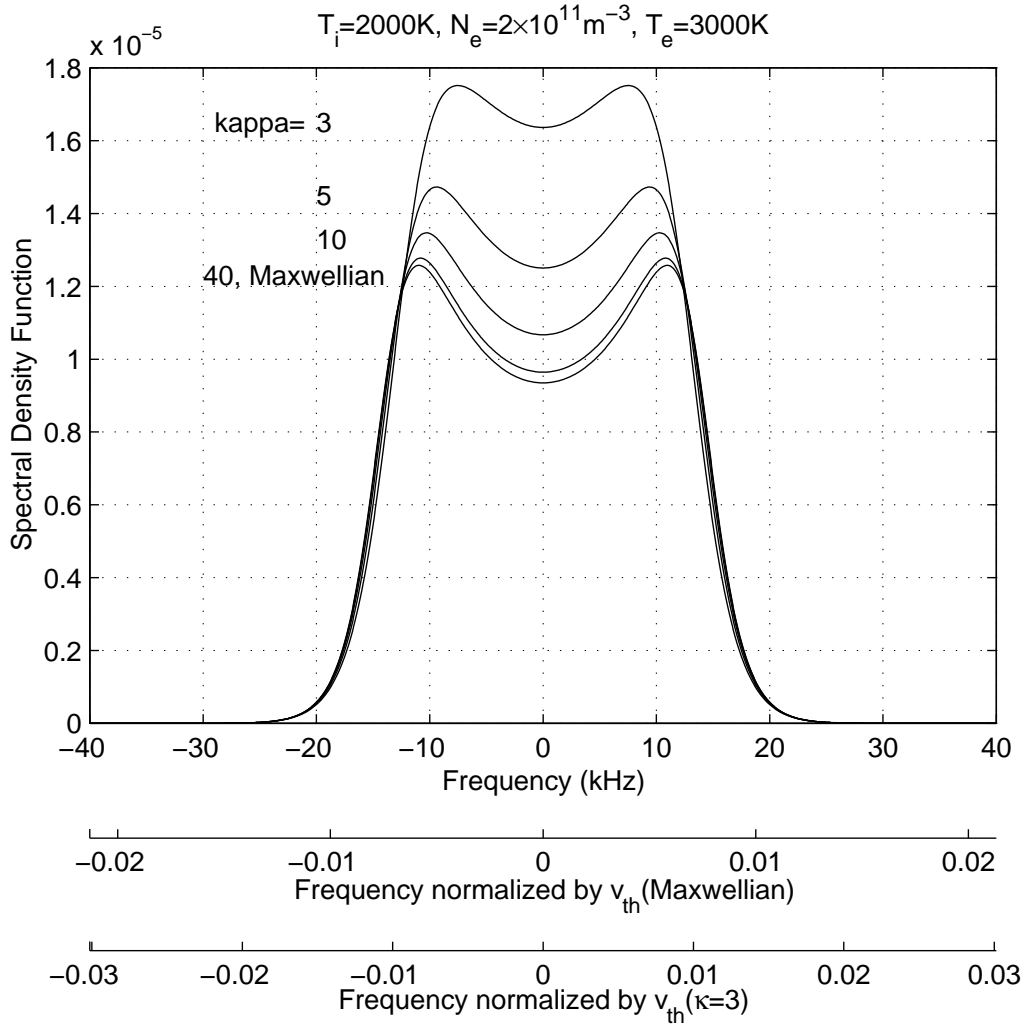


Figure 4.2: IS spectral density functions of kappa distribution plasma for a different spectral index, $\kappa = 3, 5, 10,$ and 40 , together with one from Maxwellian plasma ($\kappa = \infty$) are shown. For this case, $n_e = 2 \cdot 10^{11}\text{m}^{-3}$, $T_i = 2000\text{K}$, $T_e = 3000\text{K}$, and $m_i = 16\text{ a.m.u.}$ x -axes are indicated by corresponding velocities normalized by $v_{th,M}$ and $v_{th,\kappa=3}$ as well as by a frequency in kHz

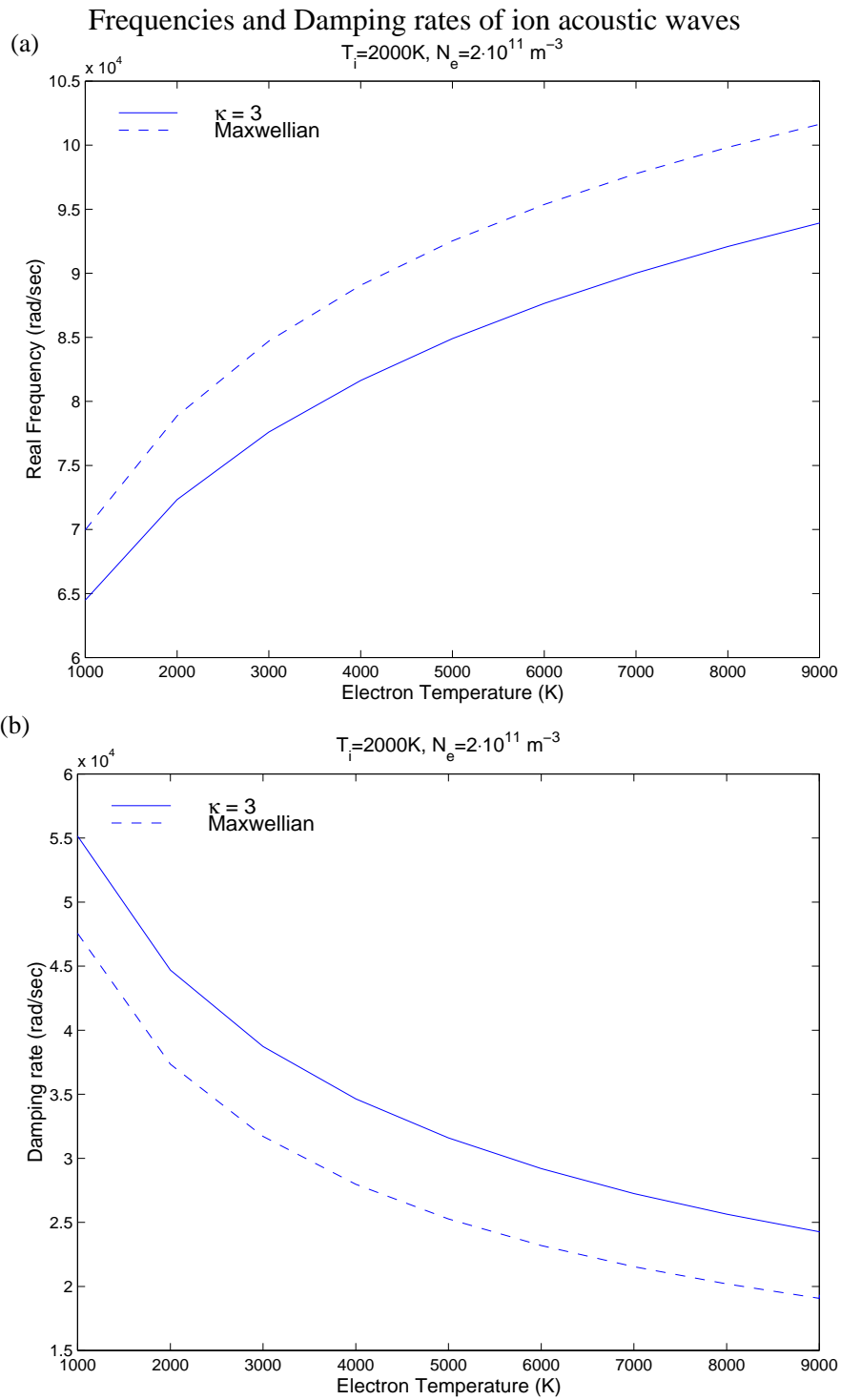


Figure 4.3: **a**, **b**. Solutions of dispersion equation for the ion acoustic waves for $\kappa = 3$ and Maxwellian. **a** Frequency **b** Damping rate are plotted over electron temperature. Ion temperature and electron density are fixed to 1000 K and $n_e = 2 \cdot 10^{11} \text{ m}^{-3}$, respectively

will estimate how large the differences could become as a result of assuming a Maxwellian distribution function if the actual distribution is a kappa distribution.

4.3.2 Difference of plasma parameters as a results of fitting with Maxwellian distribution

In our analysis, IS spectra for a kappa distribution plasma with parameters (n_e , T_i , T_e , and κ), are fitted by an IS spectra model for a Maxwellian plasma using the least square method. n_e , T_i , and T_e derived by the standard analysis are determined. Fig. 4.4 is an example of fitting a Maxwellian spectra to $n_e S(\mathbf{k}, \omega)$ calculated according to the procedure in the previous section. For this case, the ion temperature and electron density are almost the same, but the electron temperature is significantly underestimated to only 1800 K instead of 3000 K. The results for various κ with the same plasma parameters as in Fig. 4.4 are shown in Fig. 4.5. Again n_e and T_i change little, but the fitted T_e is always lower than assumed for the kappa distribution spectrum. The underestimation is up to 40% when κ is very small (more deviation from Maxwellian). The results with different sets of n_e , T_i , T_e , and κ are similar(not shown here).

It is surprising that the estimated electron density remains almost the same even though the total scattered power is larger for the spectrum with the kappa distribution. This can be understood by considering the relationship between the total scattered power and the ionospheric parameters. For the Maxwellian distribution, the total scattered power P_s is proportional to $n_e/(1 + T_e/T_i)$. Therefore, the estimated n_e is proportional to $P_s(1 + T_e/T_i)$. By lowering the estimation of T_e , the estimated n_e remains almost the same even though P_s for the kappa distribution spectrum is larger than that for the a Maxwellian for the same set of n_e , T_i , and T_e .

This underestimate of T_e may also be surprising, but this result is rather reasonable. Ion lines are sensitive to the derivative of the ion and electron distribution functions at the velocity range corresponding to the phase velocity of the ion acoustic waves. For electrons, this velocity range is the very narrow region of the center of their distribution function

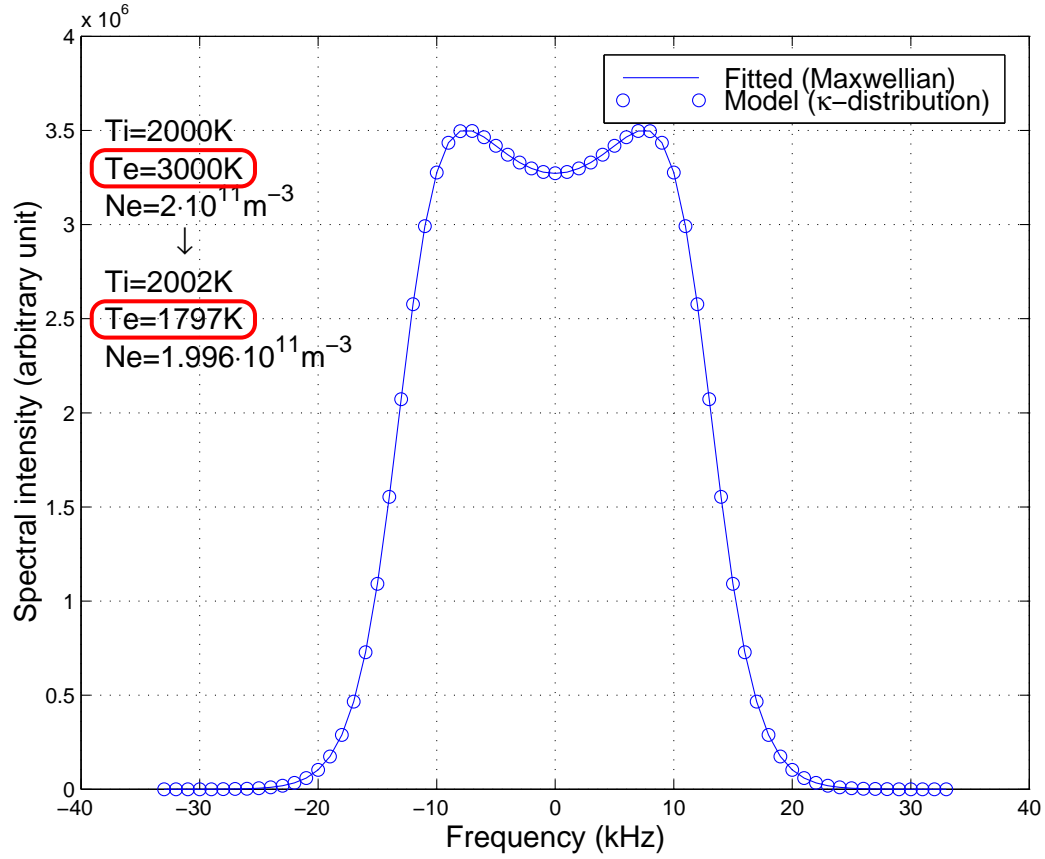


Figure 4.4: An example of fitting on an IS spectrum ($n_e S(\mathbf{k}, \omega)$) with kappa distribution by an IS spectrum with Maxwellian distribution. The model spectrum (*plotted by circles*) assumes $T_i = 2000 K$, $T_e = 3000 K$, $n_e = 2 \cdot 10^{11} m^{-3}$, and $\kappa = 3$. Solid line shows fitted IS spectrum with Maxwellian distribution function with $T_i = 2002 K$, $T_e = 1797 K$, $n_e = 1.996 \cdot 10^{11} m^{-3}$

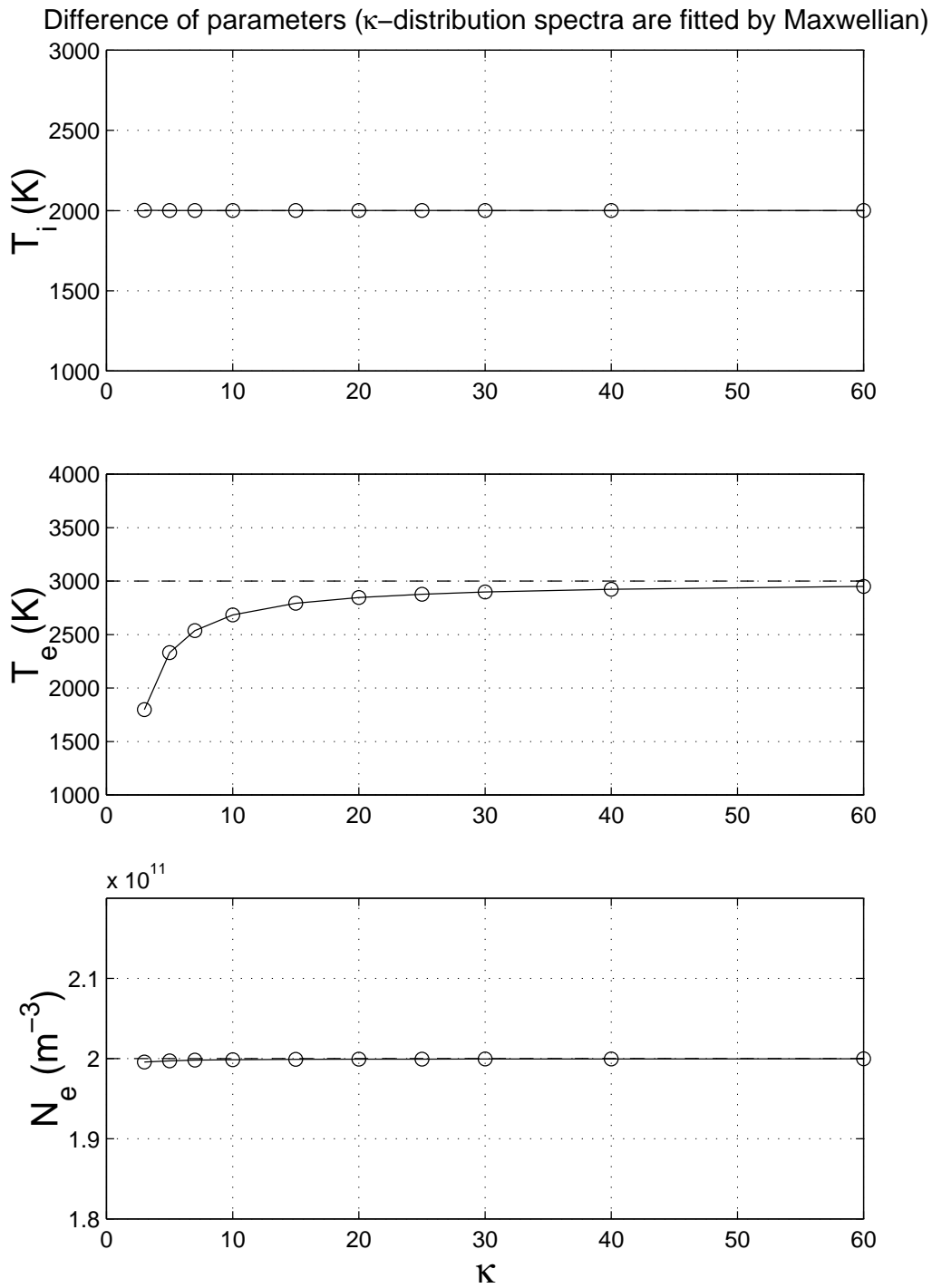


Figure 4.5: The difference of parameters when kappa distribution IS spectra are interpreted by assuming Maxwellian distribution for T_i , T_e , and n_e are shown from the *top* to the *bottom*. They are plotted as relative errors to real (kappa distribution) parameters

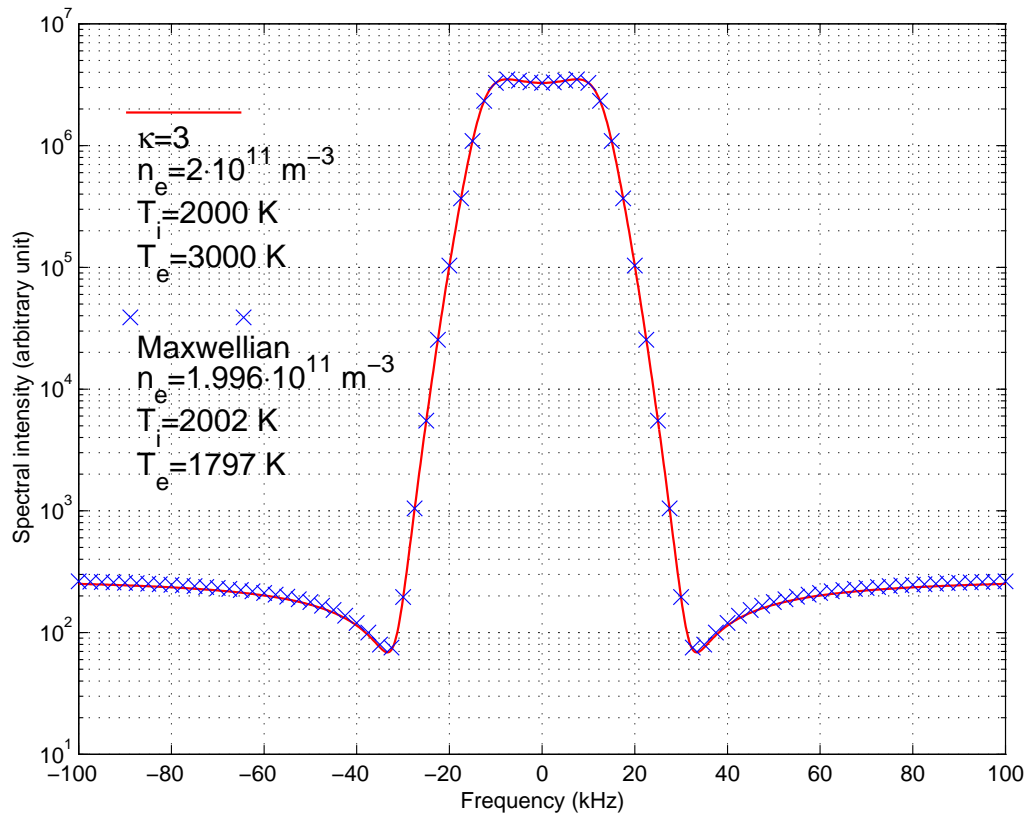


Figure 4.6: The two spectra in Fig. 4.4 are shown for wider range of frequency. *y-axis* is shown in logarithmic scale.

as shown in Fig. 4.1. There, the width of a kappa distribution function is narrower than that of Maxwellian with the same temperature, and a similar width of a Maxwellian distribution function for a lower temperature.

As seen from Fig. 4.4, those two ion line spectra with different T_e for the kappa ($\kappa = 3$) and the Maxwellian distribution function of electrons are so similar that we can hardly distinguish one from the other. Mathematically speaking, those two ion line spectra have actually slight differences in their shapes, and they could be distinguished. But as shown in Fig. 4.6, the difference is very small. Hence in practice, the difference is too small to determine both κ and T_e simultaneously to see how much electrons there are in the high energy tail of the distribution function. Furthermore, noises make it more difficult, practically impossible. So we cannot derive both κ and T_e simultaneously only from ion lines.

The same analysis was performed for the EISCAT VHF radar (transmitted frequency 224 MHz) and the EISCAT Svalbard radar (500 MHz). The same results were obtained for both the radars (not shown here) as the EISCAT UHF radar shown already.

4.3.3 Incoherent scatter spectra with kappa distribution II: plasma lines

The kappa distribution contains many more particles in the high energy tail. That should make a significant effect in the high frequency part of the IS spectrum. Bjørnå and Trulsen (1986) have calculated the effect of a photo electron flux whose energy spectrum are modeled by power law on plasma lines. They find that the total cross section at the EISCAT UHF radar frequency is increased but the position remains the same as it is in the Maxwellian case. Summers and Thorne (1991) have shown that the Langmuir waves of a kappa distribution plasma are more damped than those of Maxwellian plasma, and that the frequency of the Langmuir waves are closer to ω_{pe} . Hence, when $k\lambda_D \ll 1$, it is expected that plasma lines show stronger damping and have a smaller shifts in frequency.

We have calculated plasma lines for various T_e cases with fixed κ , T_i and n_e and

compared them to Maxwellian lines as shown in Fig. 4.7. It can be seen that plasma lines for κ distribution are more strongly damped than they are for Maxwellian for lower T_e ($\lesssim 4000 K$). For higher T_e cases ($\gtrsim 6000 K$), however, plasma lines for Maxwellian are more strongly damped than they are for κ distribution. For $T_e = 10\,000 K$, a plasma line for Maxwellian becomes very flat while that for κ distribution is still relatively sharp. At these high electron temperatures, $k\lambda_D$ becomes comparable to unity. Thus according to Thorne and Summers (1991) wave damping for Maxwellian exceeds that for κ distribution. Our results for higher temperatures are still consistent with previous works. It should be noted that our calculation has been done for $n_e = 2 \cdot 10^{11} m^{-3}$ in such a way that plasma lines for both Maxwellian and kappa distribution function have the same order of their intensities to see clearly the effect of the electron temperature. At the velocity corresponding to the phase velocity of the Langmuir wave with $k = 39.1 m^{-1}$, both distributions have similar number of electrons. If we increase n_e , ω_{pe} is also increased and the phase velocity of the Langmuir waves becomes faster. Then the plasma lines for Maxwellian distribution will be much weaker than the plasma lines for kappa distribution because of the big difference of electron densities at the phase velocity of the Langmuir wave. Svenes *et al.* (1992) have found that their electron distribution function measurements can be explained by a bi-Maxwellian distribution which is a sum of two Maxwellian distribution functions, one of which has a higher temperature than the other. Their model distribution function is still Maxwellian, so it decreases much more rapidly with a velocity in the velocity space than a kappa distribution. Therefore, we expect that the plasma lines for a kappa distribution can be much stronger than those for a bi-Maxwellian distribution, when the phase velocities of the Langmuir waves are enough fast (\leftrightarrow electron densities are higher) to make significant difference of values of a kappa and a bi-Maxwellian distribution functions at the Langmuir wave velocities. The plasma line measurements could distinguish those two (kappa and bi-Maxwellian) distribution functions.

In Fig. 4.8, a calculation of plasma lines for a specific set of T_e and n_e and for various values of κ is shown and compared with a Maxwellian calculation. The positions are slightly shifted toward the transmitter frequency. This becomes clearer for smaller κ .

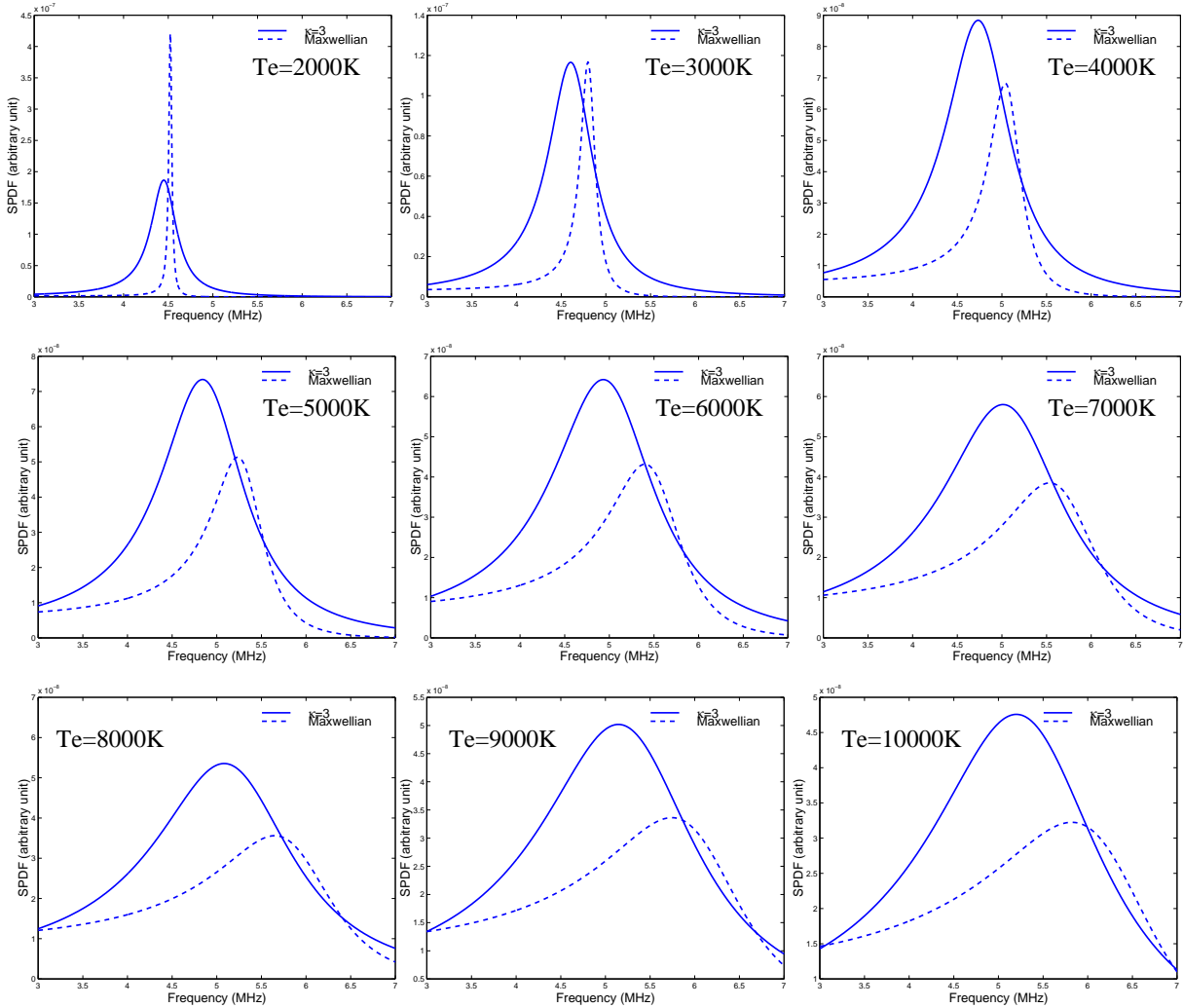


Figure 4.7: Plasma lines (upshifted) for various electron temperatures (2000 - 10 000 K) for $\kappa = 3$ (solid line) and Maxwellian (dashed line) are shown. Electron density is fixed to $2 \cdot 10^{11} \text{ m}^{-3}$. x -axis ranges are all 3 - 7 MHz. But y -axis ranges are arbitrary for each plot

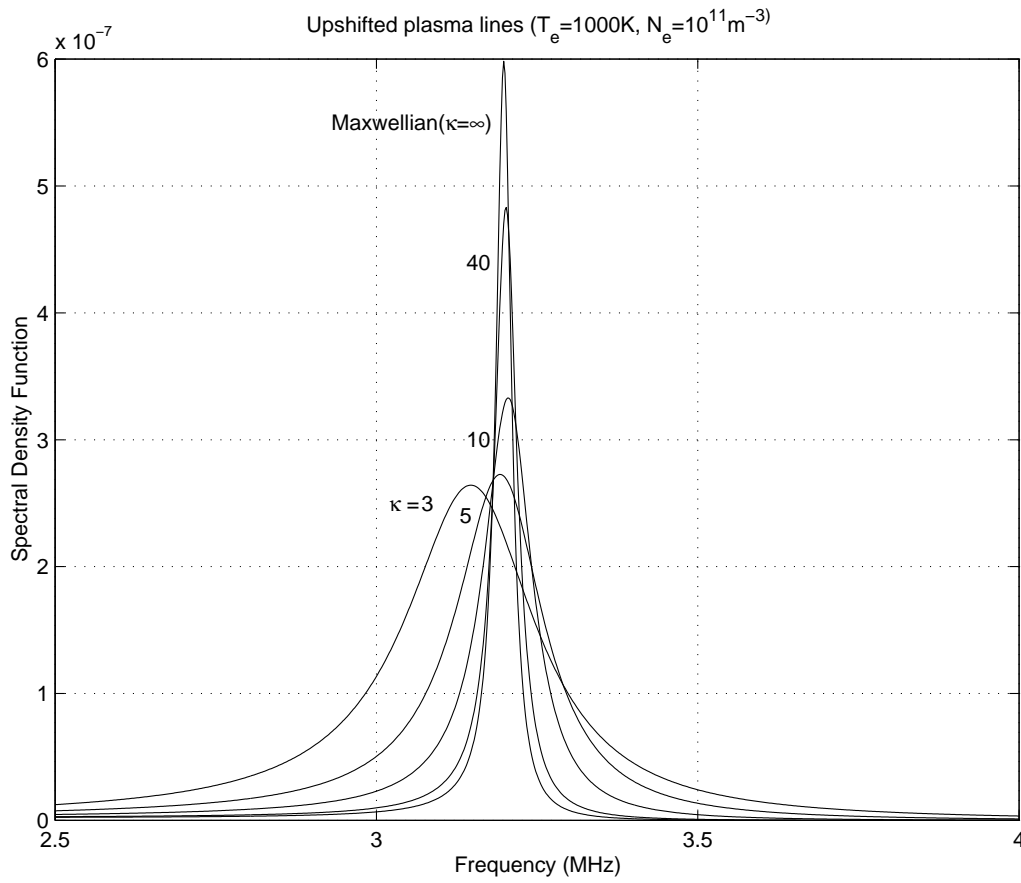


Figure 4.8: Plasma lines (upshifted) are plotted for a different spectral index, $\kappa = 3, 5, 10,$ and $40,$ together with plasma line of Maxwellian plasma ($\kappa = \infty$)

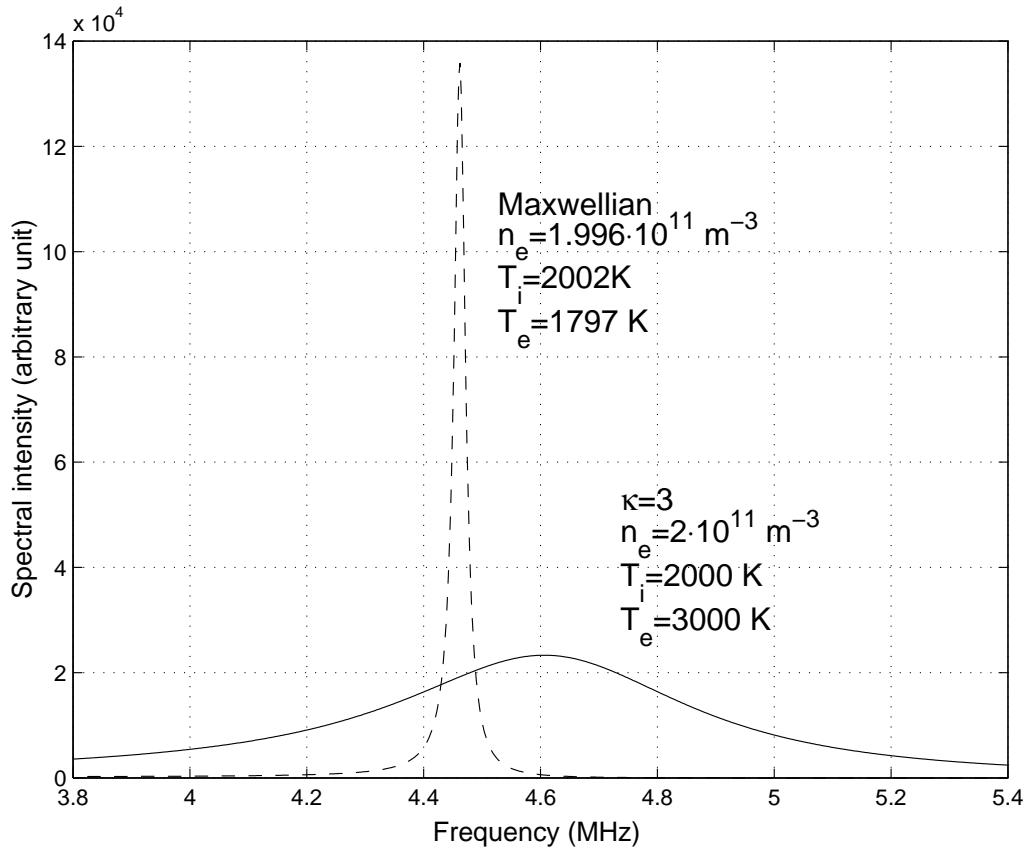


Figure 4.9: Plasma lines (upshifted) are plotted for the sets of parameters appeared in Fig. 4.4, $(n_e, T_i, T_e, \kappa) = (2 \cdot 10^{11} \text{ m}^{-3}, 2000 \text{ K}, 3000 \text{ K}, 3)$ (*solid line*) and $(1.996 \cdot 10^{11} \text{ m}^{-3}, 2002 \text{ K}, 1797 \text{ K}, \infty(\text{Maxwellian}))$ (*dashed line*)

This smaller Doppler frequency of the plasma line with smaller κ can be explained in the following way. The Langmuir dispersion relation is more exactly $\omega \simeq \omega_{pe}(1 + 3k^2 \langle v^2 \rangle / \omega_{pe}^2)^{1/2}$, where $\langle v^2 \rangle$ is the mean square velocity of electrons which is the second order moment of the distribution function. Since $\langle v^2 \rangle = \frac{2\kappa-3}{\kappa} \frac{k_B T}{m}$ for the kappa distribution, $\langle v^2 \rangle$ is smaller for the smaller κ , and consequently the frequency of the Langmuir wave becomes smaller. This means that the Doppler frequency of the plasma line should be smaller for the smaller κ .

We have also calculated plasma lines for the sets of parameters appeared in Fig. 4.4, both of which result in very similar ion line spectra. It is shown in Fig. 4.9. In contrast to the ion lines, these two plasma lines look quite different. Simultaneous measurements of ion lines and plasma lines could enable us to determine both κ and T_e simultaneously, although it is impossible from ion lines only.

4.4 Summary

We have derived incoherent scatter spectra for a plasma when the velocity distribution is a generalized Lorentzian or kappa distribution function.

We have calculated incoherent scatter spectra for a plasma that consists of electrons with a kappa distribution function and ions with a Maxwellian, and compared the spectra with those for a Maxwellian plasma. The ion lines have a double-humped shape similar to those for a Maxwellian plasma. The electron temperatures are, however, underestimated by up to 40 % when interpreting them assuming Maxwellian distributions for both ions and electrons. Ion temperatures and electron densities are almost unchanged. Our results suggest that electron temperatures derived with the assumption of a Maxwellian distribution function might be underestimated when soft electron precipitation is inferred or when intense wave activity is observed. This can lead to the incorrect estimation of forces like ambipolar electric field through the electron temperature.

We have also calculated the plasma lines for the kappa distribution function for electrons with different κ and different temperatures. For $n_e = 2 \cdot 10^{11} m^{-3}$ which is used

in our calculation, plasma lines for κ distribution are more strongly damped than they are for Maxwellian for lower T_e ($\lesssim 4000 K$). For higher T_e cases ($\gtrsim 6000 K$), however, plasma lines for Maxwellian are more strongly damped than they are for κ distribution. For $T_e = 10\,000 K$, a plasma line for Maxwellian becomes very flat while that for κ distribution is still relatively sharp. For smaller κ , the spectral peak is shifted toward the transmitter frequency.

Although practically it is still difficult to measure the shape of a plasma line as we have calculated, simultaneous measurements of plasma lines with ion lines would provide more precise information on the electron distribution function.

Chapter 5

Concluding Remarks

We have studied various effects of electrostatic waves and turbulences on the ionospheric plasma in the E and F regions both experimentally and theoretically.

In Chap. 3, electron heating by Farley-Buneman waves in the lower E region are studied using the data obtained by the EISCAT radar system, the STARE system, and the Killpisjärvi IRIS.

In Sec. 3.1, we have shown that the electron temperatures observed in the E region are clearly isotropic over aspect angles from 0° to about 40° by using the tristatic measurements of the EISCAT CP-1 data even when the electron temperatures are strongly enhanced. The very high heating rates that we derived from the observed T_e suggest that Farley-Buneman waves have an electric field component both perpendicular and parallel to \mathbf{B} as proposed by St.-Maurice (1987). If T_e enhancement is instead due to a direct scattering of electrons by wave fields not involving electron-neutral collisions, our observation implies that these waves should be isotropic. We think that our result of isotropic T_e is remarkable in light of the known strong anisotropy of the Farley-Buneman waves, which is the cause of heating. We feel that further clarifications of the underlying heating processes are needed in the future.

In Sec. 3.2, we have argued that because the total energy is conserved, the chain of processes, namely, growth of electrostatic waves, acceleration and heating of the electrons, and their cooling in inelastic collisions with neutrals must be maintained by a

quasi-stationary MI current system. We have parameterized the effects of the waves and turbulences by the anomalous (or effective) collision frequency ν_e^* as a kind of drag effect. We have found that the bulk electron velocity deviates by up to about 7° ($\nu_e^* \sim 30\nu_{en}$) from the $\mathbf{E} \times \mathbf{B}$ drift direction resulting in the additional Pedersen current carried by electrons during events with high $|\mathbf{E}|$. We have examined the importance of the electron Pedersen currents, and found that at altitudes $\lesssim 110$ km this current can become the main Pedersen current. Consequently, the current-voltage relation in the Earth's ionosphere is non-linear. Although this non-linearity appears to be rather innocent, consequences could occur in the Magnetosphere-Ionosphere coupling. This should be examined more thoroughly in the future. Although the flow angle rotation of electrons could not be confirmed by observations by the STARE system due to the saturation of the irregularity phase velocity at C_s , we have pointed out the possibility of testing our estimation by optical instruments.

In Sec. 3.3, we have examined the nature of ν_e^* using CNA measurements by the Kilpisjärvi IRIS. We have shown that the cosmic noise absorption observed by the Kilpisjärvi IRIS can be well explained by Eq. (3.13) (or Eq. (3.14)) in which only the classical electron-neutral collision frequency is taken into account, even when ν_e^* greatly exceeds the classical frequencies associated with strong electric fields and strong electron temperature enhancements. These results strongly suggest that the ν_e^* has no effect in absorption of radio waves in the ionosphere, although it can parameterize the dissipation of the electromagnetic energy to electrons. Therefore, this anomalous collision frequency has a rather limited range of application. The waves should have a drag effect equivalent to the collisions of ν_e^* times per second on the electron drift, but ν_e^* is not necessarily equivalent to the classical collision frequency in the other phenomena. Our results agree with both previous experimental results (Stauning, 1984; Stauning and Olesen, 1989) and the theoretical prediction with macroscopic consideration in Appendix A.

In Chap. 4, we have studied incoherent scatter spectra which are scattering of electromagnetic waves by the two basic types of electrostatic waves, the ion acoustic waves and the Langmuir waves. The motivation of our study was based on the anticipation that in

the F region energy inputs such as soft electron precipitation could excite the Langmuir turbulence and could modify the electron distribution function. We have derived incoherent scatter spectra for a plasma when the velocity distribution is a generalized Lorentzian or kappa distribution function.

We have calculated incoherent scatter spectra for a plasma that consists of electrons with a kappa distribution function and ions with a Maxwellian, and compared the spectra with those for a Maxwellian plasma. The ion lines have a double-humped shape similar to those for a Maxwellian plasma. The electron temperatures are, however, underestimated by up to 40 % when interpreting them assuming Maxwellian distributions for both ions and electrons. Ion temperatures and electron densities are almost unchanged.

This kind of analysis could be used when soft electron precipitation is inferred or when intense wave activity is observed. For example, electron temperature enhancements caused by soft electron precipitation which is also associated with ion outflow are often observed with EISCAT radars. Our results suggest that in such cases electron temperatures derived with the assumption of a Maxwellian distribution function might be underestimated. This can lead to the incorrect estimation of forces such as an ambipolar electric field through the electron temperature. Correctly analyzed data would significantly contribute to the understanding of ionospheric phenomena such as ion upflows and enhanced ion acoustic echoes.

Another application of our analysis is for a heating experiment in which the ionosphere is artificially modified and heated by powerful electromagnetic waves. In such an experiment, one would expect a strongly distorted electron distribution function. Although it is not certain if the electron distribution function can be modeled by the kappa distribution, we believe that it is a good example to test our analysis.

We have also calculated the plasma lines for the kappa distribution function for electrons. We have found a significant difference in the shape and a slight difference in the frequency shift. Although practically it is still difficult to measure the shape of a plasma line as we have calculated, simultaneous measurements of the shape of plasma lines with ion lines would enable us to determine the spectral index κ , and would provide more

precise information on the electron distribution function.

Appendix A

The Electromagnetic Wave

Propagation in the Turbulent Plasma

In this appendix, we examine the effect of the irregularities on an electromagnetic wave propagation through the turbulent plasma. We shall follow a procedure which was used by Hagfors (1984) to discuss the effect of heater-induced field aligned plasma density irregularities in ionospheric RF modification experiments. The mathematical procedure was originally developed by Karal and Keller (1964) and found application by Liu (1967) for magnetoplasmas for the case of high frequencies and for isotropic density irregularities. The theory is a macroscopic theory, and is not concerned with the detailed microscopic nature of ion-neutral and electron-neutral reactions.

A.1 The wave propagation problem

Consider an electromagnetic wave of frequency ω and wave vector \mathbf{k} . In a homogeneous plasma of density N the electric field of the wave is assumed to be of the form $\mathbf{E}(\mathbf{k}, \omega) \exp(i(\mathbf{k} \cdot \mathbf{r} - \omega t))$. If the medium is no longer homogeneous but contains density irregularities the propagation of an electromagnetic wave is changed and the effect may be represented by a modification of the complex refractive index governing a “mean” wave with field amplitude $\mathbf{E}_0(\mathbf{k}, \omega)$ and with wave vector \mathbf{k} . We shall search for the effect of

the plasma irregularities in the properties of this "mean" wave.

Following closely the procedure of Hagfors (1984), but modifying the procedure where it is unclear, we first Fourier expand the electric field and the polarization associated with the wave as

$$\begin{Bmatrix} \mathbf{P}(\mathbf{r}, t) \\ \mathbf{E}(\mathbf{r}, t) \end{Bmatrix} = \left(\frac{1}{2\pi} \right)^4 \iiint\!\!\!\int d(\mathbf{k})d\omega \begin{Bmatrix} \mathbf{P}(\mathbf{k}, \omega) \\ \mathbf{E}(\mathbf{k}, \omega) \end{Bmatrix} e^{i(\mathbf{k}\cdot\mathbf{r}-\omega t)} \quad (\text{A.1})$$

We shall assume that the relation between the polarization of the medium and the electric field is local in space and governed by a susceptibility tensor $\tilde{\chi}(\mathbf{r}, t)$ (we shall use tilde to denote tensors in what follows):

$$\mathbf{P}(\mathbf{r}, t) = \epsilon_0 \int d\tau \tilde{\chi}(\mathbf{r}, t - \tau; t) \mathbf{E}(\mathbf{r}, \tau) \quad (\text{A.2})$$

We allow the medium to be time-varying in addition to being dispersive in time, as one must expect of the electrojet plasma. Note that this relation is deceptively simple. The medium we are considering here is not translationally invariant. Strictly speaking one has the following relation between the polarization and the electric field:

$$\mathbf{P}(\mathbf{r}, t) = \epsilon_0 \int_V d(\mathbf{r}') \int_{-\infty}^t dt' \tilde{\chi}(\mathbf{r}; \mathbf{r}', t; t') \mathbf{E}(\mathbf{r}', t') \quad (\text{A.3})$$

The convolution relationship normally used between the field and the polarization therefore also depends on the position and the time, and not only on position and time differences. We can think of (A.2) as dealing with quantities after averaging over the microscopic spatial scale, but not over the scale of the turbulent irregularities.

The Fourier components of the polarization is given by:

$$\begin{aligned} \mathbf{P}_0(\mathbf{k}, \omega) = & \epsilon_0 \tilde{\chi}_0(\omega) \mathbf{E}_0(\mathbf{k}, \omega) + \\ & \epsilon_0 \left(\frac{1}{2\pi} \right)^4 \iiint\!\!\!\int d(\mathbf{q})d\omega' < \tilde{\chi}_1(\mathbf{k} - \mathbf{q}, \omega - \omega'; \omega) \mathbf{E}_1(\mathbf{q}, \omega') > \end{aligned} \quad (\text{A.4})$$

We have added an extra argument in the susceptibility function to indicate that this function not only depends on differences in frequencies, but also on the frequencies themselves.

We have split the susceptibility and the field quantities into a mean over the ensemble of realizations of the turbulent medium and a zero mean part:

$$\begin{aligned}\tilde{\chi} &= \tilde{\chi}_0 + \tilde{\chi}_1 & \langle \tilde{\chi} \rangle &= \tilde{\chi}_0 \\ \mathbf{E} &= \mathbf{E}_0 + \mathbf{E}_1 & \langle \mathbf{E} \rangle &= \mathbf{E}_0 \\ \mathbf{P} &= \mathbf{P}_0 + \mathbf{P}_1 & \langle \mathbf{P} \rangle &= \mathbf{P}_0\end{aligned}\tag{A.5}$$

If we can express $\mathbf{E}_1(\mathbf{q}, \omega)$ in (A.4) in terms of the mean field $\mathbf{E}_0(\mathbf{k}, \omega)$ we can substitute into the equation to obtain a dispersion equation for the mean field, and determine the refractive index and the absorption of the mean wave.

By means of Maxwell's equations we relate the polarization perturbation to the electric field perturbation:

$$\frac{1}{\epsilon_0} \mathbf{P}_1(\mathbf{k}, \omega) = \tilde{N}(\mathbf{k}, \omega) \mathbf{E}_1(\mathbf{k}, \omega)\tag{A.6}$$

where the elements in the $\tilde{N}(\mathbf{k}, \omega)$ matrix are:

$$N_{lm} = \left(\frac{c^2 k^2}{\omega^2} - 1 \right) \delta_{lm} - \frac{c^2}{\omega^2} k_l k_m\tag{A.7}$$

where c is the velocity of light in vacuum. Using the constitutive relation, on the other hand, we have:

$$\begin{aligned}\frac{1}{\epsilon_0} \mathbf{P}_1(\mathbf{k}, \omega) &= \tilde{\chi}_0(\omega) \mathbf{E}_1(\mathbf{k}, \omega) + \\ &\left(\frac{1}{2\pi} \right)^4 \iiint d(\mathbf{q}) d\omega' \tilde{\chi}_1(\mathbf{k} - \mathbf{q}, \omega - \omega'; \omega) \mathbf{E}_0(\mathbf{q}, \omega')\end{aligned}\tag{A.8}$$

Equating (A.8) and (A.6) we obtain the desired relation between $\mathbf{E}_0(\mathbf{q}, \omega)$ and $\mathbf{E}_1(\mathbf{k}, \omega)$ for substitution into (A.4):

$$\begin{aligned}\mathbf{E}_1(\mathbf{k}, \omega) &= \left(\frac{1}{2\pi} \right)^4 [\tilde{N}(\mathbf{k}, \omega) - \tilde{\chi}_0(\omega)]^{-1} \\ &\times \iiint d(\mathbf{q}) d\omega' \tilde{\chi}_1(\mathbf{k} - \mathbf{q}, \omega - \omega'; \omega) \mathbf{E}_0(\mathbf{q}, \omega')\end{aligned}\tag{A.9}$$

Because the statistical properties of the medium are assumed to be independent of position the susceptibility deviations satisfy the following condition:

$$\begin{aligned}\langle \tilde{\chi}_1(\mathbf{k}_1, \omega_1) \tilde{\chi}_1(\mathbf{k}_2, \omega_2) \rangle &= \\ (2\pi)^4 \langle \tilde{\chi}_1(\mathbf{k}_1, \omega_1) \tilde{\chi}_1(-\mathbf{k}_1, -\omega_1) \rangle &= \delta(\mathbf{k}_1 + \mathbf{k}_2) \delta(\omega_1 + \omega_2)\end{aligned}\tag{A.10}$$

we end up with a dispersion equation for the mean wave, essentially the same as in Hagfors (1984), except that the time variation of the fluctuations are accounted for, possibly in the form of a density wave:

$$[\tilde{N}(\mathbf{k}, \omega) - \tilde{\chi}_0(\omega)]\mathbf{E}_0(\mathbf{k}, \omega) = \left(\frac{1}{2\pi}\right)^4 \iiint d(\mathbf{q})d\omega' < \tilde{\chi}_1(\mathbf{k} - \mathbf{q}, \omega - \omega')[\tilde{N}(\mathbf{q}, \omega') - \tilde{\chi}_0(\omega')]^{-1}\tilde{\chi}_1(\mathbf{q} - \mathbf{k}, \omega' - \omega) > \mathbf{E}_0(\mathbf{k}, \omega) \quad (\text{A.11})$$

where we have left out the possible explicit dependence of $\tilde{\chi}_1$ on ω .

The assumption about the susceptibility in (A.10) basically means that we consider the susceptibility deviations as a superposition of statistically independent plane waves corresponding to density waves of the form:

$$N(\mathbf{r}, t) = N_0 + n_1 \cdot e^{i\mathbf{q}(\mathbf{r}-tC_s)} + n_1^* \cdot e^{-i\mathbf{q}(\mathbf{r}-tC_s)} \quad (\text{A.12})$$

Here C_s is the phase velocity of the acoustic waves in the electrojet, N_0 the mean electron density and n_1 the amplitude of the density perturbation.

Introducing

$$X_0 = \frac{N_0 e^2}{m\epsilon_0 \omega^2} \quad X_1 = \frac{n_1 e^2}{m\epsilon_0 \omega^2} \quad X_1^* = \frac{n_1^* e^2}{m\epsilon_0 \omega^2} \quad (\text{A.13})$$

we obtain for the susceptibilities:

$$\tilde{\chi} = -\tilde{M}X = -\tilde{M}X_0 - \tilde{M}X_1 \cdot e^{i\mathbf{q}(\mathbf{r}-tC_s)} - \tilde{M}X_1^* \cdot e^{-i\mathbf{q}(\mathbf{r}-tC_s)} \quad (\text{A.14})$$

with the matrix \tilde{M} defined by:

$$\tilde{M} = \frac{1}{(1+iZ)^2 - Y^2} \left\{ \begin{array}{ccc} 1+iZ & -iY & 0 \\ iY & 1+iZ & 0 \\ 0 & 0 & ((1+iZ)^2 - Y^2)/(1+iZ) \end{array} \right\} \quad (\text{A.15})$$

assuming that the coordinate system is chosen so that the geomagnetic field is directed along the z-axis, and the x and the y axes are normal to z, with the x-axis in the magnetic

meridian plane. In addition to the definition of X above we have also introduced the standard notations:

$$\begin{aligned}
Y &= \Omega_e/\omega \\
Z &= \nu_e/\omega \\
\omega_p^2 &= N(\mathbf{r}, t)e^2/m\epsilon_0 \\
\omega &= \text{wave frequency} \\
\Omega_e &= eB/m \\
\nu_e &= \text{electron collision frequency}
\end{aligned}$$

In this notation it is shown in Hagfors 1984 that the dispersion equation, for plane wave density striations, takes the form:

$$\begin{aligned}
\text{Det} = & \| \tilde{M}(\omega)^{-1} \tilde{N}(\mathbf{k}, \omega) + X_0(\omega - C_s q) \tilde{I} + \\
& \langle |X_{-1}(\omega - C_s q)|^2 \rangle \left\{ \tilde{M}(\omega - C_s q)^{-1} \tilde{N}(\mathbf{k} - \mathbf{q}; \omega - C_s q) + X_0(\omega - C_s q) \tilde{I} \right\}^{-1} + \\
& \langle |X_1(\omega + C_s q)|^2 \rangle \left\{ \tilde{M}(\omega + C_s q)^{-1} \tilde{N}(\mathbf{k} + \mathbf{q}; \omega + C_s q) + X_0(\omega + C_s q) \tilde{I} \right\}^{-1} \| \\
& = 0 \tag{A.16}
\end{aligned}$$

With this dispersion equation we ought to be able to discuss the problem of propagation of an electromagnetic wave through a turbulent plasma in a single scattering approximation. This should be appropriate to the discussion of anomalous attenuation of the riometer waves through the electrojet.

A.2 The riometer case.

Substitution into (A.16) leads to rather complicated expressions, as shown in Hagfors (1984) even for simplified cases. There simplification was achieved by assuming that the length of the propagating wave was much larger than the scale of the irregularities, and even so the dispersion equation was quite complex. For the cases we consider here we shall make other approximations. In the riometer, it will be assumed that the wave frequency

used, often in the range 30-50 MHz, by far exceeds the gyro-frequency, i.e. that $Y \ll 1$, so that the basic wave propagation will be as if in a non-magnetized plasma, i.e.

$$\tilde{\chi} = -\tilde{M}X = -\frac{X}{1+iZ}\tilde{I} \quad (\text{A.17})$$

We shall furthermore assume, somewhat unrealistically, that the density waves travel in a direction perpendicularly to the magnetic field. This direction is that of the electron drift. In reality, of course the mean current must be directed horizontally, and the waves must be inhomogeneous also traveling horizontally but with their wave normal perpendicular to \mathbf{B} . This means that q_z , the component of \mathbf{q} along the magnetic field is zero. For the purpose of assessing their effect on the absorption we shall adopt this simpler geometry. We assume that the electromagnetic wave travels vertically and that the angle between \mathbf{k} and the z -axis is θ . As we shall see presently even this simplification lead to intractable expressions, and we shall end up setting θ equal to zero thus considering the magnetic field to also be vertical.

Substitute into the dispersion equation (A.16), noting that $\omega - C_s q \approx \omega$ and that $\tilde{M}^{-1} \approx (1+iZ)\tilde{I}$ we obtain:

$$\begin{aligned} \text{Det} = & \left| (1+iZ)\tilde{N}(\mathbf{k}, \omega) + X_0(\omega)\tilde{I} \right. \\ & + \left. \langle |X_{-1}(\omega)|^2 \rangle \left\{ (1+iZ)\tilde{N}(\mathbf{k} - \mathbf{q}; \omega) + X_0(\omega)\tilde{I} \right\}^{-1} \right. \\ & \left. + \langle |X_1(\omega)|^2 \rangle \left\{ (1+iZ)\tilde{N}(\mathbf{k} + \mathbf{q}; \omega) + X_0(\omega)\tilde{I} \right\}^{-1} \right| = 0 \end{aligned} \quad (\text{A.18})$$

Simplification of the general expressions containing $\mathbf{k} \pm \mathbf{q}$ does not seem to be possible here because the electromagnetic wave used and the density wave of the electrojet may have comparable wavelengths.

In order to obtain a tractable dispersion equation we have to explicitly determine the form of both $\tilde{N} - (X_0/(1+iZ))\tilde{I}$ and its inverse. With the abbreviations $D = 1 - X_0/(1+iZ)$ and $A = c^2/\omega^2$ we have:

$$\tilde{N} - \tilde{\chi}_0 = \begin{Bmatrix} A(k_y^2 + k_z^2) - D & -Ak_x k_y & -Ak_x k_z \\ -Ak_x k_y & A(k_x^2 + k_z^2) - D & -Ak_y k_z \\ -Ak_x k_z & -Ak_y k_z & A(k_y^2 + k_x^2) - D \end{Bmatrix} \quad (\text{A.19})$$

with the inverse, which is also needed:

$$(\tilde{N} - \tilde{\chi}_0)^{-1} = \frac{1}{D(D - Ak^2)} \begin{pmatrix} Ak_x^2 - D & Ak_x k_y & Ak_x k_z \\ Ak_x k_y & Ak_y^2 - D & Ak_y k_z \\ Ak_x k_z & Ak_y k_z & Ak_z^2 - D \end{pmatrix} \quad (\text{A.20})$$

As a model which may show effects of the density waves, and which will simplify the mathematics even further, we shall consider the case where the electromagnetic wave travels along the magnetic field, i.e. where $\theta = 0$. In this case the only component of \mathbf{k} is $k_z = k$, and of \mathbf{q} is $q_x = q$. The two matrices needed in the dispersion equation now are:

$$\tilde{N} - \tilde{\chi}_0 = \begin{pmatrix} Ak^2 - D & 0 & \mp Aqk \\ 0 & A(q^2 + k^2) - D & 0 \\ \mp Aqk & 0 & Aq^2 - D \end{pmatrix} \quad (\text{A.21})$$

and

$$(\tilde{N} - \tilde{\chi}_0)^{-1} = \frac{1}{D(D - A(k^2 + q^2))} \begin{pmatrix} Aq^2 - D & 0 & \pm Aqk \\ 0 & -D & 0 \\ \pm Aqk & 0 & Ak^2 - D \end{pmatrix} \quad (\text{A.22})$$

With these substitutions in (A.18) we obtain the following dispersion relation:

$$\begin{aligned} & \left(Ak^2 - D + \frac{2 \langle |X_1|^2 \rangle (Aq^2 - D)}{D(D - A(k^2 + q^2))} \right) \times \\ & \left(Ak^2 - D - \frac{2 \langle |X_1|^2 \rangle}{(D - A(k^2 + q^2))} \right) \times \\ & \left(-D + \frac{2 \langle |X_1|^2 \rangle (Ak^2 - D)}{D(D - A(k^2 + q^2))} \right) = 0 \end{aligned} \quad (\text{A.23})$$

Setting to zero the first term in this product gives the dispersion equation for the x-component of the field, the second term the y component and the third term the z, or the longitudinal component. The x and the y components are the transverse components of the electromagnetic wave, which is of interest here. The two have slightly different dispersion relations because of the different orientation of the electric field with respect to the density wave. The approximate solutions for the two equations under the assumption

made are, for E_x , the field aligned with the wave vector \mathbf{q} of the density wave:

$$n^2 \approx n_0^2 + 2 \frac{\langle |X_1|^2 \rangle}{n_0^2} \left(1 - \left(\frac{k}{q} \right)^2 \right) \quad (\text{A.24})$$

and for E_y , the component with the field normal to \mathbf{q} the solution is:

$$n^2 \approx n_0^2 - 2 \frac{\langle |X_1|^2 \rangle}{n_0^2} \left(\frac{k}{q} \right)^2 \quad (\text{A.25})$$

Here we have introduced the refractive index of the mean wave, n , and the refractive index of the wave without density perturbations, n_0 determined by $n_0^2 = 1 - X_0/(1 + iZ)$.

Typically we have X_0 in the range 0.01 to 0.04, and probably the density perturbation less than 10%, we have $\langle |X_1|^2 \rangle$ in the range 10^{-6} to 10^{-5} so that the correction for the presence of the plasma turbulence must be very small. Only when the frequency is near a plasma resonance in the non-perturbed medium is there a chance for the turbulence to play a decisive role. With the present assumptions that is not the case, and we conclude that anomalous absorption is of negligible importance in riometer observations.

Appendix B

Plasma Dispersion Equation: Kinetic Treatment

In this appendix, we demonstrate the derivation of an equation which describes properties of plasma wave dispersion by kinetic treatment. First, useful transforms for this purpose, the Fourier transform and the Laplace transform are explained. Then starting from basic kinetic equations, we finally derive the plasma dispersion equation (Eq. (4.27)).

B.1 Fourier Transforms

The Fourier transform is one of the most commonly used integral transforms and very useful in solving differential equations. This transform of $f(\mathbf{r})$ which is a function in three-dimensional space and its inverse transform can be defined as

$$f(\mathbf{k}) = \int_{-\infty}^{+\infty} d\mathbf{r} f(\mathbf{r}) e^{+i\mathbf{k}\cdot\mathbf{r}} \quad (\text{B.1})$$

$$f(\mathbf{r}) = \frac{1}{(2\pi)^3} \int_{-\infty}^{+\infty} d\mathbf{k} f(\mathbf{k}) e^{-i\mathbf{k}\cdot\mathbf{r}} \quad (\text{B.2})$$

This transform can include a transform in time,

$$f(\omega) = \int_{-\infty}^{+\infty} dt f(t) e^{-i\omega t} \quad (\text{B.3})$$

$$f(t) = \frac{1}{2\pi} \int_{-\infty}^{+\infty} d\omega f(\omega) e^{+i\omega t} \quad (\text{B.4})$$

In the Fourier transform, \mathbf{k} and ω are real. For the kinetic treatment of a plasma, we are required to use the Laplace transform in time which is described in the next section.

B.2 Laplace Transforms

The Laplace transform may be defined as

$$f(\omega) = \int_0^{\infty} dt f(t) e^{-(i\omega + \gamma)t} \quad (\text{B.5})$$

where $\gamma > 0$. The factor $e^{-\gamma t}$ must be large enough for this integral to converge. The inverse transform is

$$f(t) = \frac{1}{2\pi} \int_{-\infty}^{+\infty} d\omega' f(\omega') e^{+(i\omega' + \gamma)t} \quad (\text{B.6})$$

If we set $\omega = \omega' - i\gamma$,

$$f(t) = \frac{1}{2\pi} \int_{-i\gamma - \infty}^{-i\gamma + \infty} d\omega f(\omega) e^{i\omega t} \quad (\text{B.7})$$

Since we have defined $\gamma > 0$, the transform applies to the lower half of the ω plane, and the contour of integration must be closed below $\text{Im}(\omega) < -\gamma$. When the contour needs to be on the upper half plane, the function $f(\omega)$ must be analytically continued.

B.3 Basic Equations

Here we derive the plasma dispersion equation with a kinetic treatment. We start from a microscopic distribution function,

$$F_s(\mathbf{r}, \mathbf{v}, t) = \sum_{j=1}^{N_q} \delta(\mathbf{r} - \mathbf{r}_j) \delta(\mathbf{v} - \mathbf{v}_j) \quad (\text{B.8})$$

where $\delta(\mathbf{r})$ is the Dirac delta-function. This means that the j -th particle is exactly at a position \mathbf{r} with a velocity \mathbf{v} at a time t . N_q is the total number of particles which satisfies

$$N_q = \int d\mathbf{r} d\mathbf{v} F_s(\mathbf{r}, \mathbf{v}, t) \quad (\text{B.9})$$

and the number density in space is given by

$$n_s(\mathbf{r}, t) = \int d\mathbf{v} F_s(\mathbf{r}, \mathbf{v}, t) \quad (\text{B.10})$$

The distribution function satisfies the Klimontovic equation

$$\frac{\partial F_s}{\partial t} + \mathbf{v} \cdot \frac{\partial F_s}{\partial \mathbf{r}} + \mathbf{a} \cdot \frac{\partial F_s}{\partial \mathbf{v}} = 0 \quad (\text{B.11})$$

In an unmagnetized plasma, it is reasonable to set the acceleration term

$$\mathbf{a} = \frac{q_s}{m_s} \mathbf{E} \quad (\text{B.12})$$

For small fluctuation, we set

$$F_s = F_{s0} + F_{s1}(\mathbf{r}, \mathbf{v}, t) \quad (\text{B.13})$$

$$\mathbf{E} = 0 + \mathbf{E}_1 \quad (\text{B.14})$$

and

$$n_s = n_{s0} + n_{s1}(\mathbf{r}, \mathbf{v}, t) \quad (\text{B.15})$$

With this expanded distribution function, we form a hierarchy of equations (For details, see Sheffield, 1975, A.2.7). The hierarchy is terminated at the two-particle correlation level, and for a stationary and homogeneous plasma at a low temperature with no magnetic field, the system is described by the following equations.

$$\frac{\partial F_{s0}}{\partial t} + \mathbf{v} \cdot \frac{\partial F_{s0}}{\partial \mathbf{r}} = 0 \quad (\text{B.16})$$

$$\frac{\partial F_{s1}}{\partial t} + \mathbf{v} \cdot \frac{\partial F_{s1}}{\partial \mathbf{r}} + \frac{q_s}{m_s} \mathbf{E}_1 \cdot \frac{\partial F_{s1}}{\partial \mathbf{v}} = \left(\frac{\partial F_{s1}}{\partial t} \right)_c \quad (\text{B.17})$$

$$\nabla \cdot \mathbf{E}_1 = \sum_s \frac{q_s}{\epsilon_0} \int F_{1s} d\mathbf{v} \quad (\text{B.18})$$

The right-hand-side of Eq. (B.17) represents collisions. To include the effects of collisions, we adopt the BGK collision term

$$\left(\frac{\partial F_{s1}}{\partial t} \right)_c = -\nu_s [F_{s1} - n_{s1} f_{s0}] \quad (\text{B.19})$$

where

$$n_{s1} = \int d\mathbf{v} F_{s1}(\mathbf{r}, \mathbf{v}, t) \quad (\text{B.20})$$

and f_{s0} is defined by

$$F_{s0} = n_{0s} f_{s0} \quad (\text{B.21})$$

B.4 Plasma Dispersion Equation

Below we adopt the Fourier transform in space and the Laplace transform in time. By this transform, for the distribution function and for the density, we have

$$F_{s1}(\mathbf{k}, \mathbf{v}, \omega) = \int_{-\infty}^{+\infty} e^{i\mathbf{k}\cdot\mathbf{r}} d\mathbf{k} \int_{-\infty}^{+\infty} F_{s1}(\mathbf{r}, \mathbf{v}, t) e^{-i(\omega-i\gamma)t} dt \quad (\text{B.22})$$

and

$$n_e(\mathbf{k}, \omega - i\gamma) = \int_{-\infty}^{+\infty} e^{i\mathbf{k}\cdot\mathbf{r}} d\mathbf{r} \int_{-\infty}^{+\infty} n_e(\mathbf{r}, t) e^{-i(\omega-i\gamma)t} dt \quad (\text{Eq. (4.3)})$$

From Poission's equation B.18 becomes

$$\begin{aligned} \nabla \cdot \mathbf{E}_1 &= \frac{1}{\epsilon_0} \rho_{q1}(\mathbf{r}, t) \\ &= \frac{1}{\epsilon_0} \frac{1}{(2\pi)^3} \int_{-\infty}^{+\infty} \rho_{q1}(\mathbf{k}, t) e^{i\mathbf{k}\cdot\mathbf{r}} d\mathbf{k} \end{aligned} \quad (\text{B.23})$$

and this leads to

$$\mathbf{E}_1 = \frac{i}{\epsilon_0} \frac{1}{(2\pi)^3} \int_{-\infty}^{+\infty} \rho_{q1}(\mathbf{k}, t) e^{i\mathbf{k}\cdot\mathbf{r}} \frac{\mathbf{k}}{k^2} \cdot d\mathbf{k} \quad (\text{B.24})$$

Laplace transform of Eq. (B.17) with the collision term (Eq. (B.19)) becomes

$$\begin{aligned} -F_{s1}(\mathbf{k}, \mathbf{v}, t=0) + [i\omega + \nu_s - i\mathbf{k} \cdot \mathbf{v}] F_{s1}(\mathbf{k}, \mathbf{v}, \omega) \\ = -i \frac{q_s}{\epsilon_0 m_s k^2} \rho_{q1}(\mathbf{k}, \omega) \mathbf{k} \cdot \frac{\partial F_{s0}}{\partial \mathbf{v}} + \nu_s n_{s1}(\mathbf{k}, \omega) f_{s0} - n_{s1}(\mathbf{k}, t=0) \end{aligned} \quad (\text{B.25})$$

Solving this equation for $\rho(\mathbf{k}, \omega)$ with the help of the relation

$$\rho_{q1}(\mathbf{k}, \omega) = \sum_s q_s n_{s1}(\mathbf{k}, \omega) \quad (\text{B.26})$$

we obtain

$$\rho_{q1}(\mathbf{k}, \omega) = \frac{g(\mathbf{k}, \mathbf{v}, t=0)}{1 + \sum_s C_s(\mathbf{k}, \omega)} \quad (\text{B.27})$$

where $g(\mathbf{k}, \mathbf{v}, t=0)$ is a function which is related to the initial state of a plasma, and $C_s(\mathbf{k}, \omega)$ is given by Eq. (4.5). (not the ion acoustic velocity) By the inverse Laplace transform, we obtain

$$\rho_{q1}(\mathbf{k}, t) = \frac{1}{2\pi} \int_{-i\gamma-\infty}^{-i\gamma+\infty} \frac{g(\mathbf{k}, \mathbf{v}, t=0)}{1 + \sum_s C_s(\mathbf{k}, \omega)} e^{i\omega t} d\omega \quad (\text{B.28})$$

where $g(\mathbf{k}, \mathbf{v}, t = 0)$ is a function of $F_{s1}(\mathbf{k}, \mathbf{v}, t = 0)$ which represents an initial perturbation at $t = 0$. Poles of the integrand of the right-hand-side of this equation which contribute to the value of the integral come from both the numerator and the denominator. The contribution from the numerator, $g(\mathbf{k}, \mathbf{v}, t = 0)$ is, however, rapidly approaching zero. Hence, for non-trivial solutions, we must have for ions and electrons

$$\epsilon(\mathbf{k}, \omega) \equiv 1 + C_i(\mathbf{k}, \omega) + C_e(\mathbf{k}, \omega) = 0 \quad (\text{B.29})$$

$\epsilon(\mathbf{k}, \omega)$ is the plasma dielectric function which appeared in Chap. 4 as Eq. (4.8). This equation can describe both high frequency Langmuir waves and low frequency ion acoustic waves that are treated with fluid theory in Sec. 1.2.1 Solving this equation for \mathbf{k} and ω , we can obtain a relationship like Fig. 4.3. As shown in Sec. 4.2, C_i and C_e can be written in terms of $Z_-(\xi)$ (4.17) or $Z_{\kappa,-}^*(\xi_\kappa)$ (4.24). Z_- is given in terms of the complex error function. Appendix. C will be devoted to the derivation of $Z_{\kappa,-}^*$.

Appendix C

Derivation of $Z_{\kappa,-}^*(\xi_\kappa)$

In this appendix, we demonstrate the derivation of the function $Z_{\kappa,-}^*(\xi_\kappa)$ (Eq. (4.26)) which appears in the theory of Chap. 4 following Summers and Thorne (1991).

C.1 Gamma Function

In this derivation we use some properties of a Gamma function,

$$\Gamma(0) = 1 \tag{C.1}$$

$$\Gamma\left(\frac{1}{2}\right) = \sqrt{\pi} \tag{C.2}$$

$$\Gamma(x+1) = x\Gamma(x) \tag{C.3}$$

$$\Gamma(2x) = \frac{2^{2x-1}}{\sqrt{\pi}}\Gamma(x)\Gamma(x+1/2) \tag{C.4}$$

For an integer κ , Eqs. (C.1) and (C.3) lead to

$$\Gamma(\kappa+1) = \kappa! \tag{C.5}$$

C.2 Cauchy Residue Theorem

In evaluating $Z_{\kappa,-}^*(\xi_\kappa)$, integration with a complex variable is used. Cauchy residue theorem is extremely useful in integration of complex functions. This is given by

$$\oint f(z)dz = 2\pi i \sum_i Res(z_i) \quad (C.6)$$

where $Res(z_i)$ is a residue at the i -th pole of $f(z)$, and the residue at $z_i^{(n)}$ which is the n -th order pole of f

$$Res(z_i^{(n)}) = \frac{1}{(n-1)!} \frac{d^{n-1}}{dz^{n-1}} \left[f(z) \left(z - z_i^{(n)} \right)^n \right]_{z=z_i^{(n)}} \quad (C.7)$$

C.3 Derivation

$Z_{\kappa,-}^*(\xi_\kappa)$ is defined by Eq. (4.24) as an integral form of

$$Z_{\kappa,-}^*(\xi_\kappa) = \frac{\kappa^{\kappa-1/2} \Gamma(\kappa+1)}{\sqrt{\pi} \Gamma(\kappa-1/2)} \int_{-\infty}^{+\infty} \frac{ds}{(s-\xi_\kappa)(s^2+\kappa)^{\kappa+1}}$$

We take the integration along the contour on the complex plane as shown in Fig. C.1. The integration along the contour C_2 vanishes when $R \rightarrow \infty$. The task is to evaluate an integral

$$F(\xi_\kappa) = \int_{-\infty}^{+\infty} \frac{ds}{(s-\xi_\kappa)(s^2+\kappa)^{\kappa+1}} \quad (C.8)$$

Even though our Laplace transform is defined as $\text{Im}[\xi_\kappa] < 0$, $Z_{\kappa,-}^*$ can be defined also on the upper half plane and on the real axis by analytic continuation. Therefore, we take the integration contour $C_1 + C_2$ so that poles ξ_κ and $-i\sqrt{\kappa}$ are always enclosed inside by deforming C_1 if necessary. For all signs of $\text{Im}[\xi_\kappa]$, from Cauchy residue theorem, we find (Eq. (C.6))

$$F(\xi_\kappa) = -2\pi i [Res(\xi_\kappa) + Res(-i\sqrt{\kappa})] \quad (C.9)$$

The minus sign on the right-hand-side of Eq. (C.9) is because the integration is in a clockwise direction (Fig. C.1). Using Eq. (C.7), the residues are given by

$$Res(-i\sqrt{\kappa}) = (\xi_\kappa^2 + \kappa)^{-(\kappa+1)} \quad (C.10)$$

and

$$\begin{aligned}
Res(\xi_\kappa) &= \frac{1}{\kappa!} \frac{d^\kappa}{ds^\kappa} \left(\frac{1}{(s - \xi_\kappa)(s - i\sqrt{\kappa})^{\kappa+1}} \right) \Big|_{s=-i\sqrt{\kappa}} \\
&= \frac{1}{\kappa!} \sum_{l=0}^{\kappa} \left[\frac{\kappa!}{(\kappa - l)!l!} \frac{d^l}{ds^l} \frac{1}{(s - i\sqrt{\kappa})^{\kappa+1}} \frac{d^{\kappa-l}}{ds^{\kappa-l}} \frac{1}{s - \xi_\kappa} \right]_{s=-i\sqrt{\kappa}} \\
&= \sum_{l=0}^{\kappa} \frac{(\kappa + l)!}{l!\kappa!} \frac{1}{(2i\sqrt{\kappa})^{\kappa+l+1}} (-1)^\kappa \frac{1}{(\xi_\kappa + \sqrt{i\kappa})^{\kappa+1-l}}
\end{aligned} \tag{C.11}$$

Eqs. (C.10) and (C.11) are valid for all values of ξ_κ (except possibly for $\xi_\kappa = \pm i\sqrt{\kappa}$ which will be considered later). Then $Z_{\kappa,-}^*(\xi_\kappa)$ becomes

$$\begin{aligned}
Z_{\kappa,-}^*(\xi_\kappa) &= \frac{\kappa^{\kappa-1/2}\Gamma(\kappa+1)}{\sqrt{\pi}\Gamma(\kappa-1/2)} F(\xi_\kappa) \\
&= -\frac{2\sqrt{\pi}i\kappa!}{\Gamma(\kappa-1/2)\kappa^{3/2}} \left(1 + \frac{\xi_\kappa^2}{\kappa} \right)^{-(\kappa+1)} \\
&\quad \times \left[1 - \frac{1}{\kappa!} \frac{1}{2^{\kappa+1}} \left(1 + \frac{i\xi_\kappa}{\sqrt{\kappa}} \right)^{\kappa+1} \sum_{l=0}^{\kappa} \left(1 - \frac{i\xi_\kappa}{\sqrt{\kappa}} \right)^l \frac{(\kappa+l)!}{l!2^l} \right]
\end{aligned} \tag{C.12}$$

For $\xi_\kappa = -i\sqrt{\kappa}$ which is actually a removable pole

$$\begin{aligned}
Z_{\kappa,-}^*(-i\sqrt{\kappa}) &= \frac{\kappa^{\kappa-1/2}\Gamma(\kappa+1)}{\sqrt{\pi}\Gamma(\kappa-1/2)} (-2\pi i) \frac{1}{(\kappa+1)!} \frac{d^{\kappa+1}}{ds^{\kappa+1}} \left(\frac{1}{(s - i\sqrt{\kappa})^{\kappa+1}} \right) \\
&= -i \frac{(\kappa-1/2)(\kappa+1/2)}{(\kappa+1)\kappa^{2/3}}
\end{aligned} \tag{C.13}$$

Similarly for $\xi_\kappa = +i\sqrt{\kappa}$

$$\begin{aligned}
Z_{\kappa,-}^*(+i\sqrt{\kappa}) &= \frac{\kappa^{\kappa-1/2}\Gamma(\kappa+1)}{\sqrt{\pi}\Gamma(\kappa-1/2)} (-2\pi i) \left[\frac{1}{(\kappa+1)!} \frac{d^{\kappa+1}}{ds^{\kappa+1}} \left(\frac{1}{(s + i\sqrt{\kappa})^{\kappa+1}} \right) \right. \\
&\quad \left. + \frac{1}{\kappa!} \frac{d^\kappa}{ds^\kappa} \left(\frac{1}{(s - i\sqrt{\kappa})^\kappa} \right) \right] \\
&= 0
\end{aligned} \tag{C.14}$$

Now we set the terms in [] of Eq. (C.12) as $f_-(\xi_\kappa)$

$$f_-(\xi_\kappa) = 1 - \frac{1}{\kappa!} \frac{1}{2^{\kappa+1}} \left(1 + \frac{i\xi_\kappa}{\sqrt{\kappa}} \right)^{\kappa+1} \sum_{l=0}^{\kappa} \left(1 - \frac{i\xi_\kappa}{\sqrt{\kappa}} \right)^l \frac{(\kappa+l)!}{l!2^l} \tag{C.15}$$

and define another function g_- by

$$f_-(\xi_\kappa) \equiv 1 - g_-(\xi_\kappa) \tag{C.16}$$

Furthermore, if we define f_+ and g_+ as

$$f_+(\xi_\kappa) \equiv f_-(-\xi_\kappa) = 1 - g_-(-\xi_\kappa) \equiv 1 - g_+(\xi_\kappa) \quad (\text{C.17})$$

it can be shown that

$$f_- + f_+ = 1 \quad (\text{C.18})$$

This leads to

$$f_-(\xi_\kappa) = 1 - f_+ = 1 - (1 - g_+) = g_+ \quad (\text{C.19})$$

From Eqs. (C.12) and (C.19), we recover Eq. (4.26)

$$\begin{aligned} Z_{\kappa,-}^*(\xi_\kappa) &= -\frac{2\sqrt{\pi}i\kappa!}{\Gamma(\kappa - 1/2)\kappa^{3/2}} \left(1 + \frac{\xi_\kappa^2}{\kappa}\right)^{-(\kappa+1)} \\ &\times \left[\frac{1}{\kappa!} \frac{1}{2^{\kappa+1}} \left(1 - \frac{i\xi_\kappa}{\sqrt{\kappa}}\right)^{\kappa+1} \sum_{l=0}^{\kappa} \left(1 + \frac{i\xi_\kappa}{\sqrt{\kappa}}\right)^l \frac{(\kappa+l)!}{l!2^l} \right] \quad (\text{C.20}) \\ &= -\frac{\kappa - 1/2}{2\kappa^{3/2}} \frac{\kappa!}{(2\kappa)!} \\ &\times \sum_{l=0}^{\kappa} \frac{(\kappa+l)!}{l!} (-i)^{\kappa-l} \left(\frac{2}{(\xi_\kappa/\sqrt{\kappa}) - i}\right)^{\kappa+1-l} \quad (\text{Eq. (4.26)}) \end{aligned}$$

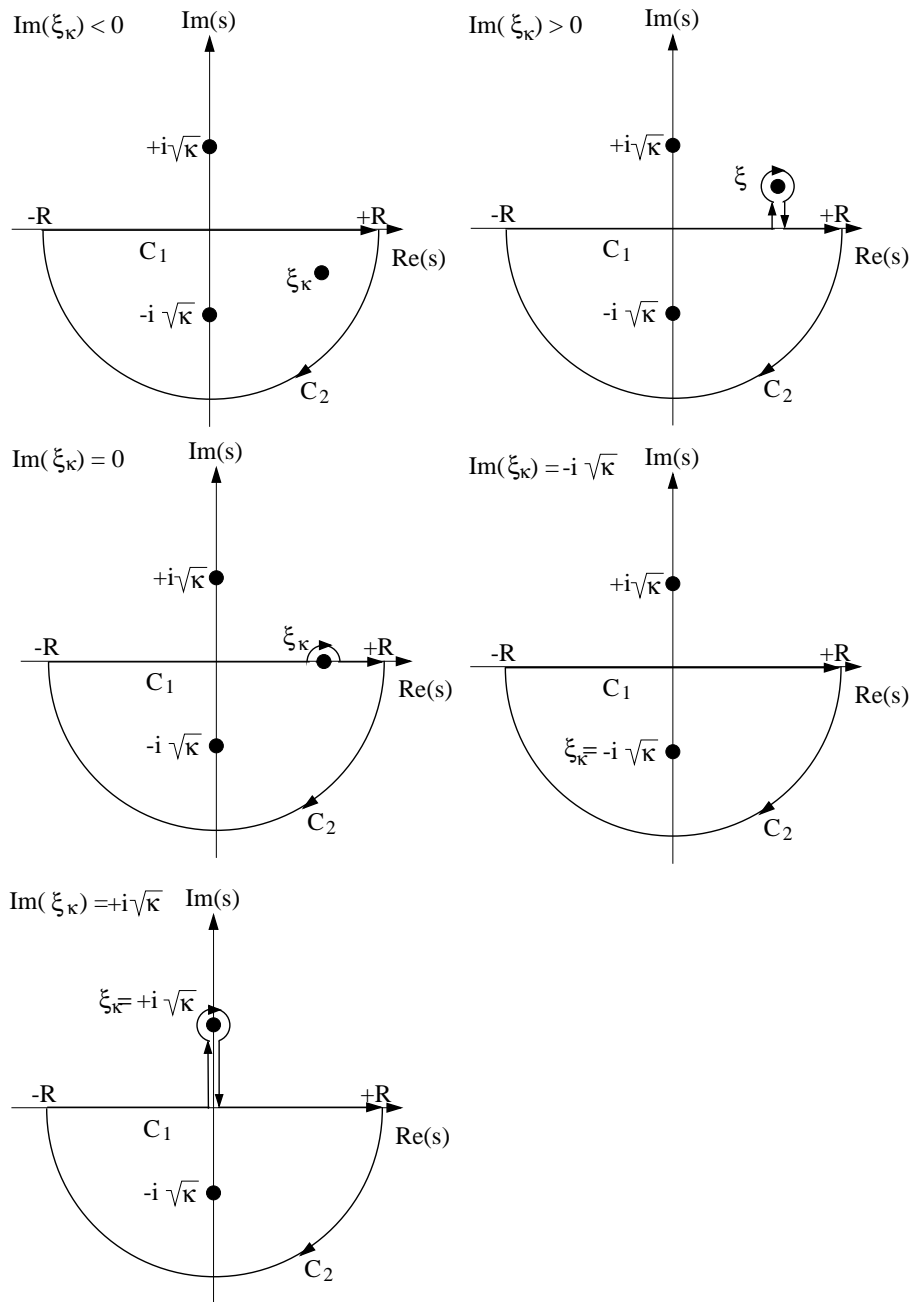


Figure C.1: Contours of integration for signs and special values of ξ_κ are shown. The contour C_1 must be above a pole ξ_κ , because the Laplace transform is defined as $\text{Im}[\xi_\kappa] < 0$.

Bibliography

- Baumjohann, W., and R. A. Treumann**, Basic space plasma physics, Imperial College Press, London, 1996.
- Bjørnå, N., and J. Trulsen**, Effect of a power law particle flux on the ionospheric incoherent scattering cross section, *Physica Scripta*, **33**, 284-288, 1986.
- Brekke, A.**, Physics of the upper polar atmosphere, Wiley, 1997.
- Bryant, D.**, Electron acceleration in the aurora and beyond, p. 75, Institute of Physics Publishing, Bristol and Philadelphia, 1999.
- Buchert, S. C. and S. Satio**, On the Pedersen current which is carried by electrons, *SUBSTORM-4*, 485-489, 1997.
- Buneman, O.**, Excitation of field aligned sound waves by electron streams, *Phys. Rev. Lett.*, **10**, 285-287, 1963.
- Christon, S. P., D. G. Mitchell, D. J. Williams, L. A. Frank, C. Y. Huang, and T. E. Eastman**, Energy spectra of plasma sheet ions and electrons from ~ 50 eV/e to ~ 1 MeV during plasma temperature transitions, *J. Geophys. Res.*, **93**, 2562-2572, 1988.
- Collis, P. N., I. Häggstöm, K. Kaila, and M. T. Rietveld**, EISCAT radar observations of enhanced incoherent scatter spectra; their relation to red aurora and field-aligned currents, *Geophys. Res. Lett.*, **18**, 1031-1034, 1991.

- Davies, J. A. and T. R. Robinson**, Heating of the high-latitude ionospheric plasma by electric fields, *Adv. Space Res.*, **20**, 1125-1128, 1997.
- Eglitis, P., P. W. McCrea, T. R. Robinson, T. B. Jones, K. Schlegel, and T. Nygren**, Flow dependence of COSCAT spectral characteristics, *J. Atmos. Terr. Phys.*, **58**, 189-203, 1996.
- Farley, D. T.**, A plasma instability resulting in field-aligned irregularities in the ionosphere, *J. Geophys. Res.*, **68**, 6083-6097, 1963.
- Farley, D. T.**, Theory of equatorial electrojet plasma waves: new developments and current status, *J. Atmos. Terr. Phys.*, **47**, 729-744, 1985.
- Fejer, B. G., D. T. Farley, B. B. Balsley, and R. F. Woodman**, Vertical backscattering region in the equatorial electrojet and the gradient drift instability, *J. Geophys. Res.*, **80**, 1313-1324, 1975
- Foster, J. C.**, Plasma turbulence and enhanced UHF backscatter from the topside ionosphere, *Phys. Space Plasmas*, **8**, 213-, 1988.
- Fried, B. D., and S. D. Conte**, The plasma dispersion function, Academic Press, 1961.
- Galeev, A. A.**, Spectra of plasma turbulence, particle acceleration and heating by plasma waves in the interacting plasma, in: Plasma waves and instabilities at comets and in magnetospheres, AGU, Washington DC, 1989.
- Hagfors, T.**, Electromagnetic wave propagation in a field-aligned-striated cold magnetoplasma with application to the ionosphere, *J. Atmos. Terr. Phys.*, **46**, 211-216, 1984.
- Haldoupis, C., K. Schlegel, and E. Nielsen**, Some observations of radio auroral backscatter at 140 MHz during E-region electron gas heating, *Ann. Geophysicae*, **11**, 283-295, 1993.
- Hasegawa, A., M. Kunioki, and M. Duong-van**, Plasma distribution function in a superthermal radiation field, *Phys. Rev. Lett.*, **54**, 2608-2610, 1985.

- Hedin, A. E.**, Extension of the MSIS thermosphere model into the middle and lower atmosphere, *J. Geophys. Res.*, **96**, 1159-1172, 1991.
- Hoh, F. C.**, Instability of Penning-type discharge, *Phys. Fluids*, **6**, 1184-1191, 1963.
- Hunsucker, R. D.**, Radio techniques for probing the terrestrial ionosphere, Springer-Verlag, 1991.
- Igarashi, K., and K. Schlegel**, Electron temperature enhancements in the polar *E* region measured with EISCAT, *J. Atmos. Terr. Phys.*, **49**, 273-280, 1987.
- Jones, B., P. J. S. Williams, K. Schlegel, T. Robinson and I. Häggström**, Interpretation of enhanced electron temperatures measured in the auroral *E* region during the ERRRIS campaign, *Ann. Geophys.*, **9**, 55-59, 1991.
- Karal, F. C., and J. B. Keller**, Elastic, electromagnetic, and other waves in a random medium, *J. Math. Phys.*, **5**, 537-547, 1964.
- Kelley, M. C.**, The Earth's Ionosphere, Academic Press, 1989.
- Liu, C. H.**, Effective dielectric tensor and propagation constant of plane waves in a random anisotropic medium, *J. Math. Phys.*, **8**, 2236-2242, 1967.
- Maeda, K., T. Tsuda, and H. Maeda**, Theoretical interpretation of the equatorial sporadic *E* layers, *Phys. Rev. Lett.*, **11**, 406-407, 1963.
- Moorcroft, D. R., and K. Schlegel**, *E* region coherent backscatter at short wavelength and large aspect angle, *J. Geophys. Res.*, **93**, 2005-2010, 1988.
- Nielsen, E., and K. Schlegel**, A first comparison of STARE and EISCAT electron drift velocity measurements, *J. Geophys. Res.*, **88**, 5745-5750, 1983.
- Nielsen, E., and K. Schlegel**, Coherent radar Doppler measurements and their relationship to the ionospheric electron drift velocity, *J. Geophys. Res.*, **90**, 3498-3504, 1985.

- Ogawa, T., B. B. Balsley, W. L. Ecklund, D. A. Carter, and P. E. Johnston, Aspect angle dependence of irregularity phase velocities in the auroral electrojet, *Geophys. Res. Lett.*, **7**, 1081-1084, 1980
- Ogawa, Y., R. Fujii, S. C. Buchert, S. Nozawa, S. Watanabe, and A. P. Van Eyken, Simultaneous EISCAT Svalbard and VHF radar observations of ion upflows at different aspect angles, *Geophys. Res. Lett.*, **27**, 81-84, 2000.
- Oyama, K., K. Hirao, P. M. Banks, and P. R. Williamson, Is T_e equal to T_n at the heights of 100 to 120 km? *Planet. Space Sci.*, **28**, 207-211, 1980.
- Pfaff, R. F., M. C. Kelley, B. G. Fejer, E. Kudeki, C. W. Carlson, A. Pedersen, and B. Häusler, Electric field and plasma density measurements in the auroral electrojet, *J. Geophys. Res.*, **89**, 236-244, 1984.
- Primdahl, F., and A. Bahnsen, Auroral E region diagnosis by means of nonlinearly stabilized plasma waves, *Ann. Geophys.*, **3**, 57-62, 1985.
- Raman, R. S. V., J. P. St.-Maurice, and R. S. B. Ong, Incoherent scattering of radar waves in the auroral ionosphere, *J. Geophys. Res.*, **86**, 4751-4762, 1981.
- Rees, M. H., Physics and chemistry of the upper atmosphere, Cambridge University Press, 1989.
- Rietveld, M. T., P. N. Collis, and J.-P. St.-Maurice, Naturally enhanced ion acoustic waves in the auroral ionosphere observed with EISCAT 933 MHz radar, *J. Geophys. Res.*, **96**, 19291-19305, 1991.
- Robinson, T. R., Toward a self-consistent non-linear theory of radar auroral backscatter, *J. Atmos. Terr. Phys.*, **48**, 417-422, 1986.
- Robinson, T. R., Simulation of convection flow estimation errors in VHF bistatic auroral radar systems *Ann. Geophysicae*, **11**, 1033-1050, 1993.

- Robinson, T. R., and F. Honary**, A resonance broadening kinetic theory of the modified two-stream instability: Implications for radar auroral backscatter experiments, *J. Geophys. Res.*, **95**, 1073-1085, 1990
- Sahr, J. D., and B. G. Fejer**, Auroral electrojet plasma irregularity theory and experiment: A critical review of present understanding and future directions, *J. Geophys. Res.*, **101**, 26893-26909, 1996.
- Saito, S., F. Forme, S. C. Buchert, S. Nozawa, and R. Fujii**, Effects of a kappa distribution function of electrons on incoherent scatter spectra, *Ann. Geophysicae*, **18**, 1216-1223, 2000.
- Saito, S., S. C. Buchert, S. Nozawa, and R. Fujii**, Observation of isotropic electron temperatures in the turbulent E region, *Ann. Geophysicae*, **19**, 11-15, 2001.
- Schlegel, K., and J. -P. St.-Maurice**, Anomalous heating of the polar *E* region by unstable plasma waves, 1. Observations, *J. Geophys. Res.*, **86**, 1447-1452, 1981.
- Schlegel, K., K.-I. Oyama, and K. Hirao**, Quantitative explanation of some electron temperature profiles measured *in situ* in the high latitude ionospheric *E*-region, *J. Geomag. Geoelectr.*, **35**, 357-366, 1983.
- Schunk, R. W., and A. F. Nagy**, Electron temperature in the *F* region of the ionosphere: Theory and observations, *Rev. Geophys. and Space phys.*, **16**, 355-399, 1978.
- Sheffield, J.**, Plasma scattering of electromagnetic radiation, Academic Press, 1975.
- Simon, A.**, Instability of a partially ionized plasma in crossed electric and magnetic fields, *Phys. Fluids*, **6**, 382-388, 1963.
- Stauning, P.**, Absorption of cosmic noise in the E region during electron heating events. A new class of riometer absorption events, *Geophys. Res. Lett.*, **11**, 1184-1187, 1984.
- Stauning, P. and J. K. Olesen**, Observations of the unstable plasma in the disturbed polar E region, *Physica Scripta*, **40**, 325-332, 1989.

- St.-Maurice, J. P.**, A unified theory of anomalous resistivity and Joule heating effects in the presence of E-region irregularities, *J. Geophys. Res.*, **92**, 323-327, 1987.
- St.-Maurice, J. P and W. B. Hanson**, Ion frictional heating at high-latitudes and its possible use for an in situ determination of neutral thermospheric winds and temperatures, *J. Geophys. Res.*, **87**, 7580-7602, 1982.
- St.-Maurice J.-P., and R. Laher**, Are observed broadband wave amplitudes large enough to explain the enhanced electron temperatures of the high-latitude E region?, *J. Geophys. Res.*, **90**, 2843-2850, 1985
- St.-Maurice, J. P and K. Schlegel**, Estimates of plasma wave amplitudes in the turbulent high-latitude *E* region using electron temperature measurements, *J. Geophys. Res.*, **87**, 5197-5201, 1982.
- St.-Maurice, J. -P., and R. W. Schunk**, Ion velocity distributions in the high latitude ionosphere, *Rev. Geophys. Space Phys.*, **17**, 99-134, 1979.
- St.-Maurice, J. -P., K. Schlegel, and P. M. Banks**, Anomalous heating of the polar *E* region by unstable plasma waves, 2. Theory, *J. Geophys. Res.*, **86**, 1453-1462, 1981.
- Sudan, R. N.**, Unified theory of type I and type II irregularities in the equatorial electrojet, *J. Geophys. Res.*, **88**, 4835-4860, 1983
- Summers, D., and R. M. Thorne**, The modified plasma dispersion function, *Phys. Fluids*, **B3**, 1835-1847, 1991.
- Summers, D., R. M. Thorne, and H. Matsumoto**, Evaluation of the modified plasma dispersion function for half-integral indices, *Phys. plasmas*, **3**, 2496-2501, 1996.
- Svenes, K. R., B. N. Maehlum, J. Troim, G. Holmgren, R. L. Arnoldy, U. P. Løvhaug, M. T. Lietveld, and C. Hall**, Combined rocket and ground observations of electron heating in the ionospheric F-layer, *Planet. and Space Sci.*, **40**, 901-905, 1992.

- Thorne, R. M., and D. Summers**, Landau damping in space plasmas, *Phys. Fluids*, **B3**, 2117-2123, 1991.
- Trondsen, T. S., and L. L. Cogger**, High-resolution television observations of black aurora, *J. Geophys. Res.*, **102**, 363-378, 1997.
- Vasyliunas, V. M.**, A survey of low-energy electrons in the evening sector of the magnetosphere with OGO 1 and OGO 3, *J. Geophys. Res.*, **73**, 2839-2885, 1968.
- Wahlund, J.-E., F. R. E. Forme, H. J. Opgenoorth, M. A. L. Persson, E. V. Mishin, and A. S. Volokitin**, Scattering of electromagnetic waves from a plasma: Enhanced ion acoustic fluctuations due to ion-ion two-stream instabilities, *Geophys. Res. Lett.*, **19**, 1919-1922, 1992.
- Williams, P. J. S., G. O. L. Jones, B. Jones and H. Opgenoorth**, High-resolution measurements of magnetospheric electric fields, *J. Atmos. Terr. Phys.*, **52**, 439-448, 1990.
- Zheng, J., C. X. Yu, and Z. J. Zheng**, Effects of non-Maxwellian (super-Gaussian) electron distribution on the spectrum of Thomson scattering, *Phys. Plasmas*, **4**, 2736-2740, 1997.